The geology of the western Nuba Mountains region, South Kordofan State, Sudan, with special emphasis on the low-grade Neoproterozoic meta-volcano-sedimentary sequence.

By

Montasir Ahmed Ibinoof Mohammed

Submitted in partial fulfillment of the requirements for the degree

DOCTOR OF PHILOSOPHY

In the Faculty of Agriculture and Natural Sciences

University of Pretoria

PRETORIA

April 2017

THIS THESIS REPRESENTS THE ORIGINAL WORK

OF THE AUTHOR, EXCEPT WHERE SPECIFIC

ACKNOWLEDGMENT IS MADE

TO THE WORK OF OTHERS

April 2017

ABSTRACT.

Dismembered and low-grade metamorphosed occurrences of mafic extrusive and intrusive and minor ultramafic rocks, grouped as the Arid unit, similar to those of the Arabian Nubian Shield (ANS), are reported here for the first time in the westernmost part of the Nuba Mountains, southeastern Sudan. These occurrences are interpreted to represent part of an ophiolite sequence with a lower cumulate layer composed of layered gabbro and minor cumulate hornblendite and a top layer of thick massive gabbro, pillowed basalt and basaltic andesite. The Arid unit is structurally underlain by basaltic-andesite and andesite and a metasedimentary sequence identified as turbidite and both grouped as the Abutulu unit. All of the rocks are slightly sheared, deformed and metamorphosed under low-grade greenschist facies. New geochemical and Sr-Nd isotope data reveal that the low-grade metavolcanic rocks of the westernmost Nuba Mountains represent a Neoproterozoic oceanic arc/back-arc assemblage. The massive gabbro and pillowed basalt of the Arid unit show the geochemical characteristics of HFSE-depleted tholeiitic basalt while the co-genetic and more evolved meta-andesite of Abutulu unit show a calc-alkaline signature. Both units display a REE pattern characterized by LILE enrichment indicating formation in an arc/back-arc environment. This arc was active at around 778±90 Ma (Sm-Nd 12 WR isochron) that is similar in age to arc magmatism in the ANS. The close interval between the T_{DM} Nd model age (average of 10 metavolcanic samples is 814 Ma) and the crystallization age (778±90 Ma) is indicative of little or no involvement of older crustal material. The western Nuba Mountains metavolcanic rocks have ε_{Nd} values of +5.9 at 778 Ma (average of 12

samples) indicating a depleted mantle source similar to that of the ANS (published range from +6.5 to +8.4).

The metavolcanic rocks are structurally bounded from the eastern side by medium-grade orthogneisses and supracrustal metasediments intruded by syn to late-orogenic granite. Based on their geochemistry and isotopic characteristics these gneisses are interpreted to be evolved from an arc magma source of early Neoproterozoic age 976±58 Ma corresponds to ε_{Nd} value of +6.3±0.9 (six point Nd isochron). The tight clustering of ε_{Nd} values and the T_{DM} Nd model ages preclude significant involvement of older crustal material and hence these gneisses are assigned to intra-oceanic arc environments.

New ion microprobe (SHRIMP) U–Pb dating of zircon from late-orogenic granite reveal early Ediacaran ages of emplacement for the main magmatic phases. This event started at 624±7 Ma (earliest concordance $^{206}Pb/^{238}U$ age of magmatic zircon core 2.2) and possibly lasted up to 605±10 Ma (youngest concordance $^{206}Pb/^{238}U$ age of magmatic zircon rim). The magmatic event was contemporaneous with high temperature metamorphism reflected by metamorphic rims (discordant $^{206}Pb/^{238}U$ age 614±8 Ma to 583±6 Ma) which are undistinguishable from magmatic rims ($^{206}Pb/^{238}U$ age 613±6 Ma to 605±10 Ma). The early magmatic phase is thought to be around 743±8 Ma (the earliest discordance $^{206}Pb/^{238}U$ age of magmatic zircon core 5.2). The subduction-related geochemical signature of the granite allow for the use of the 743±8 Ma as a lower control on the west dipping subduction event. Significantly no ages older than Neoproterozoic were recorded in any of the 19 zircon crystals analyzed.

It is proposed that the metavolcanic and associated plutonic mafic rocks represent a unique Neoproterozoic entity named the Abutulu terrane that developed in a marginal back-arc basin west of the intra-oceanic arc. The Abutulu terrane is a western continuation of the ANS, through the medium-grade gneisses of the intra-oceanic arc, then the eastern boundary of the SMC must occur further west of its current location and possibly assigned to the Abutulu suture zone.

TABLE OF CONTENTS

LIST OF FIGURES:

LIST OF PLATES:

LIST OF TABLES:

1-Introduction:

1.1: location of the study area:

The area covered during this research is situated in the southern part of the Republic of Sudan, specificaly in the western Nuba Mountains in the southeastern and central parts of West Kordofan State (Fig. 1-1). The study area is bounded by latitudes 11.21° N and 12.0° and longitudes 28.48° E and 29.77° E covering an area of 14,900 km^2 (Fig. 1-1).

The Nuba Mountains are covered by a network of asphalt roads between Khartoum and El Obied, from El Obied to El Fula and El Dalang, and from El Dalang to Kadugli. District administrative centers are linked by motor tracks varying in quality, most of which are closed in the rainy season (Fig. 1-1 and Fig. 1-2).

The railway line, which extends from Khartoum to El Obied passes through the NW parts of the region. Regular flights run between Khartoum-El Obied, Khartoum-Kadugli and El Obied- Kadugli.

The study area is accessible from Khartoum either by asphalt road from Khartoum to Kadugli, using the exits towards Lagawa, and then via minor roads to the different parts of the area, or by asphalt road from Khartoum to El Fula. The study area is quite inaccessible in the rainy season with the exception of few roads that are passable with great difficulty.

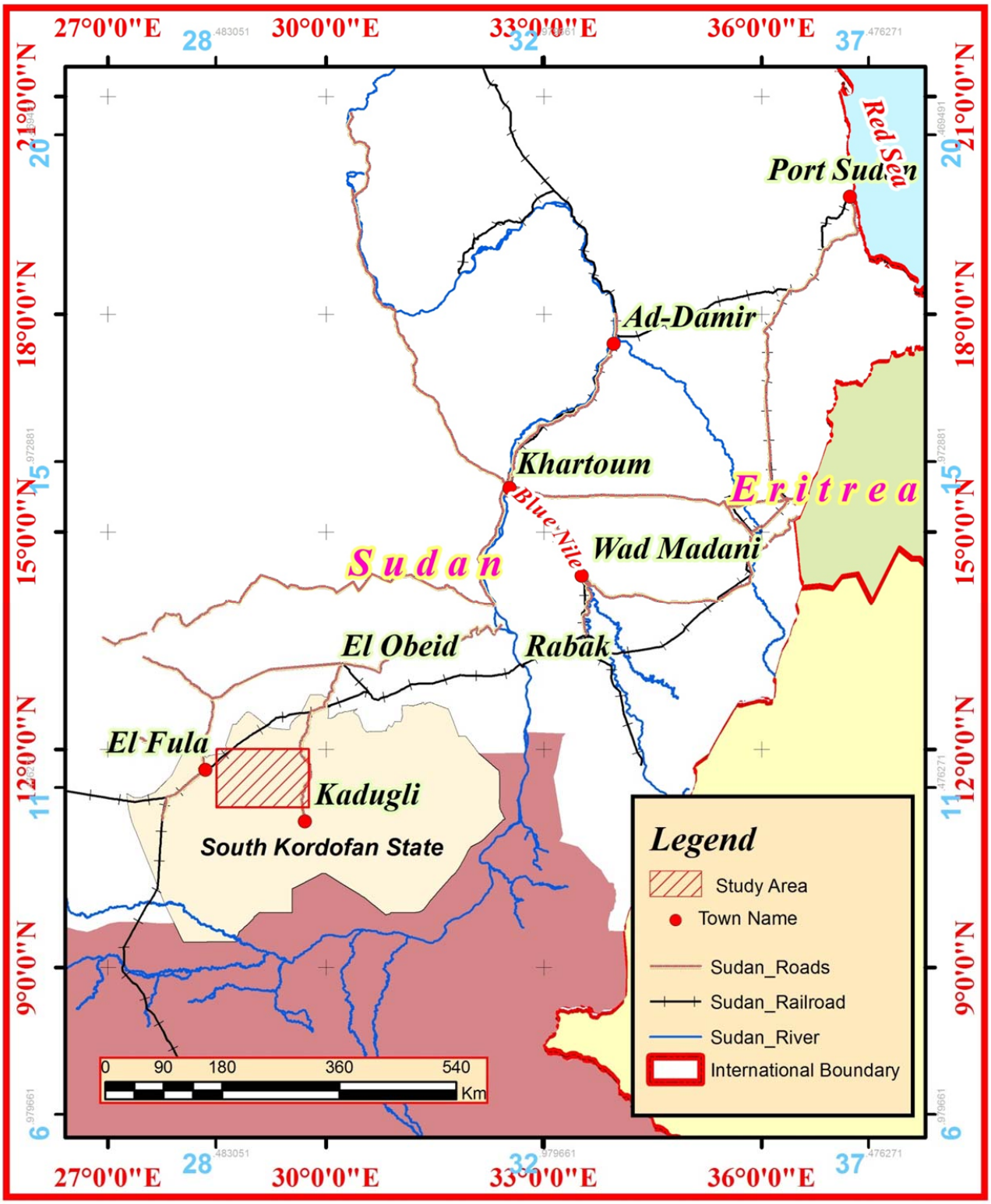

Figure 1-1: A map showing the location of the study area within Sudan and northeastern Africa.

1-2 Physiography and Drainage System:

The study area lies on the southeastern edge of a gentle topographic swell in the south central plain of the Sudan and rises to a height of 700m above sea level in the centre. The elevation decreases to 450m above sea level at the periphery of the study area. Outstanding massifs, group of hills and inselbergs are generally very steep and reach a maximum height of 998m (above sea level) at Jebel Tuleshi (Fig. 1-2). Other major hills are Tabaq (930m), Damiek (904m), Lagawa (845m), and Keiga El Khail (709m) (Fig. 1-2).

A network of intermittent seasonal streams (Wadies) traverses the Nuba Mountains. Most of the wadies are structurally controlled along fractures and joints giving rise to a rectangular and subdendritic drainage pattern (Fig. 1-2). The watercourses are dry for most of the year but carry considerable run-off during the rainy season when up to 700mm is precipitated. In spite of this, some natural depressions hold considerable amounts of water for the whole year and being used as permanent sources of drinking water (e.g. Lake Miri).

1-3 Climate and the Vegetation Cover:

The Nuba Mountains are characterized by a Savannah climate ranging from poor Savannah in the northern part with a long dry season, to rich Savannah in the southern part of the region with a long rainy season (June - October) and considerable rainfall (up to 700mm).

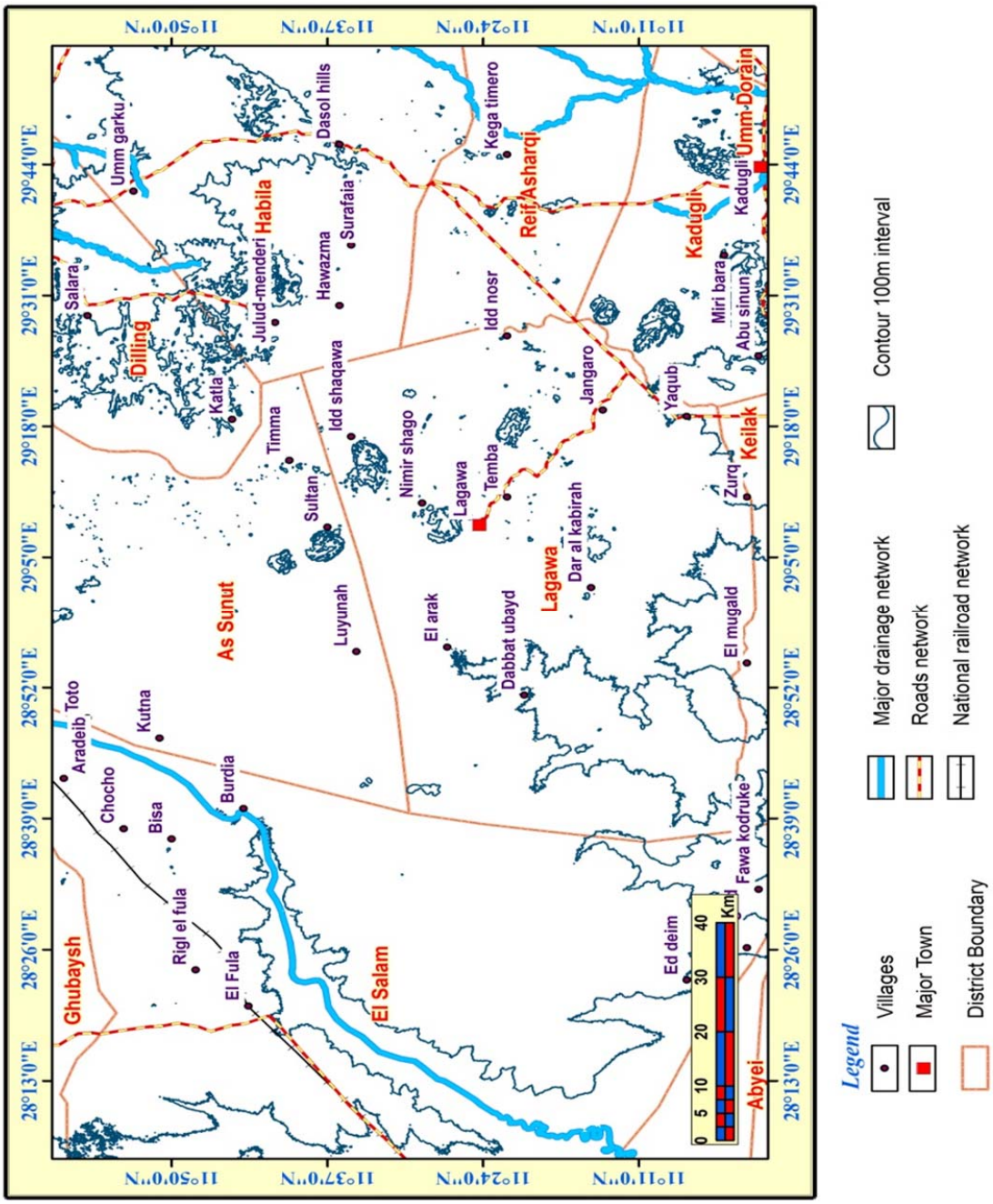

Figure 1-2: Topographic map of the study area.

The summer is generally hot with an average temperature of *ca* 30ºC. The vegetation includes moderate to tall grass cover interspersed by variable thorny acacia trees that mainly cluster on the topographic surfaces of the outcrops, and concentrate along the drainage channels and around the natural pools. The vegetation cover gets denser and taller southwards where forests of rich Savannah climate are encountered.

1-4 Socio-Economic Features:

The region is mainly inhabited by the Nuba tribes in the central and Eastern parts of the study area and the Misseriya tribes in the western part. The Nubas are mainly engaged with seasonal rain-fed cultivation and rearing of the domestic animals such as cattle, sheep and goats. The Misseriya are mainly nomadic, breeding cattle, with a few pursuing seasonal agricultural activities in the wadies.

1-5 Previous work on the geology of the Nuba Mountains:

1-5-1: Summary of the work of Vail (1973):

Vail (1973) was motivated by the lack of either systematic geological research or published geological maps of the Nuba Mountains Region (NMR) despite the enormous size of the region (approximately 143000 km^2) and more than 100 years of geological research in the region.

1-5-1-1: Lithostratigraphic succession suggested by Vail (1973):

Vail (1973) divided the geology of the Nuba Mountains Region (NMR) into two major units (Table 1): The Basement Complex and Post-Basement Complex Formations. He further subdivided the Basement Complex into four subunits; 1- Metamorphosed schist

and gneiss; 2- Slightly foliated gabbro; 3- Non-foliated granitic and syenitic intrusive masses and 4- Dykes.

Vail (1973) found that the metamorphosed schists and gneisses were made up of (a) dominant banded granitic and granodioritic gneisses, (b) a metasedimentary rock succession represented by crystalline limestone and graphitic schist and (c) rare metavolcanic rocks represented by hornblende gneiss and localized meta-andesite.

Within the Post-Basement Complex Formations Vail (1973) identified four subunits: (a) purple schistose mudstone and minor limestone known as the Nawa Formation that is only found in boreholes (ie no outcrop), (b) the Cretaceous-aged Nubian Sandstone Formation which represents continental deposits of cross-bedded pebbly grits, sandstones and mudstones located along basins or troughs that crop out at the western and northern margins of the NMR, (c) unconsolidated sands, gravels, silts and clays of the Umm Ruwaba Formation that cover most of the older lithologies in the NMR and suggested by Vail (1973) to have a Quaternary age, and (d) recent aeolian sediments known locally as Qoz Sands.

1-5-1-2: Field relations and structural setting observed by Vail (1973):

The scattered and isolated nature of the outcrops and the thick soil cover that obscures most of the surface geology prevented Vail (1973) from seeing any useful field relationships within the units of the Basement Complex. He mentioned that no geological contacts against any of the units were observed. However, he noticed that schist and gneiss share evidence for a dominant tectonic event, the metasedimentary

rocks are conformable with the surrounding gneiss and schist, and most of them are affected by later brittle deformation.

Vail (1973) identified two types of structures, (a) ductile, tectonic-related structures that affect the oldest rocks and (b) brittle, post-orogenic fractures observed in most of the lithologies. Structures in the metamorphosed schists and gneisses are mainly folds with general N to NNE plunging fold axes, with steeply-dipping limbs. The brittle structures are characterized by two fracture patterns, (a) an E-W dominant set that cuts the entire northern part of the study area and (b) a NE-SW set that is observed in the NMR as well as in the neighbouring Darfur region.

1-5-1-3 Conclusion and sequence of events Vail (1973):

Vail (1973) proposed that the earliest event in the NMR is the “deposition of psammitic, pelitic and volcanic rocks on an unknown basement”. These lithologies are now represented by migmatized and granitized gneisses and schists in which the original primary features no longer exist. Gabbroic bodies were then emplaced into the gneiss and schist.

A sequence of low-grade graphitic schist, siltstone and limestone overlay the gneiss unit. The last event in the basement is the intrusion of granitic and granodioritic igneous rocks and associated dyke swarms.

The next episode is the deposition of the Nawa Formation (red shales, silts and minor limestones), which are now slightly metamorphosed.

The third phase of deposition took place after a long period, during which erosion of the earliest units led to uneven topography, on which the continental sedimentary strata of the Cretaceous-aged Nubian sandstone accumulated. Rapid deposition of the unconsolidated and variable sediments of the Umm Ruwaba Formation took place in the Quaternary, following a second episode of erosion. The events in the region were concluded by the deposition of widely spread clay soils and wind blown sands in recent times.

Due to the lack of any geochronological data Vail (1973) correlated the units of the NMR with those of the neighbouring regions and suggested the following ages:

- Precambrian age for all of the tectonic events in the basement complex with a Pan African age (600- 500 Ma) for the youngest event.
- Cambro-Ordovician age for the post-orogenic granites and syenites similar to the Younger Granite-type igneous province of north Sudan (Vail, 1990).
- Early Paleozoic age for Nawa Formation.
- Late Cretaceous age for the Nubian Sandstone as identified from fossil evidence in Darfur.

1-5-2: Summary of the work of Sadig and Vail (1986):

Sadig and Vail (1986) summarized the geological work done after that of Vail (1973), mainly those of El Ageed and El Rabaa (1981) and Brinkman (1982). They introduced a new lithological succession for the NMR as well as further elaboration on the field relationships between the various units. They also conducted and interpreted the results

of two gravity profiles across the western part of the NMR and showed the usefulness of gravity methods in identifying various basement components in central Sudan.

1-5-2-1: Lithological succession of Sadig and Vail (1986):

In their new succession Sadig and Vail (1986) divided the metamorphosed schists and gneiss unit of Vail (1973) into two units, (i) Quartzo-feldspathic gneiss, that is basically made up metamorphosed sedimentary rocks, and sheared and altered granitoids with reported occurrences of hornblende augen gneiss, granodioritic gneiss and muscovite, biotite and sillimanite gneisses, and (ii) a metasedimentary rock unit that comprises paragneisses, mica and graphitic schists. They also introduced a new volcano-sedimentary unit which is made up of meta-volcanic rocks (mainly meta-andesite) intercalated with pyroclastic and sedimentary layers. This unit is restricted to two localities, one in the west and one in the east of the NMR. The eastern outcrop contains important lenses of chromitiferous serpentinite. Sadig and Vail, (1986) correlated this with similar occurrences in the Kurmuk – Ingessana region and also in the Red Sea region, and hence they interpreted these eastern occurrences as a disturbed ophiolite. This interpretation motivated the authors to reconsider the regional geology of the region and consider the area from a new perspective. Of importance was the reclassification of the gabbroic unit of Vail (1973) into the new volcano-sedimentary unit. However Sadig and Vail, (1986) never gave any description whether these occurrences were of ophiolitic origin or not.

According to Sadig and Vail (1986) All of the previously mentioned units have been intruded by syn to late-orogenic batholitic granitoids of granitic and granodioritic composition. They are foliated and underlie areas of highest topography.

Other forms of intrusion reported by Sadig and Vail (1986) are anorogenic alkali intrusions of mainly granitic and syenitic composition and their volcanic equivalent, and minor foid syenites.

1-5-2-2: Field relations observed by Sadig and Vail (1986):

Sadig and Vail (1986) highlighted an important relationship regarding the basement complex, which has also been recorded by several others since the work of Vail (1973) (e.g. the work of El Ageed and El Rabaa [1981] which will be discussed separately in section 1-5-3).

This relationship observed by Sadig and Vail (1986) concerns the intercalation of gneisses comprising weakly metamorphosed sedimentary rocks with sheared and altered granitoids. This observation led Vail to suggest that at least part of the gneisses may represent a higher grade equavilent of low grade units.

The metasedimentary rocks unit shows no clear relationship with the gneiss. In places they may grade into one another, and in other places show a sharp contact identified earlier in the eastern NMR by El Ageed and El Rabaa (1981) as a westerly dipping thrust contact. Sadig and Vail (1986) also suggested strongly deformed and tectonized contacts between the metasedimentary rocks and gneiss, as indicated by mylonitization and shearing. Sadig and Vail (1986) drew attention to the possibility that the meta-

sedimentary rocks might be intercalated with meta-volcanic rocks to form one metavolcano-sedimentary unit as proposed by Vail (1983) elsewhere in Sudan.

1-5-3: Summary of the work of El Ageed and El Rabaa (1981):

An important contribution to the geological research in the Nuba Mountains with special focus on the northeastern Nuba Mountains was provided by El Ageed and El Rabaa (1981). They mapped the area in detail at a scale of 1:48000 to 1:40000 and also provided significant remarks and observations regarding the basement complex in which they introduced a new classification of the metasedimentary rocks and the metavolcanic rocks units of the basement complex.

1.5.3.1 Lithological succession of El Ageed and El Rabaa (1981):

El Ageed and El Rabaa (1981) recognized four major units in the northeastern Nuba Mountains; (a) gneiss, (b) metasedimentary rocks, (c) metavolcanic rocks and (d) younger intrusives. The gneiss described by El Ageed and El Rabaa (1981) were only the hornblende gneiss that outcrop in the core of a dome structure. Overlying the gneiss is a metasedimentary rock unit comprising eight individual inter-banded rock subunits that were arranged by El Ageed and El Rabaa (1981) stratigraphically from oldest in the bottom and youngest in the top as follows:

9- Graphitic-quartzofeldspathic schists.

8- Quartzofeldspathic schists.

7- Tremolite marbles.

6- Amphibolite schists.

5- Calc-semipelites.

4- Grey marble.

3- Quartzites.

2- Quartz-muscovite schists.

1- Graphitic schists.

On top of the metasedimentary rocks is a metavolcanic rock unit that consists of meta-basic volcanics at the bottom and meta-acidic volcanics at the top. Lenses of chromiferous serpentinite composition were identified within the basic-metavolcanic strata, associated with calc-carbonates, which has recently been interpreted as part of an ophiolite association (Abdelsalam and Dawoud, 1991 and references therein). Younger intrusive rocks have intruded the earlier mentioned lithologies and caused local thermal metamorphism.

1.5.3.2 Structural framework suggested by El Ageed and El Rabaa (1981):

El Ageed and El Rabaa (1981) identified at least three phases of deformation (D_1, D_2 and D_3) responsible for three episodes of metamorphism (M_1, M_2 and M_3). In their model D_1 is characterized by tight, inclined folds and is responsible for the development of a S_1 foliation. M_1 metamorphism reached amphibolite facies conditions in post-D_1 times. D_2 deformation is characterized by easterly-verging thrusts and closed to tight folds that have resulted in the formation of a S_2 foliation. M_2 metamorphism, associated with D_2 deformation, occured under greenschist facies conditions. The latest phase of deformation, characterized by the formation of major wrench faults, resulted in M_3 regional cataclasis. Variations in the expression of different deformational phases

among the different lithologies led El Ageed and El Rabaa (1981) to divide the area into three regions and examine each region separately.

1-5-4: The work of Brinkmann (1986):

1-5-4-1 Summary of the work of Brinkmann:

As part of Sudanese-German Technical cooperation, the Federal Institute for Geosciences and Natural resources, Hannover, Germany (BGR) carried out work for a mineral inventory program in the northeastern Nuba Mountains between the years 1980 and 1984. The outcomes of this project were published in several reports; including that of Brinkmann, (1986).

In his work, Brinkmann provided a review on the geology and geochronology of the northeastern Nuba Mountains and discussed the presence of a number of ophiolite-related and non-related mineralized areas. He also suggested a new stratigraphic succession for the Nuba Mountains.

1-5-4-2 Field relations and lithostratigraphic succession:

The main difference between the proposed succession of Brinkmann and all of those previously discussed, is the consideration of the medium-grade gneisses as part of the low-grade metavolcanics and metasediments. Hence, Brinkmann considered the volcano-sedimentary sequence as the older unit in the geology of the Nuba Mountains. His identification of the volcano-sedimentary sequence as the older unit is based on the observation by Brinkmann (1986) and Vail (1973) that the gneisses are intercalated in several locations by weakly metamorphosed sedimentary rocks. This phenomenon led

Vail (1983) to suggest that the gneiss domes “probably only represent local areas of greater heat flow and doming within the greenschist facies rock” (Brinkmann, 1986).

Brinkmann (1986) also mentioned that during their work in the Nuba Mountains, he observed no rocks of amphibolite facies, except those preserved in the retrograded ophiolite rocks. He considered the gneiss of the northeastern Nuba Mountains as a lateral, higher grade equivalent of the lower-grade metamorphic volcano-sedimentary series.

Brinkmann (1986) proposed a nine-fold sequence of events in the Nuba Mountains. The earliest two episodes were associated with an island arc environment, where the extrusion of mainly basic volcanic rocks preceded the deposition of various sediments that were intercalated with volcaniclastic rocks. The subsequent collision of the island arcs of the ANS led to the emplacement of ophiolitic slivers and the intrusion of syn-orogenic granite. Three cycles of magmatic intrusion took place at 700 Ma, 550 Ma and 250 Ma.The geological history proposed by Brinkmann (1986) is provided in table 1-1.

1-5-5: The work of Abdelsalam and Dawoud (1991):

Abdelsalam and Dawoud (1991) redefined the boundary between the Pan-African Arabian Nubian Shield and the pre-Pan-African continental crust as the Kabus ophiolitic mélange in the northeastern (NMR), west of the previously suggested location at the Ingessana hills. They based their description of the basement units in the area mainly on the works of Vail (1973), Shadad et al. (1979) and Sadig and Vail (1986). Abdelsalam and Dawoud (1991) regrouped the basement units identified by the previous authors into two main lithogeographical units; the high-grade gneisses that

occupy the western part of the northeastern NMR and the low-grade volcano-sedimentary sequence identified in the eastern part of the northeastern NMR. These two units are separated by the Kabus ophiolitic mélange. The western high-grade gneises are pre-Pan-African in age, possibly Archaean to early Proterozoic, and the eastern low-grade volcano-sedimentary sequence have a Pan-African age). In their consideration of the age of the gneissic unit, Abdelsalam and Dawoud (1991) discussed the geochronological data obtained by Harris et al. (1984) and Curtis and Lenz (1985) and came to the conclusion that although the majority of the data suggest a Pan-African age, the high initial $^{87}Sr/^{86}Sr$ ratio observed in one outcrop (Jebel Doleibaya) suggests the presence of pre-Pan-African crustal material within the rocks of the NMR. Abdelsalam and Dawoud (1991) have confirmed the three phases of deformation (D_1, D_2 and D_3) previously described by El Ageed and El Rabaa (1981).

Using geological, geochronological, structural and geophysical data Abdelsalam and Dawoud (1991) have produced a three stage tectonic model in which (1) a westerly dipping subduction zone led to the formation of an intra-oceanic island arc and opening of a marginal basin between the arc and the continent, (2) beginning of closure of the marginal basin, formation of an Andean-type arc and migration of the subduction zone westward and (3) complete closure of the marginal basin, formation of the Kabus ophiolitic mélange and erosion of the Andean-type arc.

Abdelsalam and Dawoud (1991) concluded their work by discussing the nature of the Ingessana ophiolite and the high-grade gneisses situated between it and the northeast Nuba Mountains and concluded that the western boundary between the ANS and the continental crust to the west is defined by the Kabus ophiolitic mélange.

<table>
<tr><th>Vail (1973)</th><th>Sadig and Vail (1986)</th><th>El Ageed and El Rabaa (1981)</th><th>Brinkmann (1986)</th></tr>
<tr><td>Intrusion of ring complexes and dykes</td><td rowspan="5">Cover rocks:
3-Quaryernary Umm Ruwaba formation
2-Cretaceous Nubian Sandstone formation
1- Nawa-Abu Habil deposits</td><td rowspan="6">Younger Intrusive</td><td>F_3 – Faulting and cataclasis and final volcanism (20 Ma)</td></tr>
<tr><td>Folding, N-S to NE, and metamorphism (greenschist facies) and cataclasis (?)</td><td rowspan="2">Intrusion of anorogenic alkali complexes (250 – 220 Ma) and dykes</td></tr>
<tr><td>Extrusion of meta-volcanic unit</td></tr>
<tr><td>Intrusion of late-orogenic granitoids</td><td>Intrusion of alkali complexes</td></tr>
<tr><td>Deposition of graphitic siltstones, mudstones and possibly limestones and andesite</td><td>End of F_2</td></tr>
<tr><td>Folding (NNE-SSW), metamorphism (amphibolites facies) and granitization</td><td>Anorogenic alkali ring-complexes</td><td>Intrusion of Late-orogenic granites (about 700 Ma)</td></tr>
<tr><td>Intrusion of gabbro (?)</td><td>Syn-to late-orogenic batholithic granitoids</td><td>Intrusion of gabbro</td></tr>
<tr><td>Deposition of psammites, shales, limestones and possibly rare volcanic rocks</td><td>Volcano-sedimentary unit:
Intercalated metavolcanic (meta-andesite and chlorite schist) and metasedimentary (pyroclastic strata)</td><td>Metavolcanic:
2- Meta-acidic volcanic
1- Meta-basic volcanic which include a chromiferous serpentinite</td><td>Collision of island arc; Emplacement of oceanic crust slivers (ophiolite) (F_1), start of folding (F_2), and intrusion of syn-orogenic batholiths (about 1000 Ma)</td></tr>
<tr><td>Erosion</td><td>Meta-sedimentary unit:
Paragneisses, psammites and mica and graphitic schists</td><td>Meta-sediments:
9- Graphitic-quartzofeldspathic schists
8- Quartzofeldspathic schists
7- Tremolite marbles,
6- Amphibolite schists,
5- Calc-semipelites
4- Grey marble,
2- Quartz-muscovite schists,
1- Graphitic schists.</td><td>Deposition of sediments (black shales with ferruginous cherts, carbonates, scarce conglomerates and arkose) with minor intercalated intermediate to acidic volcaniclastic (island arc setting)</td></tr>
<tr><td>Formation of granitic gneiss</td><td>Quartzo-feldspathic gneiss:
Hornblende augen gneiss, granodioritic gneiss,
and muscovite biotite gneiss</td><td>Hornblende gneiss</td><td>Extrusion of predominantly basic volcanic rocks with intercalated intermediate to acidic volcaniclastics and ferruginous cherts, deposition of carbonate (island arc setting)</td></tr>
</table>

Tabel 1-1: Summary of the different lithostratigraphic succession proposed for the Nuba Mountains.

1-5-6 other studies relevant to the Nuba Mountains:

Harris et al., (1984), in their studies of the relationships between the various lithological units in northeastern and east of Africa, have presented the results of Nd isotope data of the major Pan-African lithologies including data from the Nuba Mountains (El Obeid muscovite granite, Rashad and El Abbassiya syn-tectonic granites) which show a Paleoproterozoic crustal age for the former and a Pan-African age for both of the latter. Harris et al., (1984) interpreted the age obtained from El Obied as indicating either a Paleoproterozoic age or a mixture between Archean and Pan-African material.

Curtiz and Brinkmann (1985) have studied the post-tectonic units of the lithostratigraphic succession (Younger intrusive) of the Nuba Mountains. They focused on the main occurrences of the younger intrusive alkali complexes in the Nuba Mountains that are exposed in the southwestern part of the Nuba Mountains where more than 25 individual igneous complexes crop out covering a total area of 12000 km^2 along a 200 km long northwesterly trend between Jebel Talodi and Jebel Lagowa. Curtiz and Brinkmann (1985) provided detailed maps accompanied by their geological and geochemical descriptions.

1-6: Work on the Saharan Metacraton:

The Precambrian basement of northeast Africa is divided mainly into two tectonic regimes; an older sialic continental plate (Nile Craton, Rocci, 1965; Saharan-Congo Craton, Kröner, 1977; Eastern Saharan Craton, Bertrand and Caby, 1978; Central Sahara Ghost Craton, Black and Liégeois, 1993; Saharan Metacraton, Abdelsalam et

al., 2002) and the Neoproterozoic Pan-African Arabian Nubian Shield (Gass, 1981; Shackleton, 1979; Vail, 1983).

The latter region is well-studied and has relatively well-known geographic extents, consistent lithology, isotopic and geochronologic signatures and a widely accepted tectonic model of development. However, the older sialic continental crust is still lacking detailed geological work, no agreement on its boundaries has yet been reached, and little is known about its geochronology and isotopic characteristics.

After examining the available geological, structural and geochronological data of the sialic continental crust, Abdelsalam et al., (2002) revised and rejected the use of the term 'craton' on the basis that the prolonged history of deformation of this crust since the Neoproterozoic is no longer characteristic of cratonic behaviour. Therefore, the use of the term craton is misleading since the available geochronological and radiogenic data suggest that the region is no longer stable continental crust but was mostly remobilized during the Neoproterozoic orogeny (Abdelsalam et al., 2002, and references therein). Terms used to describe this crust, such as the Nile Craton (Rocci, 1965); Saharan-Congo Craton (Kröner, 1977); Eastern Saharan Craton (Bertrand and Caby, 1978) may therefore be inappropriate and/or these terms do not satisfy the geographic location of the region (Nile Craton and Eastern Saharan Craton suggest the area is too far to the east). Alternative terminology is not well-defined and not widely accepted (e.g. Central Sahara Ghost Craton). Instead, the term Saharan Metacraton (SMC) was proposed to describe the area by Abdelsalam et al., (2002).

The SMC is bounded to the east by the ANS and to the west by the Tuareg shield, the southern boundary is considered as the southern boundary of the Oubanguides orogenic belt and the northern boundary is hidden under the thick Phanerozoic cover of northern Africa (Fig. 1-3).

High to intermediate-grade gneisses, meta-sediments, migmatites and localized patches of granulites make up most of the SMC. Occurrences of low-grade volcano-sedimentary sequence (similar to those of the ANS) are occasionally reported.

Pre-Neoproterozoic ages for the SMC lithologies were first suggested, based upon their high-grade of metamorphism and further evidence derived from some Rb/Sr isochrons, Nd model ages, and U/Pb ages and from Sr and Nd initial ratios (Harris et al., 1984; Kröner et al., 1987; Sultan et al., 1994; Stern et al., 1994; Liégeois et al., 1994) which indicate the participation of Paleoproterozoic or possibly Archean crustal material within the protolith of these rocks. On the other hand, Rb/Sr, Sm/Nd and U/Pb zircon age data have also shown that parts of the SMC were formed and/or remobilized during the Neoproterozoic (Meinhold, 1979; Barth et al., 1983; Ries et al., 1985; Curtis and Lenz, 1985; Kröner et al., 1987; Key et al., 1989; Harms et al., 1990, 1994; Stern and Dawoud, 1991; Black and Liégeois, 1991; Stern et al., 1994; Liégeois et al., 1994).

Due to the enormous size of the SMC (about 5,000,000 km^2), it is understandable that several tectonic events and processes might have destabilized the region (Liégeois et al., 2013). Collision events t took place at the end of the Neoproterozoic in the SMC around the entire perimeter; at the eastern edge against the ANS, against the Taureg shield at the west, against the Congo craton at the south and against an unknown

craton in the north. These multiple collisions did not allow for tectonic escape and hence led to the decratonization of the interior and added much to the complexity of structures in the Saharan Metacraton. Abdelsalam et al., (2002) listed two major structural trends that have been reported in several areas within the Saharan Metacraton; an older ENE-trend, widely known as the Zalingai fold belt (Vail, 1976; Schandelmeier et al., 1987) which is interpreted to represent a Pre-Neoproterozoic structure in Central Africa (Abdelsalam et al., 2002 and references therein) and a younger N-S trend of the Neoproterozoic Keraf suture. In the Bayuda Desert Küster and Liégeois (2001) interpreted this structural trend to be inherited from terrain collision in the early Neoproterozoic.

N-S-trending structures were identified in various areas within the Saharan Metacraton and they are present in various manifestations: In the vicinity of the Keraf suture (the boundary between the ANS and the SMC), N-trending upright folds were later deformed by N- to NW-trending strike-slip faults; In the Bayuda Desert of northern Sudan, N-trending shear zones deformed the high-grade gneisses (Abdelsalam et al., 2000). N-S trending structures on the SMC are also present as N-trending fold and thrust belts in northern Chad and southern Libya (Tibesti massif), and in northern Sudan (Jebel Rahib) (Schandelmeier et al., 1990; Abdel-Rahman et al., 1990). Structures with similar trends were reported as far away as northern Cameroon where they were suggested to be younger than 620 Ma from U/Pb zircon data (Toteu et al., 1987).

The presence of fold and thrust belts were interpreted as relating to the opening and closing of restricted oceanic basins with or without the development of a subduction zone and volcanic arcs (Schandelmeier et al., 1990; Abdel-Rahman et al., 1990).

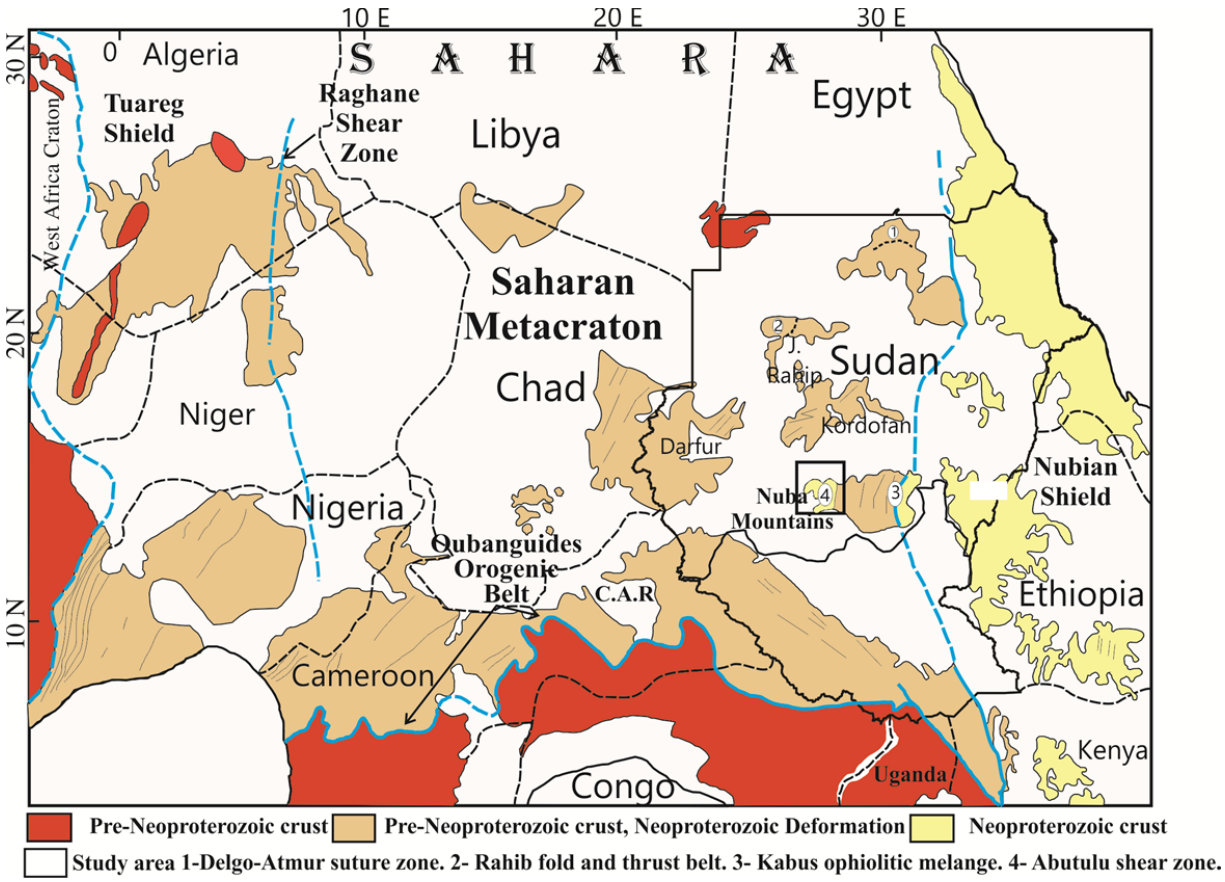

Figure 1-3: Location map of the Saharan Metacraton showing, Jebel Rahib, Atmur Delgo, Kabus and Abutulu areas (modified after Abdelsalam et al., 2002).

The opening and closure of these oceanic basins is one of the mechanisms that could account for the existence of the low-grade metavolcano-sedimentary sequence described later in this work.

In the western part of the Saharan Metacraton Fezaa et al., (2010) recognized the Murzuq Craton. The surface geology of the Muzruq Craton is coincident with the circular Muzruq Phanerozoic basin. Liégeois et al., (2013) suggested that the Murzug, the Al Kufrah and the Chad cratons are all remnants of the SMC and adjacent metacratonic areas, based upon their similarities (Fig. 1-3). This juxtaposition between the cratons and metacratonized area is a criterion of a metacraton that formed through the metacratonization of the inner part of a former craton (Liégeois et al., 2013).

The remobilization of the SMC was in the form of deformation (Vail, 1971, 1972, 1976; Schandelmeier et al.,1987; Denkler et al., 1994; Harms et al., 1994; Abdelsalam et al., 1995, 1998, 2000; Küster and Liégeois (2001), metamorphism (Kröner et al., 1987; Stern and Dawoud, 1991; Denkler et al., 1994), emplacement of igneous bodies and extension (Harms et al., 1990, 1994; Stern et al., 1994; Sultan et al., 1990, 1992, 1994), and formation of limited oceanic basins and further closing of the basins and collision of the drifted blocks (Schandelmeier et al., 1990, 1994; Abdel-Rahman et al., 1990; Stern et al., 1994). Four models were suggested to explain the remobilization of the Saharan Metacraton during Neoproterozoic time; 1- collision processes; 2- sub continental mantle lithosphere delamination; 3- extension tectonics; 4- assembly of the metacraton from exotic terranes.

1-7 The Eastern Boundary of the Saharan Metacraton:

A tectonic contact is believed to separate the Sahara Metacraton from the Arabian Nubian Shield. Vail (1985; 1988) suggested that the contact is defined by a belt of deformed supra-crustal meta-sediments that overlie the high-grade gneiss of the craton (now the SMC) and traced it from the Sekerr – Karamoja – Kapoeta region of northern Kenya and South Sudan through the Ingessana – Kurmuk region of southeastern Sudan to eastern Bayuda desert of northern Sudan. Abdelsalam and Dawoud, (1991) have shifted the boundary in central Sudan westward and redefined it as the Kabus ophiolitc mélange rather than the Ingessana – Kurmuk region. In the northern part of Sudan, the eastern boundary of the SMC is marked by the Keraf suture zone (Almond and Ahmed, 1987; Abdel Rahman et al., 1993; Abdelsalam et al., 1995 and 1998).

After recognizing that most of the Bayuda desert is underlain by juvenile Neoproterozoic crust Küster and Liégeois (2001) argued that the eastern boundary of the SMC should lie somewhere to the west of the Zalingei fold belt, unless the Bayuda desert area was thrust westwards over the eastern margin of the SMC. At the intersection between the Nakasib (a late-Proterozoic suture between the Haya and Gebeit terranes of the ANS) and the Keraf (Neoproterozoic suture that separates the ANS from the SMC) sutures Ali and Abdel Rahman (2010) identified new ophiolitic occurrences to the east and west of the Keraf suture. These occurrences generally line up along a NE- trending lineament, although part of it is affected by the sinistral movement of the Keraf shear and rotated to parallelism with the N-trending Keraf structures. Ali and Abdel Rahman, (2010) suggested that these ophiolitic occurrences may represent the continuation of the Nakasib ophiolite to the west of the Keraf suture. This suggestion should be treated with

care, since the relative sinistral movement along the Kerarf, which is estimated to be 1000 km (Küster and Liégeois (2001) rendered impossible correlation between the terranes east and west of it (although it supports the notion of Küster and Liégeois (2001) regarding the location of the contact between the SMC and the ANS).

1-8 Present Study:

1-8-1 Statement of the Problem:

The presence of Neoproterozoic Pan-African low-grade rocks within general high-grade (upper amphibolite facies) gneisses and schists of the Saharan Metacraton, have always been considered problematic in the sense that the low-grade metavolcano-sedimentary rocks are similar to the assemblages of the Arabian Nubian Shield. Vail (1983, 1986) suggested that they might be detached from the Arabian Nubian Shield. Studies in the northern and central parts of Sudan on similar outcrops have suggested variable tectonic models. These models involve rifting, formation of oceanic basins (usually restricted) and then closure of these basins with or without the formation of subduction zones and arc materials. The final stage is the collision between the different terranes on both sides of the former basin. Former studies also helped in understanding the significance of the different models in the destabilization of the SMC during the Neoproterozoic time.

The low-grade volcano-sedimentary sequence of the western Nuba Mountains has long been reported in the literature and still remains one of the few unstudied occurrences within the Sudanese section of the SMC.

In some instances early Neoproterozoic high-grade assemblages are found at the margin of the Metacraton as in the case of the Bayuda desert and are considered as different oceanic entities to that which exists between the SMC and the ANS (Küster and Liégeois (2001).

1-8-2 Objectives:

The overall objective is directed toward a better understanding of the low-grade volcano-sedimentary sequence of the western Nuba Mountains and their regional extents and geotectonic environment.

The detailed objectives are:

1- To conduct detailed geological mapping of the area around Jebel Abu Tulu in order to determine the extent and the structural relations of the low-grade metavolcano-sedimentary assemblage as well as the field relationships between this low-grade assemblage and adjacent rock units.
2- Lithological characterization of various rock units within the study area.
3- Documentation of the structures of the low-grade metavolcano-sedimentary assemblage and testing of existing models proposed for similar occurrences within the SMC.
4- Geochemical (rock and mineral chemistry), geochronological and isotopic characterization of the major lithologies in the study area.

Detailed description of the methodologies followed in the current study is provided in Appendix (1-1).

2- Regional Geology and Petrography:

2-1 Regional Geological framework of the Nuba Mountains:

The Nuba Mountains region (NMR) is located in the southern part of Sudan (Fig. 2-1) and comprises an inlier of uplifted crystalline basement, which is surrounded by Mesozoic to Cenozoic sedimentary rocks filling several grabens (Sadig and Vail, 1986; Browne and Fairhead, 1983).

Early studies in the region by Vail, (1973), Shaddad et al. (1979), El Ageed and El Rabaa (1981) and Sadig and Vail, (1986) have divided the crystalline basement rocks into high-grade gneisses and schists, low-grade metavolcano-sedimentary sequences and syn- to late-orogenic granitoids. The latter have intruded both of the former units (Fig.2-1). The presence of ultramafic rocks in the northeast of the Nuba Mountains was first described by El Ageed (1974) and these were identified as ophiolites by Hirdes and Brinkmann (1985), Brinkmann (1986) and Steiner (1987).

Abdelsalam and Dawoud (1991) have described these ophiolite fragments as a NNE-trending ophiolite-decorated suture zone. They introduced the name “Kabus ophiolitic mélange” and considered them to represent the eastern boundary of the SMC which separates the high-grade gneisses in the west from the low-grade volcano-sedimentary sequence in the east (Fig. 2-1).

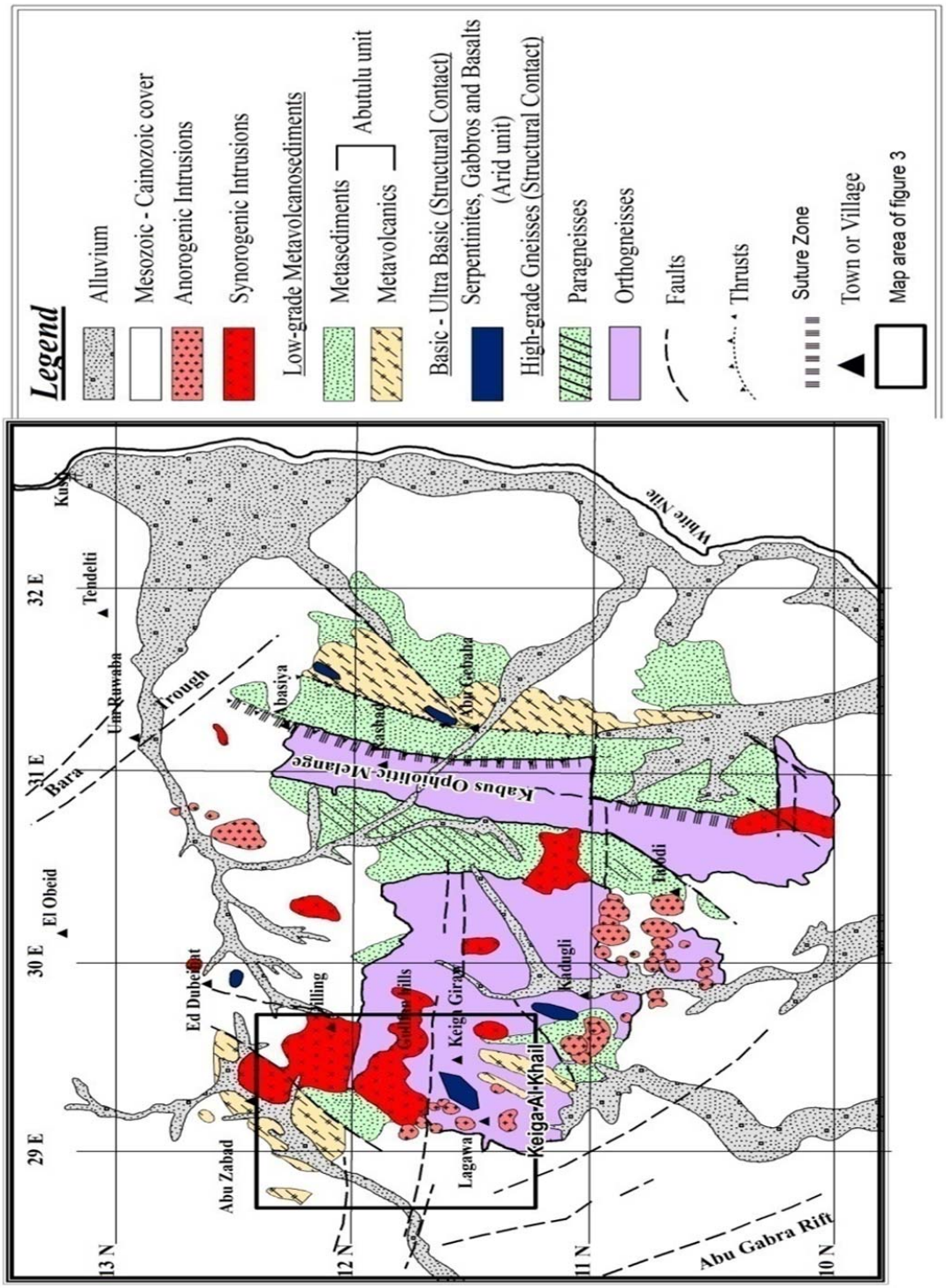

Figure 2-1: Geological map of the entire Nuba Mountains region (Modified after Sadig and Vail, 1986).

Although most of the region to the west of the Kabus ophiolitic mélange is underlain by amphibolite facies gneisses, the existence of low-grade greenschist facies meta-volcanic and meta-sedimentary rocks has long been reported at several localities in the western Nuba Mountains (Sadig and Vail, 1986). Small bands of meta-andesite surrounded by gneisses near Kega Al Khail (Fig. 2-1) have been reported by El Nadi (1984), while further to the north in the vicinity of Abu Zabad and around Abutulu (Fig. 2-1) similar meta-volcanic rocks and low-grade phyllites are present {Mansour and Iskander, (1960) and Almond (1983) in Sadig and Vail, (1986)}.

These low-grade meta-volcanic and meta-sedimentary rocks are geographically associated with several mafic masses first reported by Lyns and Campbell Smith (1921), Vail (1973) and Sadig and Vail (1986). These mafic occurrences have been considered by Vail (1973), as mafic intrusions that followed the metamorphism of the crystalline gneisses. However, this interpretation has not been adopted by this same author in a more recent publication (Sadig and Vail, 1986).

2-2 Geology of the western Nuba Mountains:

The area under consideration is situated in the westernmost Nuba Mountains and bounded by latitudes 11˚ 9′ 0″ and 12 ˚ 0′ 0″ N and longitudes 28˚ 32′ 0″ and 29˚ 40′ 0″ E covering an area of 11,910 km^2 (Fig. 2-2). Detailed geological mapping was carried out at the scale of 1:50000 utilizing ETM 7+ and Landsat8 Landsat images.

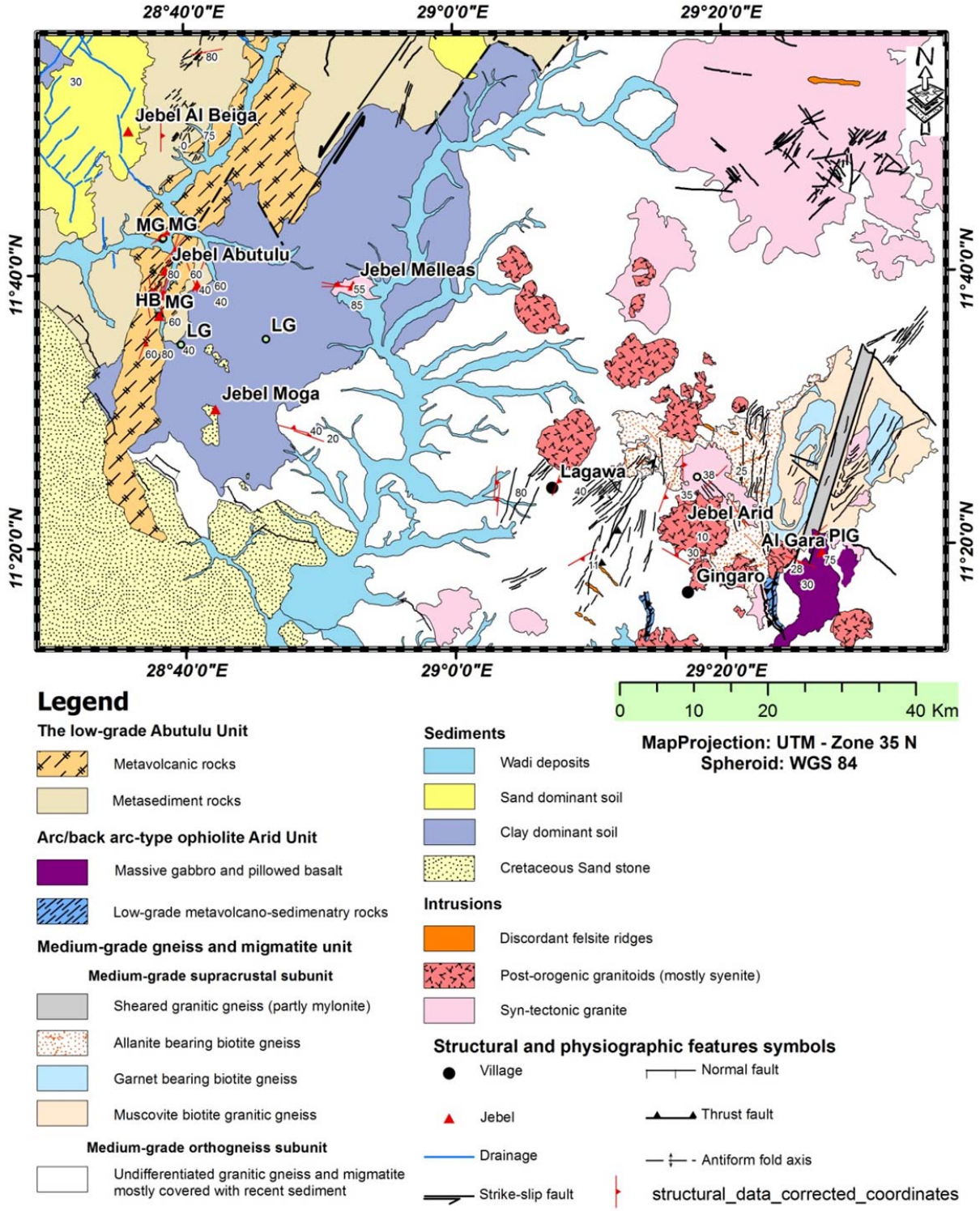

Figure 2-2: Detailed geological map of the western Nuba Mountains.

Several mapping tours revealed six lithostratigraphic units: gneisses and migmatites, a metavolcano-sedimentary sequence, an extrusive and intrusive mafic belt, syn to late-orogenic granitoids, anorogenic granitoids, and Mesozoic sedimentary rocks. All of the lithological units (except the Mesozoic sedimentary rocks) are aligned along N- and NNE-trending belts.

2-2-1 Medium-grade gneiss and migmatite:

2-2-1-1 Ortho-granitic and monzonitic gneiss:

Gneissose foliated banded rocks of granitic and granodioritic compositions occupy most of the eastern part and a portion of the centre of the study area. Sadig and Vail (1986), Mansour and Samuel (1957), Vail (1973), Brinkmann (1982) and Shaddad et al. (1979) have reported similar lithologies from areas in the eastern Nuba Mountains and in parts of the western Nuba Mountains. The gneisses crop out typically as low-lying features and in a few cases as hilly outcrops. They do not form any sort of lineament on the Landsat images and aerial photographs.

The gneissic granite is coarse-grained, foliated and contains strained quartz (30%), microcline (25%), orthoclase (5%), plagioclase (albite – oligoclase) (15%) and biotite (20%). Secondary minerals include sericite, carbonate, epidote, zoisite and chlorite. Accessory minerals include zircon, apatite, titanite and opaque minerals. In the gneissic granodiorite, hornblende increases at the expense of biotite and constitutes up to 10% of the rock. In some samples, plagioclase is the only feldspar with minor microcline perthite. K-feldspar augen gneiss occurs only in the western part of the mapped area (Plate 2-1). The mineral assemblage of oligoclase + microcline + biotite + hornblende

indicates amphibolite facies of regional metamorphism (Best, 2003). Later retrograde metamorphism is indicated by the formation of chlorite after primary hornblende and biotite, and the formation of epidote after primary plagioclase. The homogeneity of the granite and granodiorite suggests their magmatic origin.

The eastern contact of the high-grade ortho-gneisses is reported to be against the Kabus ophiolitic mélange about 300 km to the east (Abdelsalam and Dawoud, 1991). Diffuse and gradational contacts separate the gneisses from syn-orogenic granite of similar composition. Due to the nature of the contact between the two units, Sadig and Vail (1986) have described the difficulty in estimating the ratio between the gneisses and the syn-orogenic granite and suggest that portions of the latter might be misinterpreted as gneisses. This difficulty is confirmed in this study and most of the investigated previously-mapped gneiss occurrences have been found to be late to syn-orogenic granites containing numerous xenoliths of the older gneiss units. Basic xenoliths oriented parallel to the foliation planes are seen in syn-orogenic granite just a few kilometers to the WSW of Lagawa (Plate 2-2). The contact against the low-grade volcano-sedimentary unit to the west is demarcated by a steeply dipping sinistral shear zone. A sharp tonal contrast seen on the Landsat image denotes the contact. A sharp contact against the younger anorogenic granitoid intrusions is present and dykes of the younger intrusions are widely encountered near the intrusions. Detailed mapping of the younger intrusions and description of the nature of the contacts against the basement were given by Curtis and Brinkmann (1985).

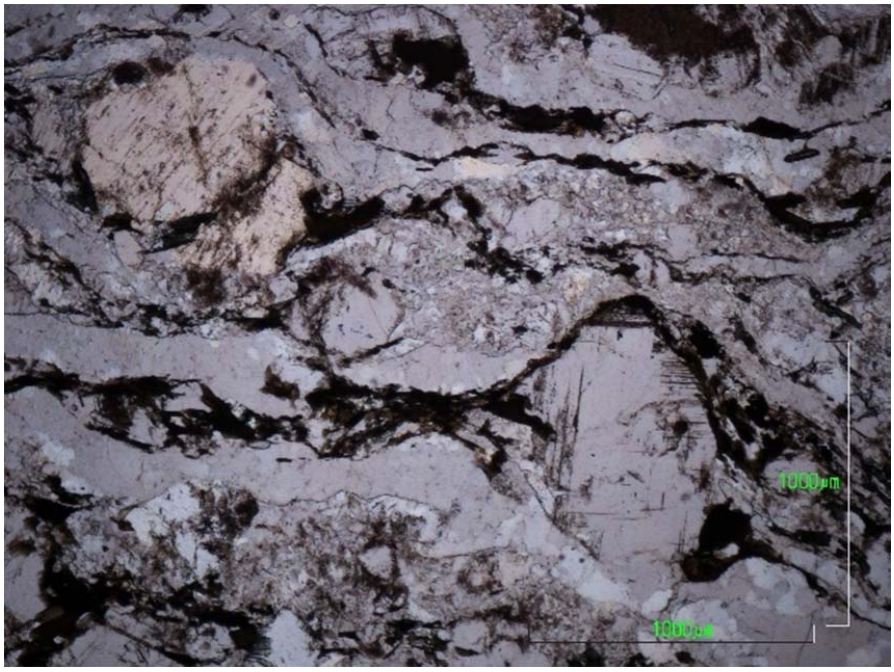

Plate 2-1: Augen gneissic granite from the western part of the study area, with orthoclase and microcline perthite porphyroblast crystals.

Plate 2-2: Basic xenolith within the syn-orogenic granite.

2-2-1-2 Low to medium-grade Supracrustal meta-sedimentary rocks:

N- to NNE-trending, moderately to steeply dipping narrow strips of intercalated meta-sediments (chert, graphite schist, graphitic-mica schist, quartz-feldspathic schist and gneisses) together with massive acidic and basic meta-volcanic rocks are reported in this study less than seven kilometers to the east of Jebel Arid and to the northwest and to the south of Jebel Keiga Al Kail. The meta-sedimentary units generally show primary layering and shallow (≈30°) south-southwesterly plunging stretching lineations, restricted to the quartzofeldspathic lithologies at the interface between the meta-sediments and the gneisses. In many locations the stretching lineations are the only structural fabric identified leading to strong L-tectonite quartzofeldspathic lithologies. The coarse varieties of the quartzofeldspathic lithologies show a planar fabric that grade into a gneissic fabric at the margin with the orthogneisses. Despite the changes in the direction of strike of the meta-sediments the direction of the stretching lineation remains consistent which possibly suggests it was developed at a later stage. The meta-sediments are affected by brittle deformation along NE-trending faults.

The paragneisses are made up of quartz, microcline, plagioclase (albite and/or oligoclase), muscovite and minor biotite. Garnet and allanite exist in some samples (Plate 2-3). The quartz has strong undulose extinction and the plagioclase shows twisted lamellae and is commonly altered to sericite. Accessory minerals are zircon and apatite. In the calc-silicates the main minerals are calcite, diopside, wollastonite, brucite and talc (Plate 2-4). Low-grade varieties only contain calcite and minor serpentine. The migmatitic mesosome is made up of hornblende, biotite and clinopyroxene and the leucosome is made up of plagioclase (oligoclase) and quartz. Epidote, apatite and

opaques are seen in both of the previous varieties. The unit is intruded by both syn-orogenic and anorogenic granitoids. A contact aureole has been recorded adjacent to impure marble.

Despite the petrographic difficulties in differentiating the protolith of quartzofeldspathic gneiss from magmatic rhyolitic tuffs or sedimentary lithic sandstone (Best, 2003), the inhomogeneity of the rocks is indicative of a sedimentary origin.

The mineral assemblage of the paragneisses (plagioclase+ K-feldspar+ muscovite + biotite) indicates amphibolite facies of regional metamorphism. The thermally metamorphosed impure limestone show mineral assemblages of slightly higher grade indicated by the presence of wollastonite in their mineral paragenesis (the presence of wollastonite indicating a H_2O dominated fluid phase environment – very low CO_2). The unit rock assemblage of quartzofeldspathic gneisses, quartzite and marble are all indicative of a shallow water shelf depositional environment.

The meta-sediments can easily be recognized on Landsat images by their well developed NNE-trending lineament and a rectangular drainage pattern that is most likely structurally controlled (Fig. 2-2). Thrust faults are thought to define the contact against the gneiss unit. This assumption is based on field observations where thrust faults were noticed in the last observed eastern- and western-most outcrops of the meta-sedimentary rocks.

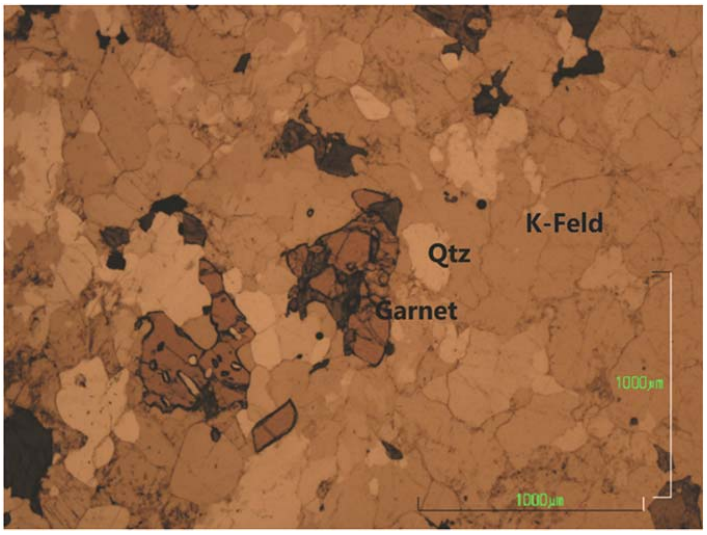

Pate 2-3: Garnet crystals in paragneiss north of Jebel Arid.

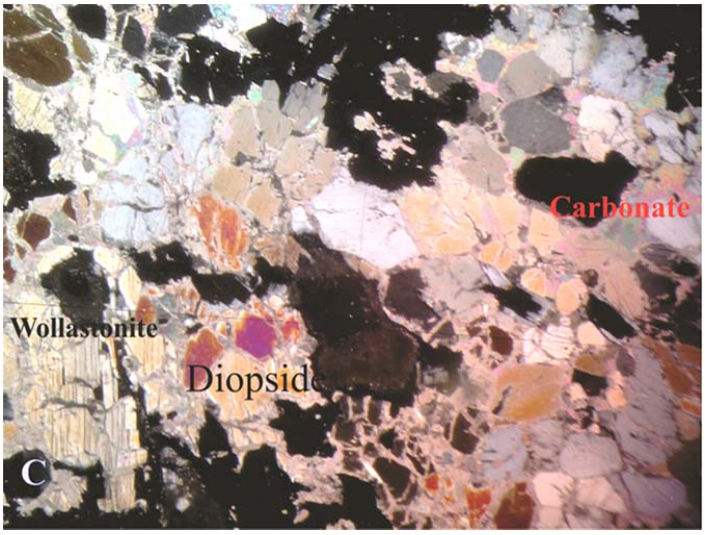

Plate 2-4: Calc-silicate of the supra-crustal subunit that shows mineralogy of diopside, brucite, talc and calcite.

The meta-sedimentary rocks are affected by major south-plunging, easterly-verging asymmetrical antiform folded along a N-S to NNE-SSW trending axis. Several northeast-trending strike slip faults have been observed.

2-2-2 Syn-orogenic granitoids:

Previous mapping shows that syn-orogenic granitoids form a very limited proportion of the surface geology of the NE Nuba Mountains, although they make up a considerable amount in the Arabian Nubian Shield, where they form substantial exposures of the Red Sea Hills and the southeastern area of the Bayuda desert.

The syn-orogenic granitoids were intruded into the medium-grade gneiss as well as the low-grade metavolcano-sedimentary rocks. In the northeastern Nuba Mountains Vail (1983) reported that the syn-orogenic granitoids also intruded the ophiolite sequence. Based on the T_{DM} Nd model ages obtained by Harris et al., (1984) from foliated granite and granodiorite intrusions of Rashad (1000 Ma) and Abbasiya (950 Ma), the emplacement age of the syn-orogenic batholiths was suggested to be around 1000 Ma (Brinkmann, 1986).

Within the area under consideration, no clear intrusive contact relationships are noticeable between the syn-orogenic granitoids and the arc/back-arc ophiolite of the Arid unit, despite the close proximity between the two units.

The rocks are generally homogenous in composition and only two main varieties can be recognized; a hornblende biotite granite and a muscovite biotite granite. The first type is only identified in the western part of the area in a locality named Umm Shair (approximately 12 km to the south of Jebel Abutulu). The outcrop is coarse-grained and

K-feldspar, quartz and biotite are easily recognized in hand specimen. The outcrop is highly charged with xenoliths of basic and felsic compositions. A well developed NW foliation (300/60NE) is identified all over the outcrop.

The biotite muscovite granite occurs in both the eastern and western part of the study area. In the eastern part it occurs as high relief outcrops surrounded by the Quaternary sand. The rocks are foliated (080/50SE) and laden with concentrations of mafic material (schlieren texture). The schlieren clustures are mostly aligned parallel to the dominant foliation plane.

The microscopic investigations reveal that the rocks are mainly composed of K-feldspar (microcline and orthoclase), plagioclase (mainly albite) and biotite. Muscovite exists in minor amounts as primary and/or secondary constituents. Hornblende substitutes some of the biotite in the hornblende biotite variety. Zircon, iron oxide, epidote and sphene occur are common accessories (Plate 2-5). Primary muscovite and hornblende are likely to be incompatible.

2-2-3 Pillow basalt, massive gabbros and layered gabbros (Arid units):

Dismembered low-lying fragments of pillow basalts, massive gabbros and minor layered gabbros are found to occupy a NNE-trending belt from Kadugli (Vail, 1973), north and northeast of Jebel Arid (this study) and 10 km SE of Ed Dubeibat (Lyns and Campbell Smith, 1921) (Fig. 2-2). Brinkmann (1986) have suggested that some of these gabbroic bodies are not related to the ophiolite unit and he attempted to draw a distinction between the two units based on their geochemistry. In the study area no contrasting

field relation is observable and further information can only be gained from geochemistry.

2-2-3-1 Layered gabbros:

The layered gabbros are greenish in colour with brown weathering surfaces, coarse-grained texture and show crude compositional layering (Plate 2-6). They were found in three exposures along the boundary between the metavolcano-sedimentary unit and the high-grade gneisses (Fig. 2-2). Although there is no obvious contact against the other units they are considered to be the lowest unit within the mafic sequence, based on their structure (layering) and spatial position (furthest to the NW in the SE-dipping sequence). Its exposure along Wadi Al Beida is in close geographic location to hornblendite occurrences less than few hundred meters to the NW along the same wadi (Fig. 2-2). The rocks are affected by 040°-oriented shear and show intrafolial folds that plunge steeply to the SE. In the Al Beida exposures they are found to be intruded by granite and cut by numerous veinlets of quartz.

Microscopically, the layered gabbro is coarse-grained, composed of plagioclase and clinopyroxene in approximately equal amounts. Deformed plagioclase displays twisted lamellae and poikilitic textures and is saussuritized to sodic plagioclase, epidote and sericite (Plate 2-7). The clinopyroxene is mostly retrograded to green hornblende and both are replaced by fibrous actinolite and chlorite. These relationships possibly suggest two metamorphic episodes; medium grade followed by low grade, though this may just be generalized retrogression – depending on textural relationships.

Apatite, sphene and iron oxides are the main accessory minerals. Epidote, zoisite, actinolite and chlorite are the main secondary minerals.

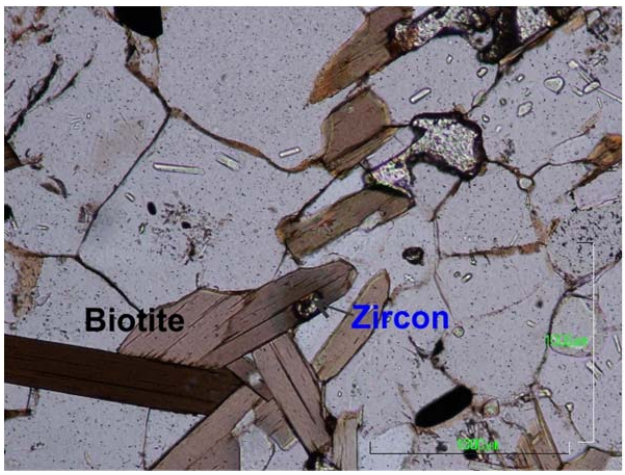

Plate 2-5: Inclusions of zircon within the biotite crystals in the syn-orogenic granite of Jebel Umm Shair.

Plate 2-6: Layered gabbro exposure to the east of Jebel Abutulu.

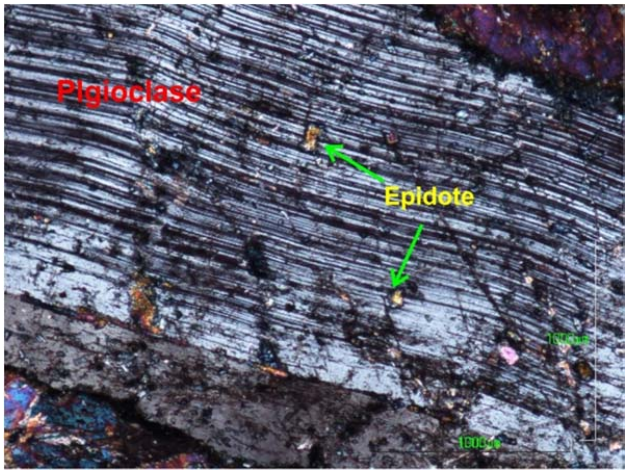

Plate 2-7: Deformed plagioclase of the layered gabbro showing formation of epidote and sericite.

2-2-3-2 Massive gabbros:

The massive gabbros outcrop as boulders of medium to coarse-grained rock which vary texturally from gabbroic to doleritic. They are predominantly massive, showing slight to no indication of foliation, but are slightly sheared locally. They have dark colours and some of them are melano-gabbroic. The massive gabbros are the dominant lithology among the mafic-ultramafic sequence; their main outcrop is in the core of a southerly-plunging asymmetrical antiformal structure about a kilometre to the NE of Jebel Arid (Fig. 2-2). The massive gabbro is made up mostly of saussuritized calcic plagioclase and approximately equal amounts of hornblende. Hornblende is retrograded after early clinopyroxene (augite). Uralitized clinopyroxene remains as relicts and is partially replaced along its margins and cleavage planes by green fibrous actinolite and chlorite. Orthopyroxene is evident in a few samples and is always associated with olivine. One sample (SK-207) shows fine- to medium-grained crystals of green primary hornblende which may represent near solidus crystallization in an ophiolite magma chamber (Coogan et al, 2001). The main secondary minerals are epidote, zoisite, actinolite and chlorite while apatite and iron oxides are accessory minerals. The massive gabbro in two localities (Al Greera outcrop and east of Abutulu) is associated with pods and dykes of plagiogranite (Fig. 2-2). The plagiogranite is light in colour and has a coarse-grained texture composed mainly of quartz and sodic plagioclase and minor amounts of biotite and iron oxide. Beside this outcrop, Sadig and Vail (1986) have reported numerous exposures of massive gabbros in the mapped area.

2-2-3-3 Basaltic lavas:

Basaltic lavas, rarely showing pillow structures, are underlain by massive gabbro northeast and east of Jebel Arid. The rocks are grayish green to dark green in color and fine-grained in texture. The pillows are of oval shape and reach ~30 cm in size (Plate 2-8).

Petrographically, the rocks are fine-grained in texture showing weak to well-developed foliations and are composed of plagioclase + amphibole (Hornblende/Actinolite) ± clinopyroxene + epidote ± zoisite ± sphene ± chlorite ± apatite ± iron oxide, with plagioclase and hornblende forming up to 90% of the rock (Plate 2-9). Hornblende appears green to dark green in color, usually forming hypidiomorphic long prisms but idiomorphic perfect cross-sections are frequently seen. Plagioclase is generally xenomorphic and occasionally shows twisted lamellae. Subsequent alteration and possible retrogression is evident by the presence of calcic plagioclase saussuritized to sodic plagioclase, epidote and quartz, with minor replacement of hornblende by chlorite. The general mineral assemblage of the metabasite indicates low-grade metamorphism in the epidote-amphibolite sub-facies.

2-2-4 Low-grade meta-volcanic and meta-sedimentary rocks (Abutulu unit):

This group of rocks underlies the westernmost area of the Nuba Mountains and is mostly composed of poly-deformed and metamorphosed meta-volcanic (dominantly meta-andesite and sub-alkaline-basalt) and meta-sedimentary rocks (slate, phyllite, graphitic and mica quartzitic schist). The western boundary of the unit is hidden under thick sedimentary rocks.

Plate 2-8: Basaltic lava with pillow structure.

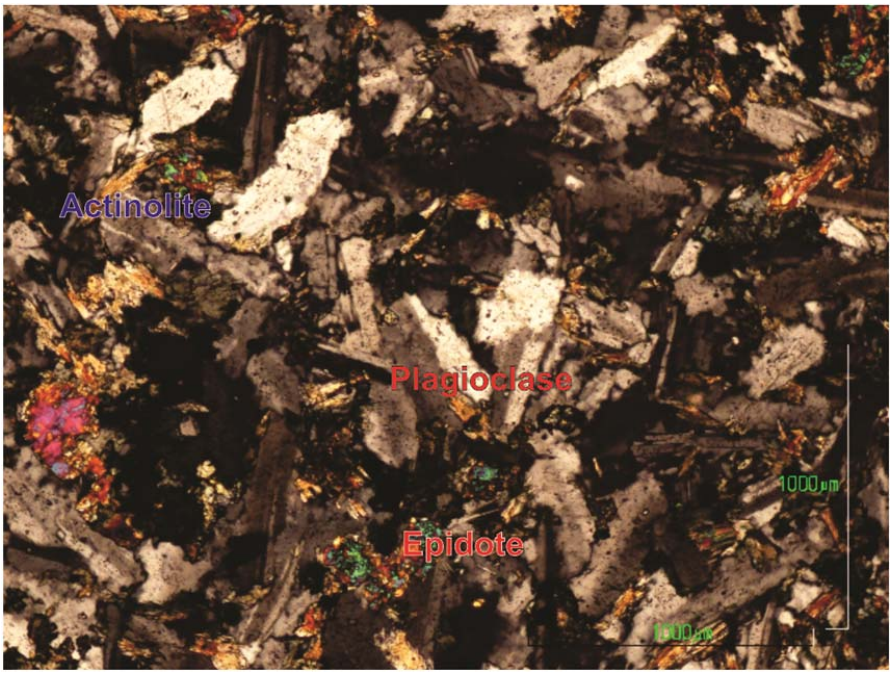

Plate 2-9: Photomicrograph showing the mineral composition of the pillowed basaltic lava.

A tonal contrast on Landsat images coincides with a sinistral shear and represents the eastern boundary separating them from the high-grade gneisses.

Establishment of a stratigraphic column within the unit is difficult since the nature of the outcrop is as isolated inselbergs surrounded by thick clay cover. However, in the Abutulu outcrop, the meta-volcanics overlie the meta-sedimentary rocks. The presence of a meta-volcanic exposure immediately west of Jebel Abutulu may indicate intercalation between the meta-sedimentary and the meta-volcanic units, like the general pattern observed in the Nuba Mountains. Both the units are sheared and folded along a general N30-50E strike but with more structural complexity in the meta-sedimentary rock. The structural pattern suggests sinistral transpression with a dominant strike-slip component and subordinate compression.

The mica quartz schist is fine-grained, well-foliated and banded with some lamellae rich in mica and the others rich in quartz. A flakey sericite band has been reported in parts of the southern part of the Al Beida outcrop. Graphite schist is the dominant lithology among the meta-sedimentary rocks and is reported in several localities from Kadugli in the south and northward thereof. The main locality in the study area is Tugula in the north of the mapped area and although highly folded and sheared, the primary sedimentary structures (bedding) can still be observed both at mesoscopic (Plate 2-10) and microscopic scales. Lenses of phyllite have been recorded within the Tugula lithology.

The meta-andesite main outcrop is at Abutulu (Fig. 2-2) where it flanks the meta-sedimentary rocks and appears as large and hard blocks of greenish grey color with no

joints. Other meta-andesite occurrences have only been seen as exposures along the dense network of drainage.

Petrographically, the meta-sedimentary rocks are fine-grained rocks and have a mineral assemblage of quartz, white mica, and graphite (Plate 2-11). Chlorite is the main accessory mineral, accompanied by biotite, epidote, apatite and iron oxides as accessory phases. Mansour and Iskander (1960) have reported a rare occurrence of glaucophane among the accessory minerals.

The meta-volcanic rocks have porphyritic to phanitic textures with plagioclase (mainly andesine) as porphyroblasts in a finer groundmass of plagioclase, actinolite, chlorite, relict clinopyroxene and biotite. In many samples chlorite replaces all the mafic minerals (Plate 2-12). Epidote, zoisite, muscovite and quartz are the main secondary minerals. Apatite and opaques are the accessory minerals. Veinlets of carbonate and hydrothermal quartz (with poorly developed wavy extinction) are frequently observed Igneous textures are widely seen (ophitic intergrowth). The general mineral assemblage indicates greenschist facies metamorphism.

2-2-5 Late-orogenic granitoids:

A distinction in the field between the syn-orogenic granitoids and the late-orogenic is not easily made. However the latter partly showing no foliation (especially in the margins of the outcrops) and they generally have a more outstanding relief.

Four occurrences of late-orogenic granite were observed in the study area. All four outcrops are restricted to the central part of the mapped area and they cut the medium-grade ortho- and paragneiss (Fig. 2-3) where they carry xenoliths of the gneiss.

Plate 2-10: Primary bedding (quartz rich and graphite rich layers) in the sheared meta-sediments of Jebel Tugula.

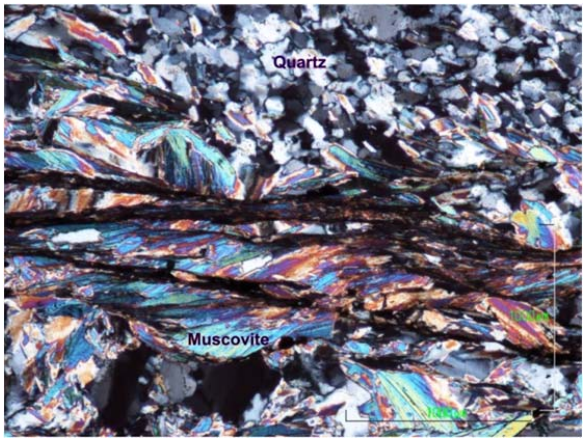

Plate 2-11: The mineral composition of the mica quartz schist of Jebel Al Beida. Notice the two foliation emphasized by the mica.

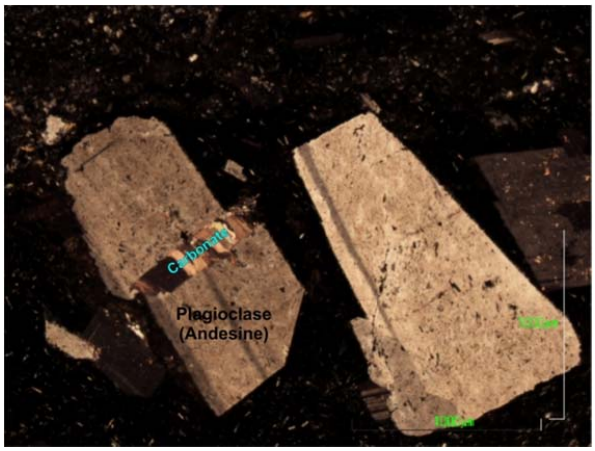

Plate 2-12: Microphotograph of the meta-andesite of Jebel Abutulu.

The occurrence in the southern part of the central area is represented by medium to coarse-grained equigranular to feldspar porphyritic granite with cross cutting veins of pegmatite that are composed of quartz, feldspar and hornblende. A northeast trending foliation with moderate northwest dips (020/36W) was recorded in the central part of the outcrop.

The west central occurrence exists as isolated hilly outcrops of up to 20 meter above surrounding plains and the individual outcrops are separated from each other by up to hundreds of meters distance. Planar fabrics grades from weak to well-developed foliations with an S-C fabric (plate 2-13). The shear plane (C-plane) is moderately north dipping (290/20N) while the mylonitic foliation (S-plane) is approximately horizontal and is defined by quartz and feldspar ribbons (plate 2-13). Strong slickenside lineations plunge gently (20° to 40°) to the north, and are usually associated with the foliation planes. Well-defined stepping is noticed on the C-plane, suggesting low-angle normal faulting. At the centre, the late-orogenic granitoids show absolutely no planar or linear fabric. The granitic rocks of these outcrops were used extensively as grinding surfaces for sesame seeds in the past (Plate 2-14).

Plate 2-13: S-C fabric developed in the western outcrop of the late-orogenic granite with approximately horizontal mylonitic foliation (C-plane) and a gently north dipping shear plane (S-plane).

Plate 2-14: Manmade pot holes in the late-orogenic granite utilized in the grinding of sesame seeds.

3- LITHOCHEMISTRY:

3-1 Samples and analytical techniques:

For the petrochemical studies 73 samples comprising 24 from the Arid unit (gabbro and pillow basalt), 15 from the Abutulu unit (meta-andesite and acidic meta-volcanic), 22 from the gneisses and syn-orogenic granitoids and 12 from late-orogenic granite were selected for major, trace and rare earth element (REE) analysis. Major and trace element concentrations were determined by X-ray fluorescence using an ARL9400XP+ spectrometer in the XRD – XRF analytical facility of the Department of Geology, University of Pretoria, using fused glass beads for major elements and pressed powder pellets for the trace elements. The limits of detection for the major elements were better than 1%. A group of 44 samples of the different units (except the post-orogenic granite) were selected for high-precision determination of trace and REE element concentrations by induced coupled plasma mass spectrometry (ICP-MS) in the analytical facilities of the Department of Geological Sciences, University of Cape Town, South Africa.

3-2 Alteration and testing of element mobility:

Petrographical examinations, as well as later determination of loss on ignition, (LOI) indicate that most of the samples have suffered from post-magmatic processes, including magma - sea-water interaction, regional metamorphism and later alteration. Elements are known to behave differently under such processes (Hart, 1970; Polat et al., 1999; Humphris and Thompson, 1978; Mottl, 1983; Wilson, 1989). This variation in element behavior during weathering and hydrothermal alteration is commonly attributed

to charge/radius ratio (ionic potential) (e.g. Pearce, 1996). Thus elements that form ions of low (<0.03 pm^{-1}) and high (>0.10 pm^{-1}) ionic potential tend to be preferentially removed in solution while elements that form ions of intermediate ionic potential (0.03-0.10 pm^{-1}) tend to remain in the solid product of weathering and so are relatively immobile; this is typically true even at greenschist-grade of metamorphism (Hastie et al., 2007). Thus the elements Zr, Hf, Nb, Ta, Y, Ti, Cr, REE except Eu and possibly La, Th, Ga and Sc are considered among the most relatively immobile elements (Hastie et al., 2007; Pearce and Cann, 1971, 1973; Pearce, 2008; Ahkol' nik et al., 2009).

However it is important for the mobility of each element to be tested since even the immobile elements may be mobilized under certain conditions, such as a change in the fluid composition, and/or an increase in temperature and/or extremely high fluid throughput (e.g. Hastie et al., 2007; Hynes, 1980; McCulloch and Gamble, 1991; Pearce, 1996; Hill et al., 2000).

In this study, the method described by Cann (1970) is implemented, in which an immobile element (Nb in this study) is plotted on the horizontal axis and the element to be tested on the vertical axis. If the elements are immobile and the samples are cogenetic, the data should give a trend with a slope close to unity.

Plotting of Hf, Ta, Y and Yb for samples of Arid and Abutulu units (Fig. 3-1) gave slopes that are close to unity indicating the immobility of these elements and the cogenetic nature of the two units.

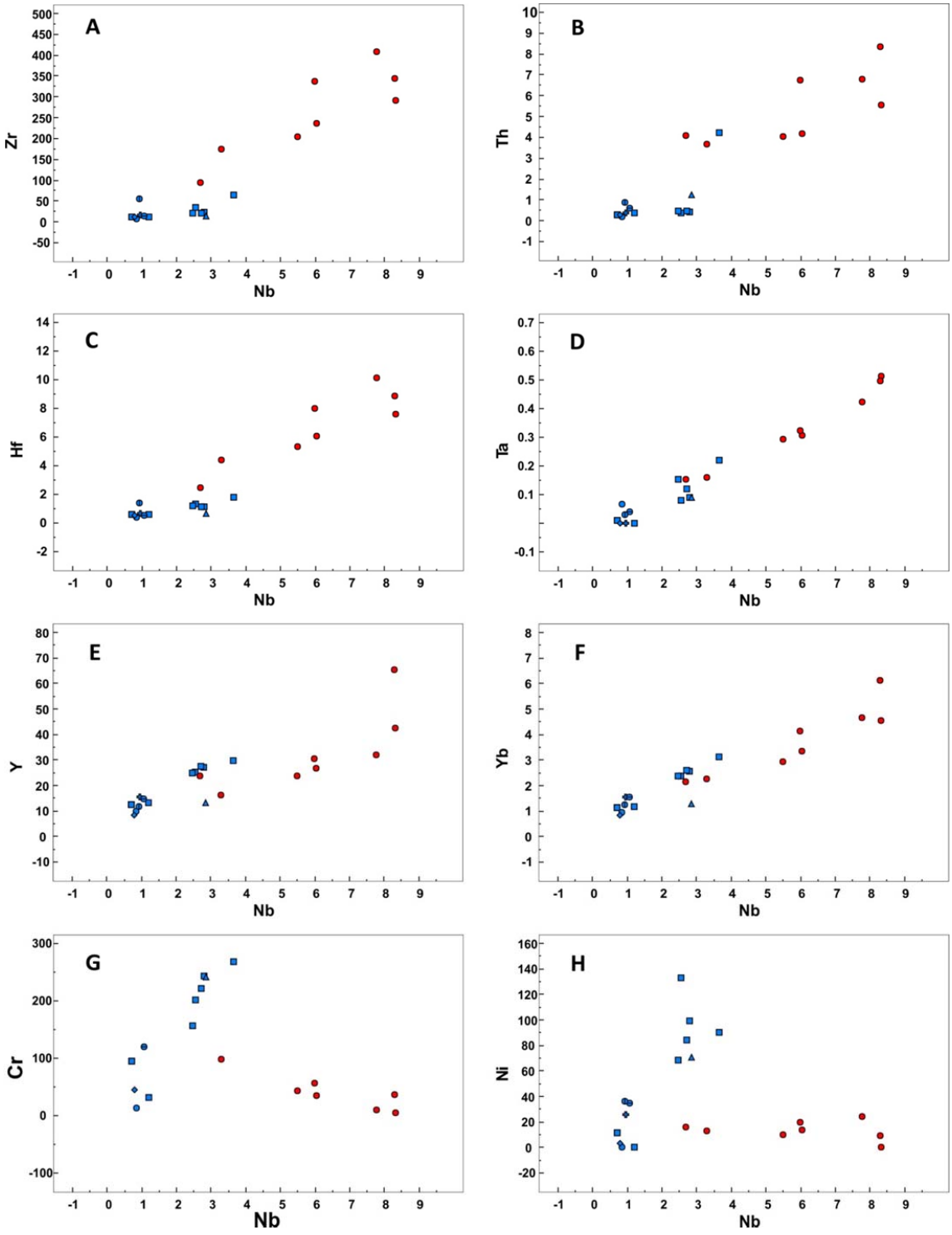

Figure 3-1: Plotting of various trace elements from the Arid unit (blue squares) and the Abutulu unit (red cycles) against Nb.

3-3 Major and trace element geochemistry:

Although the lithological, structural and spatial differences between Arid and Abutulu units have been described in the previous sections, the bivariate plotting of various elements from the Arid and Abutulu units against their Nb contents (Fig. 3-1) clearly indicate the cogenetic nature of the two units and thus suggests that the variation between these units could be explained by intra-formation differentiation.

Thus, in this section we will deal with the geochemistry of two units together. However, each lithological group will be assigned a unique symbol and will be discussed in a separate sub-section for the purposes of comparison.

The ortho-gneiss subunit and the syn-orogenic granite will also be discussed together. However, the late-orogenic intrusions will be presented and discussed separately.

3-3-1 Ortho-granitic gneiss and syn-orogenic granite:

Field observations, petrographical and geochemical data allow the identification of medium-grade gneisses of igneous derivation and those of sedimentary derivation. Monotonous, isolated intrusions of dominantly biotite gneiss with rare occurrences of hornblende – biotite gneiss varieties and rare secondary muscovite are interpreted as meta-igneous (ortho-gneisses). Muscovite – biotite, garnet – biotite and quartzo – feldspathic gneisses are part of interbedded sequence and considered as meta-sediments (paragneiss).

The ortho-gneisses have a wide silica range 64 - 75 wt %. The rest of the major elements have a compositional range as follows: 12.7 – 15.8 wt % Al_2O_3; 1.15 – 5.4 wt

% Fe_2O_3T; 0.01 - 1.31 wt % MgO; 0.3- 2.6 wt % CaO; 2.9 – 4.2 wt %; Na_2O and 4.4 – 6.0 wt % K_2O; (Appendix 3-1). The quartz monazite gneisses (two samples) have SiO_2 and Al_2O_3 contents (65 – 71 wt % and 15.9 – 21.2 wt % respectively) and only limited variation in the rest of the other elements. They have low averages of TiO_2 (0.06 wt %), Fe_2O_3 (0.07 wt %) and K_2O (0.12 wt %), similar content of MnO (0.03 wt %) and higher contents of CaO (5.4 wt %) and Na_2O (5.1 wt %). They are akin to a high K-calc-alkaline chemistry (Fig. 3-2). The calc-alkaline affinity of the samples is also indicated in the plot of the samples on an AFM diagram (Fig. 3-3). Utilization of the Frost et al., (2001) Na_2O+K_2O-CaO diagram (Fig. 3-4) shows the granitic and tonalitic samples plot in the in the fields of calcic alkali and alkali calcic fields.

The A/CNK ratios {molecular $Al_2O_3/(CaO+Na_2O+K_2O)$} of the granitic and tonalitic gneisses (Appendix 3-1) vary between 0.9 and 1.22, with an average of 1.07 suggesting that the samples are metaluminous to slightly peraluminous. The tonalitic gneisses hold the lowest A/CNK range (0.98 – 1.03). Plotting of P_2O_5 against SiO_2 for the granitic and tonalitic gneisses (Fig. 3-5) shows a negative correlation, a characteristic feature of I-type granite, and due to the low of solubility of apatite in metaluminous to slightly peraluminous melt (I-type) which decreases with increasing SiO_2 (Wolf and London, 1994; Chappell, 1999).

The Na_2O content of all of the samples is >3.0 wt %, a characteristic of I-type granite (Hine et al., 1978). High K_2O concentrations recorded in all of the samples leads to high K_2O/Na_2O ratios, (generally between 1.0 and 1.9). K_2O/Na_2O ratios close to 1 are typical of calc-alkaline rocks and higher ratios are indicative of contamination with evolved crustal material (Andonaegui et al., 2012)

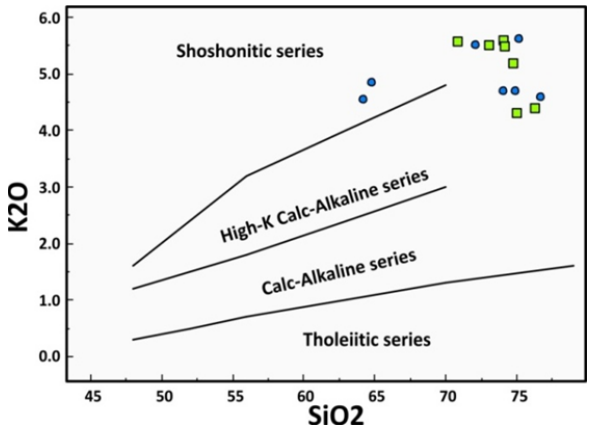

Figure 3-2: Bivariate plot of K_2O vs SiO_2. The diagram shows the subdivisions of Le Maitre et al., (1989). Orthogneiss (blue circle), paragneiss (red squares) and syn-orogenic granite (green squares).

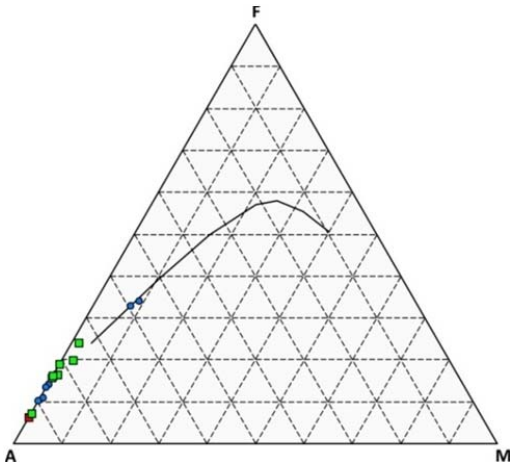

Figure 3-3: AFM diagram (Irvine and Baragar (1971)) showing calc-alkaline trend for the orthogneiss (blue circle), paragneiss (red squares) and syn-orogenic granite (green squares).

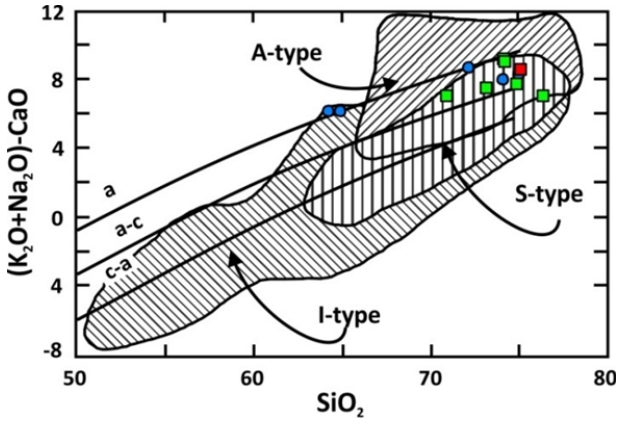

Figure 3-4: (K_2O+Na_2O)-CaO vs SiO_2 bivariate discrimination diagram of Frost et al., (2001). Orthogneiss (blue circle), paragneiss (red squares) and syn-orogenic granite (green squares).

Trace element concentrations are listed in Appendix 3-1a and 3-1b. Barium and Sr have a linear negative correlation with increasing SiO_2, suggesting fractional crystallization. The tonalitic gneisses host the highest concentrations of both elements > 2300 ppm and 550 ppm respectively and the granitic gneisses the lowest concentrations 286 and 39.6 ppm respectively. Nb shows a broadly positive correlation where Th, Zr and Y show no significant correlation (Fig. 3-5), possibly suggesting magma mixing.

On an N-MORB-normalized incompatible element diagram (Fig. 3-6a) all of the samples show a Nb – Ta negative anomaly and Sm, P, Ti, Y, and Yb depletion. These are characteristics of subduction related magmas (Pearce et al., 1995). The granitic gneisses (two micas) compare well with the muscovite-biotite gneisses of the Bayuda desert (Küster and Liégeois, 2001) while the tonalitic gneiss compares with the epidote-biotite gneiss of Bayuda desert. Both the granitic and quartz monzonitic gneisses show a higher depletion in P and Ti, slightly less depletion in Nb and Ta and higher concentration of Th when compared to Bayuda lithologies (Fig. 3-6a).

On chondrite-normalized rare earth element diagrams (Fig. 3-7a) the biotite gneiss has a high total rare earth element (∑REE) ranging between 731.6 – 193 ppm and has a negative correlation with increasing SiO_2. The samples show LREE enrichment patterns with La/Yb_N values ranging between 46.66 – 2.79, with a moderate to strong negative Eu anomaly Eu/Eu* 0.47 – 0.05.

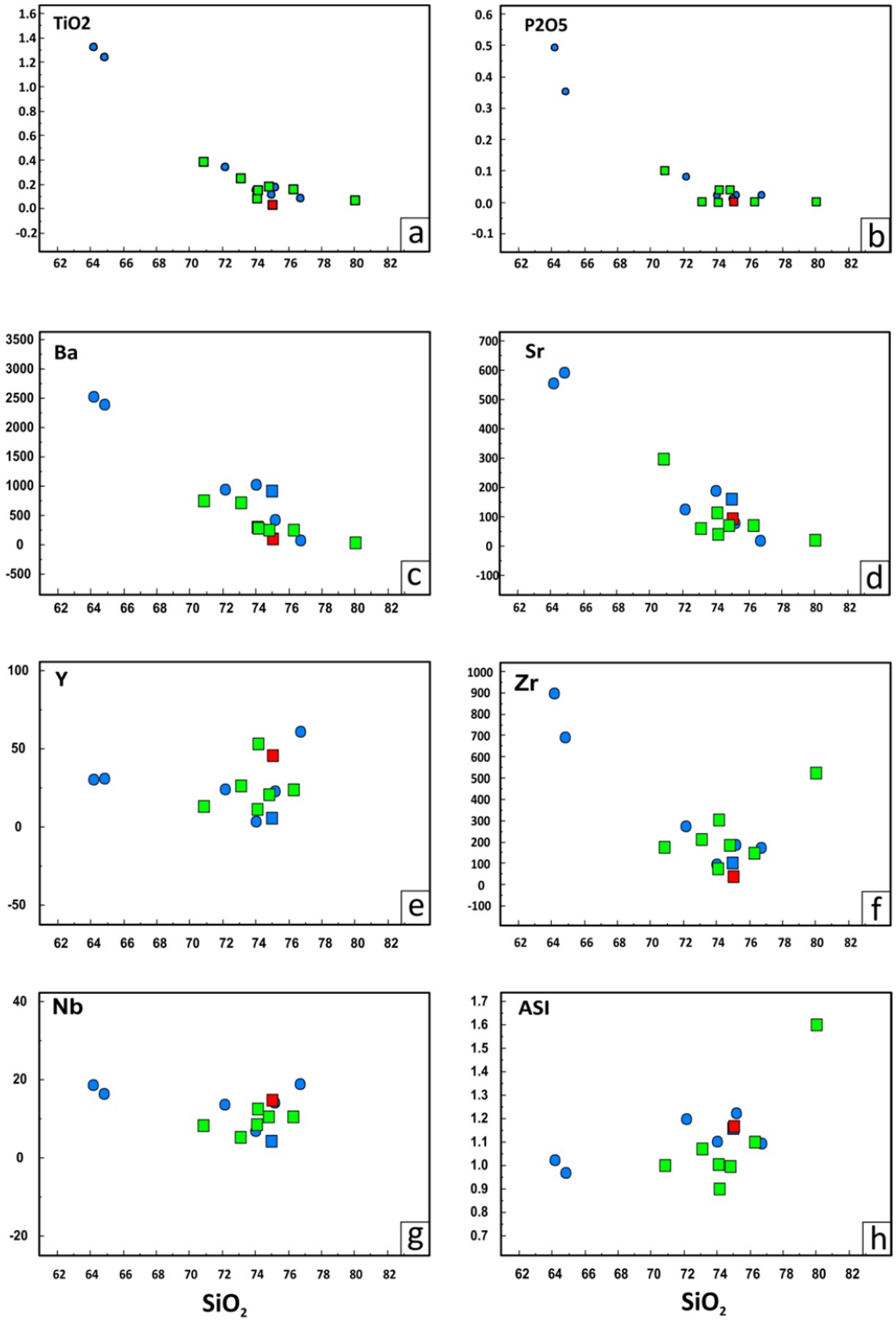

Figure 3-5: Bivariate plotting of major, trace and alumina saturation index versus silica. Green squares are the syn-orogenic samples, blue circles are orthogneiss samples and the red square is paragneiss sample.

The 2 mica granitic gneiss has a lower ∑REE value (188 ppm), a less fractionated pattern of La/Yb_N (27.7 – 10.5) and a negative Eu anomaly similar to the biotite gneiss (Eu/Eu^*_N = 0.33) and LREE enrichment pattern (La/Yb_N = 12.24). The metasedimentary garnet bearing sample (SK237) shows a different REE pattern (typical of fractionarion of HREE in garnet Rollinson (1993)) with HREE more than the LREE (Tb/Yb_N = 0.31) and holds the lowest ∑REE = 55.7. The SK237 share has a similar negative Eu anomaly (Eu/Eu* = 0.27).

The western Nuba Mountains orthogneisses are enriched in the large iron lithophile elements (LILE) and light rare earth elements (LREE) relative to the high field strength elements (HFSE) characteristic features of subduction related magmas (Fig. 3-6b) (Davidson, 1996; Tatsumi and Eggins, 1995). The enrichment in LILE is either due to fluid mobilization from the subducting slab or from melting sediments or crustal contamination. To test which of these possibilities apply in the investigated lithologies a Ba/Th vs Th bi-variant plot (Andonaegui et al., 2012) was implemented, since the Ba/Th ratio is enriched in the supra-subduction zone magmas affected by fluid from subducting plate and the Th contents increase in magma contaminated by crustal material in shallow levels (Andonaegui et al., 2012; and references therein). The samples show an increase in the Th contents suggesting crustal contamination**.** The low U/Th ratio and the high Th/Ce ratio add further support to the notion of crustal contamination**.**

The syn-orogenic granitic samples have a similar REE pattern to the gneiss (Fig. 3-7b) that is characterized by LREE enrichment (La/Yb_N range from 1.22 to 2.39) and a negative Eu anomaly (Eu/Eu* from 0.61 to 0.13).

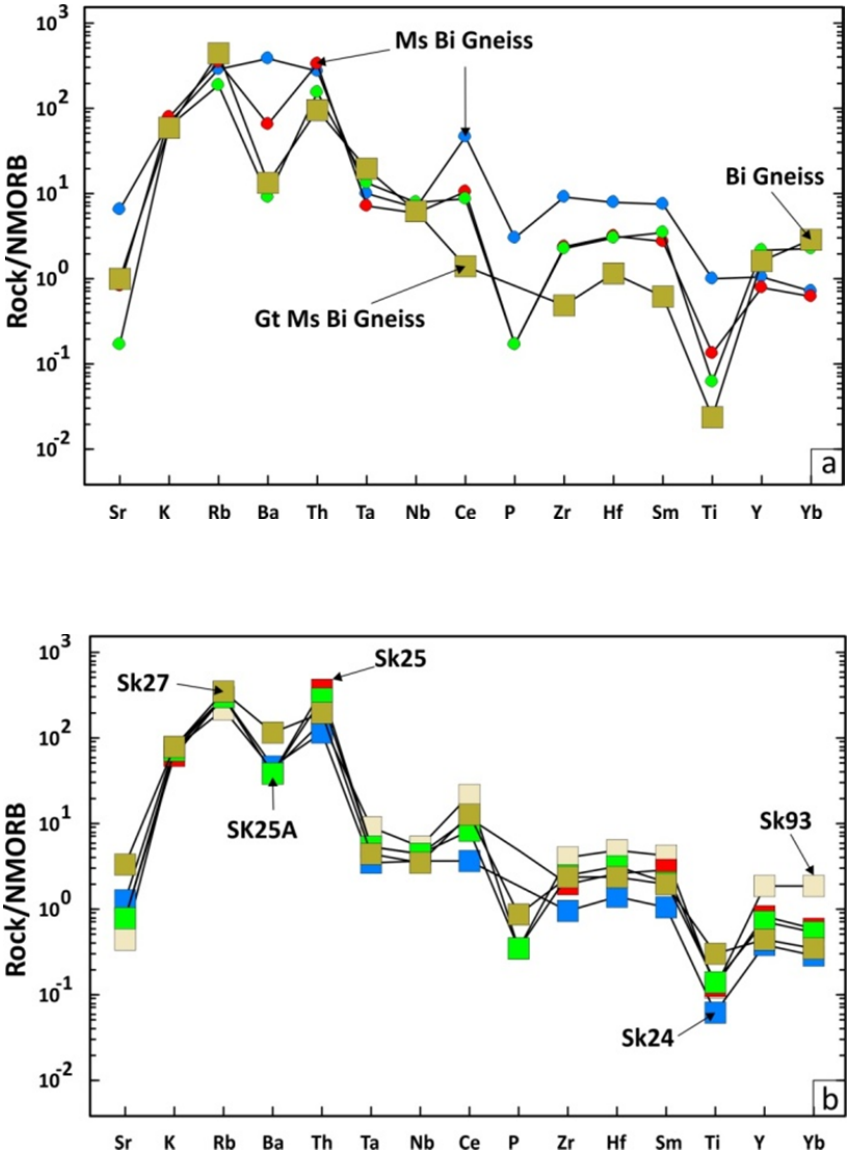

Figure 3-6: NMORB multi-element spidergram of (a) the gneiss samples and (b) the syn-orogenic granitic samples.

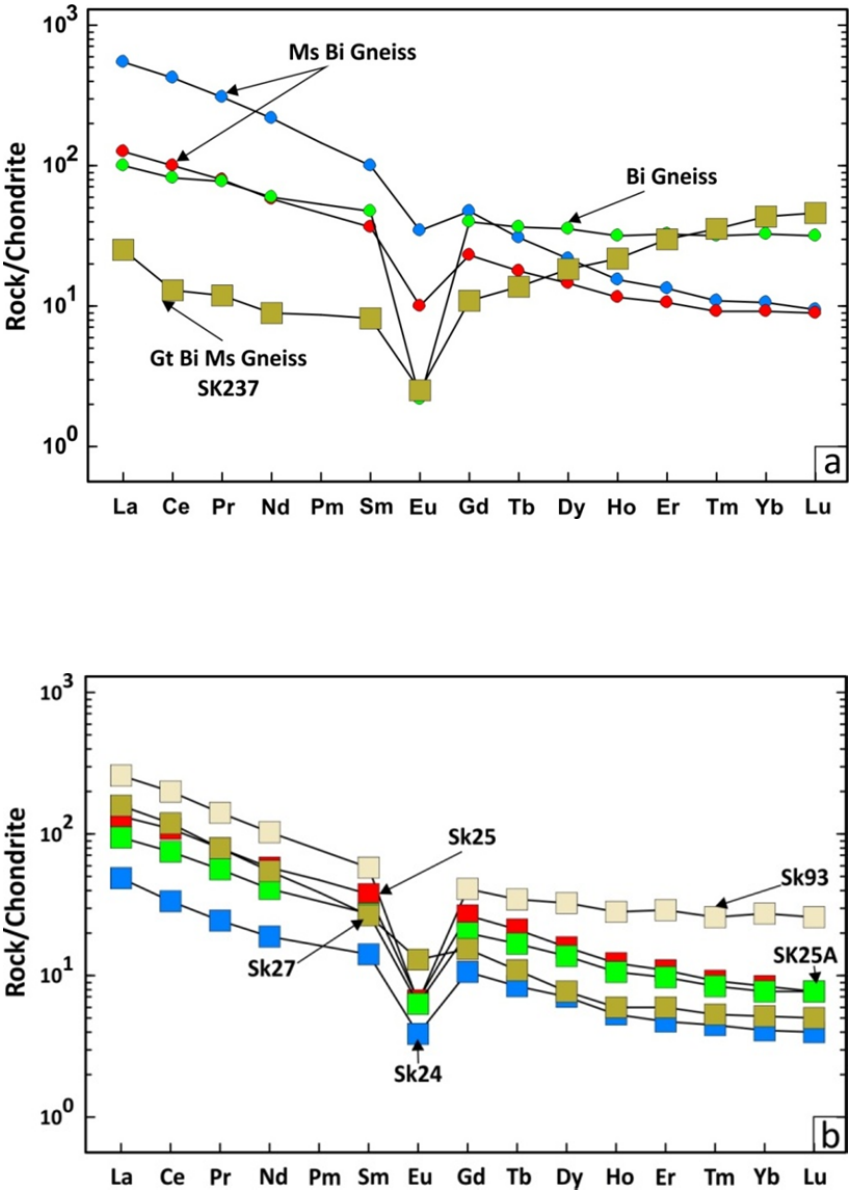

Figure 3-7: Chondrite-normalized diagram for (a) the gneiss samples and (b) the syn-orogenic samples.

3-3-2 Pillow Basalts:

The pillowed basalts show limited variation in SiO_2 from 44.74% to 49.15%, (with one sample showing higher content of 57.86%), TiO_2 from 0.72% to 1.58%, MgO from 4.43% to 7.6%, Fe_2O_3t from 8.39% to 14.38% and K_2O from 0.14% to 1.08% (Appendix 3-2). The Mg# (= {100*Mg (Mg + 0.8FeOt)}) (Luhr, 1997) has low values that range from 36.3 to 41.2. These values are lower than those of primary lavas > 62 (Luhr, 1997; Kampunzu et al., 1998). The bivariate plotting of different elements versus MgO shows a mostly scattered pattern (Fig. 3-8) which is possibly a reflection of open system behavior suffered by most of the major elements during alteration and/or low-grade metamorphism. This interpretation is supported by the breakdown of plagioclases and clinopyroxenes to form secondary epidote, sericite, quartz, actinolite and chlorite, as identified in thin sections.

The lavas have high La/Nb (2.98 – 4.07), La/Sm (1.38 – 2.51), Sm/Nd (0.26 – 0.33) and low Nb/U (1.64 – 7.97), Ce/Pb (1.37 – 8.05) element ratios compared to those of extensional tectonic settings, (e.g., in MORB and WPB including OIB and continental rift basalt emplaced far from any convergent margin {Sun & McDonough, 1989}). These values are similar to those of arc lavas.

The Zr/TiO_2 vs Nb/Y diagram (Fig. 3-9) classifies the samples as sub-alkaline basalt and basaltic andesite. They also plot as island arc tholeiite basalt in the Th vs Co classification diagram (Fig. 3-10).

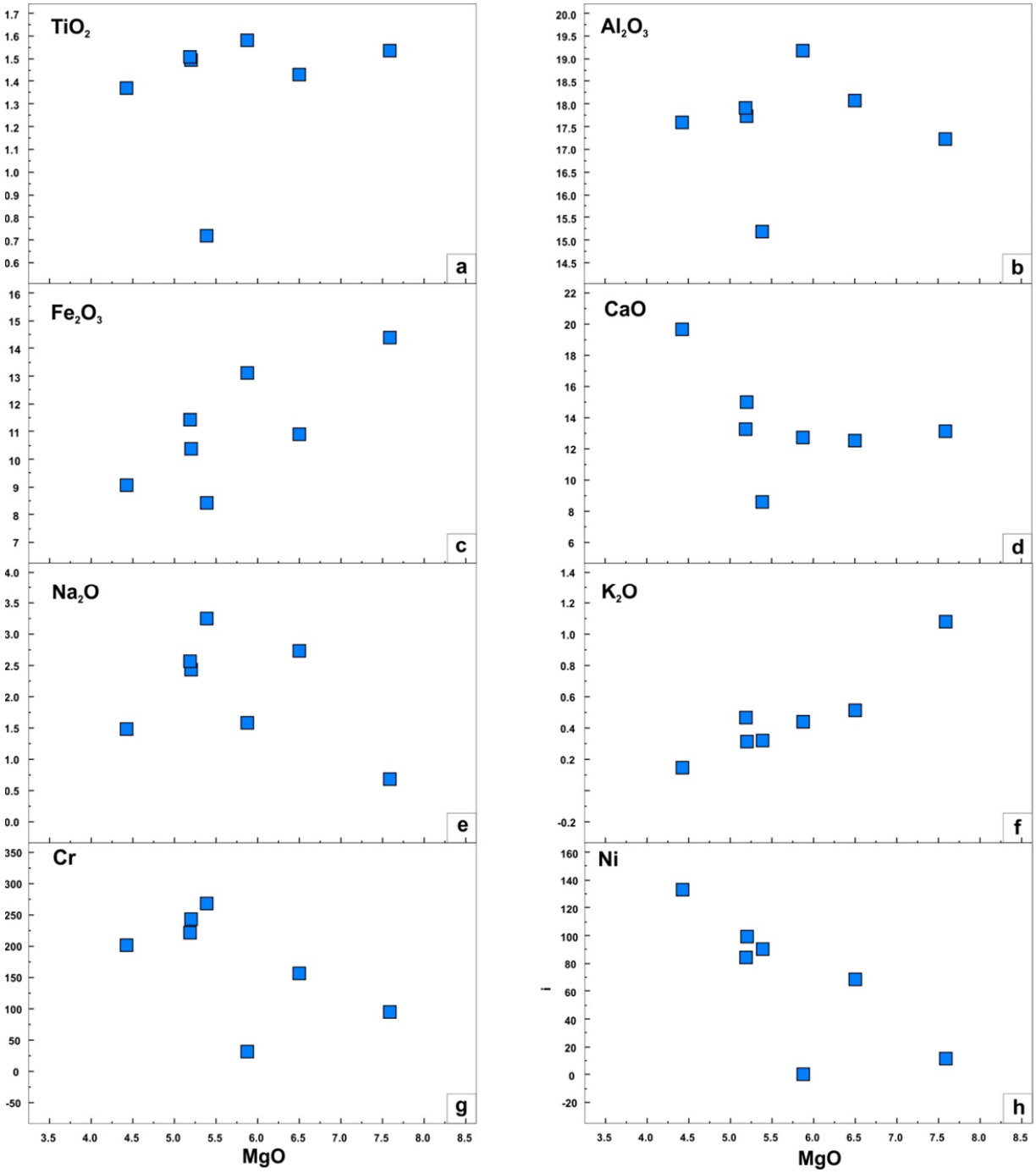

Figure 3-8: Bivariate plots of major and trace elements of the pillow basalt plotted against MgO.

The pillow lavas show a tholeiitic trend on the AFM diagram (Fig. 3-11). This is also supported by their plotting on the island arc tholeiite (IAT) field on the Th/Yb vs Ta/Yb classification diagram using the ratios of relatively immobile trace elements.

The MORB normalised multi-element spiderdiagram of major and trace elements shows features that are typical of subduction–related trace element features (Fig. 3-12) and similar to those of the Vanuatu arc (Peate et al., 1997). These include enrichment of large-iron lithophile elements (LILE) relative to light rare earth elements (LREE) (e.g., Ba/La* ≈ 5.5). Both LILE and LREE are enriched relative to high-field strength elements (HFSE) (e.g., Ba/Nb* ≈ 16.2; La/Nb* ≈ 2.95). The HFSEs, Hf and Zr are depleted relative to the LREEs, Nd and Sm on MORB normalized plots of pillowed basalts. These features are common in arc lava and are attributed to the involvement of a sediment component of the subducting slab (Pearce et al., 1995; Tollstrup and Gill, 2005; Peate et al., 1997) and also to slab dehydration.

The chondrite normalized rare earth element diagram shows a fractionated pattern with high REE abundances (Fig. 3-13). Europium anomalies are absent. The enrichment of the LREE relative to the HREE that is shown by all samples is a characteristic feature of arc lavas as well as back-arc lavas, (Peace & Stern, 2006) and correlates well with the Vanuatu arc (Peate et al., 1997) as shown in Fig. 3-13.

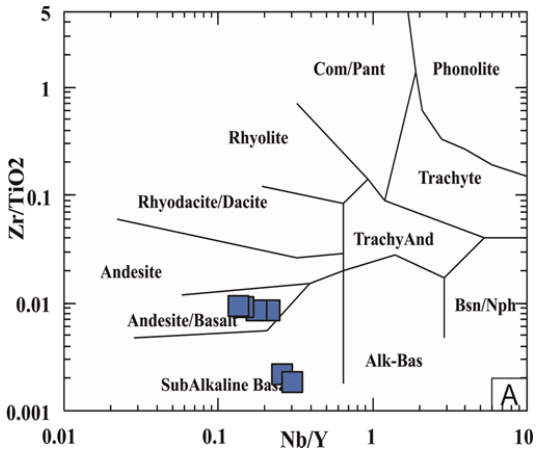

Figure 3-9: The Zr/TiO_2 vs Nb/Y classification diagram (Winchester and Floyd, 1977) which classify the pillow basalt as basalt and basaltic andesite.

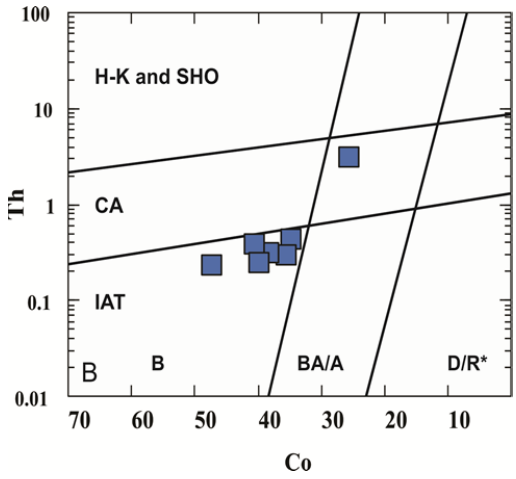

Figure 3-10: Th vs Co classification diagram which classifies the pillow basalt samples as island arc basalts (after Hastie et al., 2007).

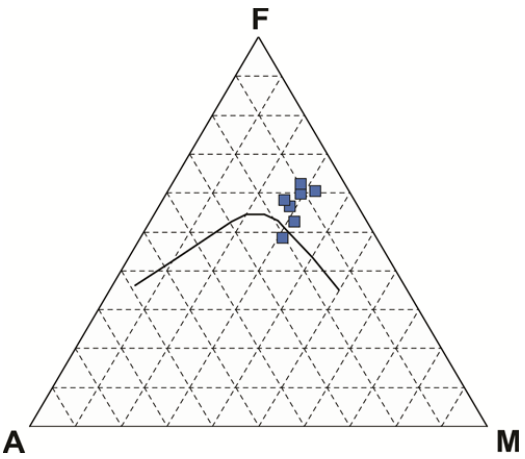

Figure 3-11: AFM diagram showing a tholeiitic trend for Arid samples (Irvine and Baragar, 1971).

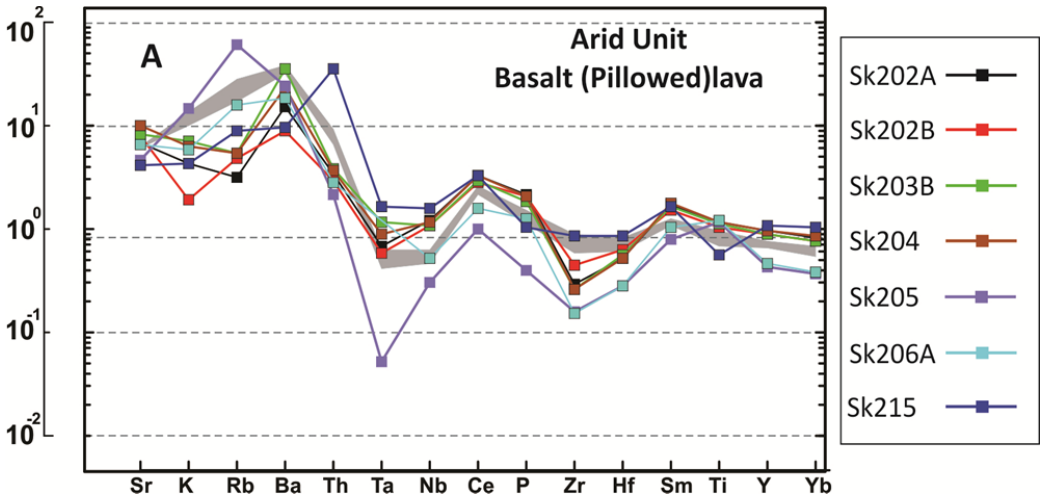

Figure 3-12: N-MORB multi-element spider diagram of major and trace element showing features similar to those of suprasubduction zone ophiolites for the pillow basalts of Arid unit. (REE values are of Sun and McDonough 1989).

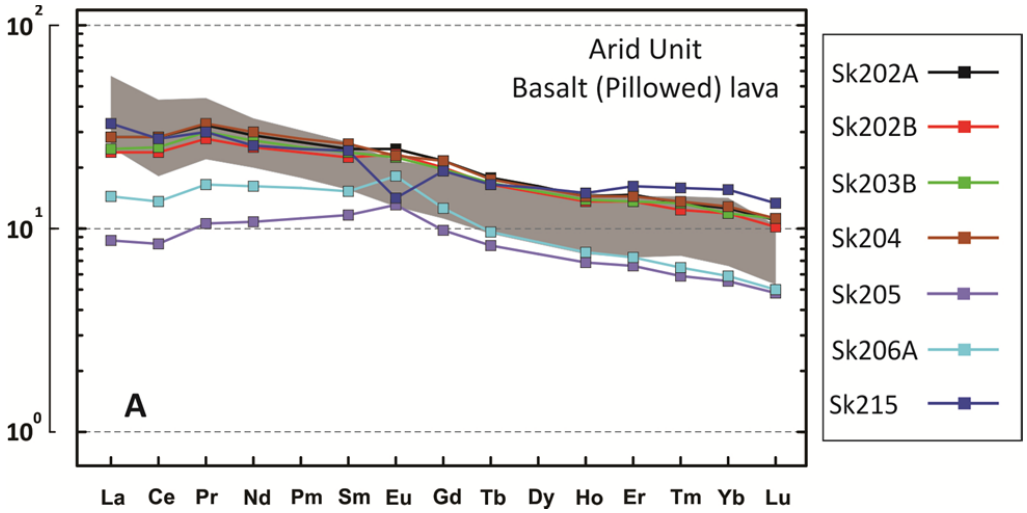

Figure 3-13: Chondrite normalized rare earth element diagram for pillow basalts. The grey shaded area represents samples from Vanuatu arc. (REE values are of Sun and McDonough 1989).

A set of discrimination diagrams using HFSEs and REEs, generally considered to be immobile during alteration and low-grade metamorphism (Campbell et al. 1984; Lesher et al. 1986), have been used in the identification of the metavolcanic samples' tectonic setting and magmatic affinity.

In the Ti-Zr-Y diagram of Pearce and Cann (1973) (Fig. 3-14a), which is effective in discriminating between within-plate basalt (OIB & continental flood basalt (CFB)) and other types of basalt (IAT, MORB & CAB) (Rollinson, 1993), all of the data fall in or at the boundary of non-continental basalt, straddling the fields of IAT (A), the CAB (C) and the field (B) that contains both IAT and CAB together with MORB. This scattering may represent geochemical characteristics that are transitional between those of MORB and IAT, similar to mafic rocks from back-arc basins, where magma generation could involve subduction-related materials (Wilson, 1989; Saunders and Tarney, 1991).

The plotting of the meta-mafic samples on a V vs Ti diagram (Shervais, 1982), which distinguishes between volcanic-arc tholeiite, MORB and alkali basalt (Fig. 3-14b) based on the variation of V partition coefficient as a function of oxygen fugacity, shows a wide dispersion of data (Ti/V <10 and >50). This wide dispersion is a characteristic feature of supra-subduction back-arc ophiolites (Dilek and Furnes, 2011) and is attributed to the wide range of magmas (boninite, Island arc tholeiite and MORB) that occur in subduction influenced igneous regimes. This conclusion is also supported by the plotting of the meta-mafic data on the Zr/Y vs Zr discrimination diagram of Pearce and Norry (1979) where most of the plotted samples fall in the field of back-arc basalt (Fig. 3-14c) described by Floyd et al. (1991) on the same diagram of Pearce and Norry (1979).

The transitional nature (MORB – Arc) for the Arid unit can also be seen from their variable Th/La ratios (0.04 – 0.08 for lava) that are typical of MORB values, generally <0.1 (Plank, 2005) to higher arc values (> 0.2 for massive gabbro). The linear trend of Th/La vs Sm/La (Fig. 3-14d) supports the incorporation of subducted sediments, and sentence not clear where the Arid unit represents the MORB mantle and the Abutulu unit (arc values) indicates the subducted sediments (Plank, 2005).

The multi-element spiderdiagram for the Arid and Abutulu units have a supra-subduction ophiolite geochemical signature indicated by the enrichment of LILE (especially the most incompatible conservative elements Cs, Rb, Th) relative to LREE. Both of them are enriched relative to HFSE. The subduction-related signature is also supported by the slight enrichment in LREE compared to HREE, and by the negative Ta, Nb and positive Pb and Sr anomalies (Dilek and Furnes, 2011). The negative Zr and Hf anomalies suggest the involvement of subducted material from the subducting slab (Pearce et al., 1995; Peate, et al., 1997).

The plotting of Abutulu data on the Ba/Yb vs Nb/Yb diagram (Pearce and Stern, 2006) constrains the shift from the mantle array towards a Mariana arc array (Fig. 3-14e), a feature that distinguishes supra-subduction ophiolites from subduction-unrelated ophiolites, since the latter will usually follow the MORB array (Dilek and Furnes, 2011).

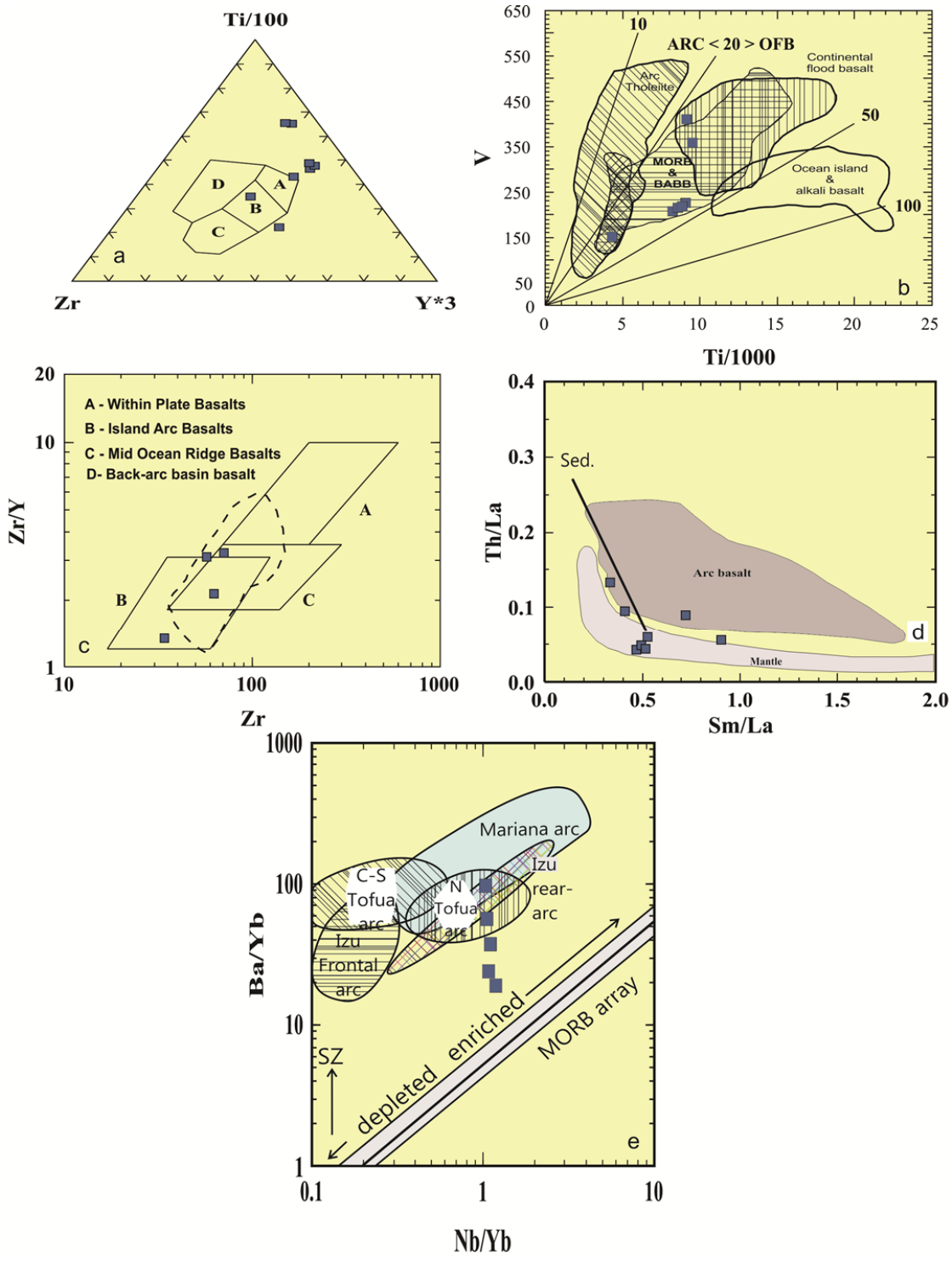

Figure 3-14: Discrimination plots for the Arid basalts (a) Ti-Zr-Y ternary diagram,(b) V vs Ti diagram, (c) Zr/Y vs Zr diagram, (d) Th/La vs Sm/La diagram and (e) Nb/Yb vs Ba/Yb diagram.

3-3-3 Massive gabbros:

The massive gabbro sequence (Appendix 3-2) shows a wide range of SiO_2 from 44.81% to 58.45%, and also a wide range of TiO_2% from 0.25% (lower values usually found in basalts from a convergent tectonic setting) to 2.73% (values characteristic of basalts from extensional tectonic setting), but are mostly < 1%, higher MgO from 4.91% to 10.64% (with one sample showing lower value of 2.14%), and lower Fe_2O_3t from 5.44% to 13.22%. They also have a wide range of Al_2O_3 from 13.94% - 19.58% with only three samples showing higher Al_2O_3 values (Appendix 3-2). The average Al_2O_3 content (17.62%) is close to the average of those reported for IAT and MORB but the anomalous samples fall within the average of high alumina basalt HAB (Brophy and March, 1985).

The Mg# shows higher values (32.7 to 68.56) than those of pillow basalt and a gradational pattern that decreases from massive gabbros to the more basaltic andesite pillowed lava. This pattern suggests increasing differentiation from a primary mantle derived magma with Mg# > 62 to more differentiated magma (cf., Luhr, 1997; Kampunzu et al., 1998).

The massive gabbros show higher concentrations of Cr and Ni (251.4 ppm – 934.76 ppm and 25.7 ppm – 186.22 ppm, respectively, with few samples out of this range) than those of the pillow basalts and have element ratios comparable to those of the pillow basalts and hence of arc lavas (Table 2-3).

The plot of major and trace elements versus MgO (Fig. 3-15) shows rough negative correlation patterns for TiO_2, Al_2O_3, Na_2O and Cr while scattered patterns characterized

Fe_2O_3, CaO and Nb plots. An important feature highlighted by the bivariate plot diagram is the presence of two clusters, one of which includes gabbro samples from the layered sequence of Jebel Arid together with a few samples of scattered gabbroic bodies. However, a different liquid line of descent characterizes the samples of Jebel Arid.

The massive gabbro MORB multi-element spiderdiagram of major and trace elements pattern shows a slight LREE enrichment and HFSE depletion, characteristic of mafic arc magmas (Fig. 3-16), similar to that of Vanuatu arc (Peate et al., 1997).

The moderate to slight LILE enrichments suggest a moderately evolved arc or back-arc environment (Kröner and Liégeois, 2001). The only differences between the Vanuatu arc and the gabbros are the weaker negative Ta and Nb trough in the gabbro and the presence of a negative Zr and Hf anomaly that is shown by sample SK206B. These indicate the involvement of sediment components of the subducted slab, mantle-liquid interaction reaction or slab dehydration (Pearce et al., 1995; Tollstrup and Gill, 2005; Peate et al., 1997), a feature commonly seen in arc lavas. Three of the massive gabbros samples (SK201, SK207 and SK240B) show relatively flat LREE and strongly fractionated HREE, $(Gd/Yb)_N$ between 3.45 to 3.6 possibly suggesting their generation through 3-5% melting of an Fe-rich mantle corresponding to the stability fields of spinel and garnet peridotite at depths of 60-100 km (Manikyamba et al., 2015).

The chondrite-normalized rare earth elements pattern for the massive gabbro (Fig. 3-17) show LREE enrichment, $(La/Yb)_N$ (average = 2.41) and HFSE depletion characteristic of mafic arc magmas. The slight to moderate LILE enrichment indicates a primitive arc or back-arc environment (Pearce and Stern, 2006).

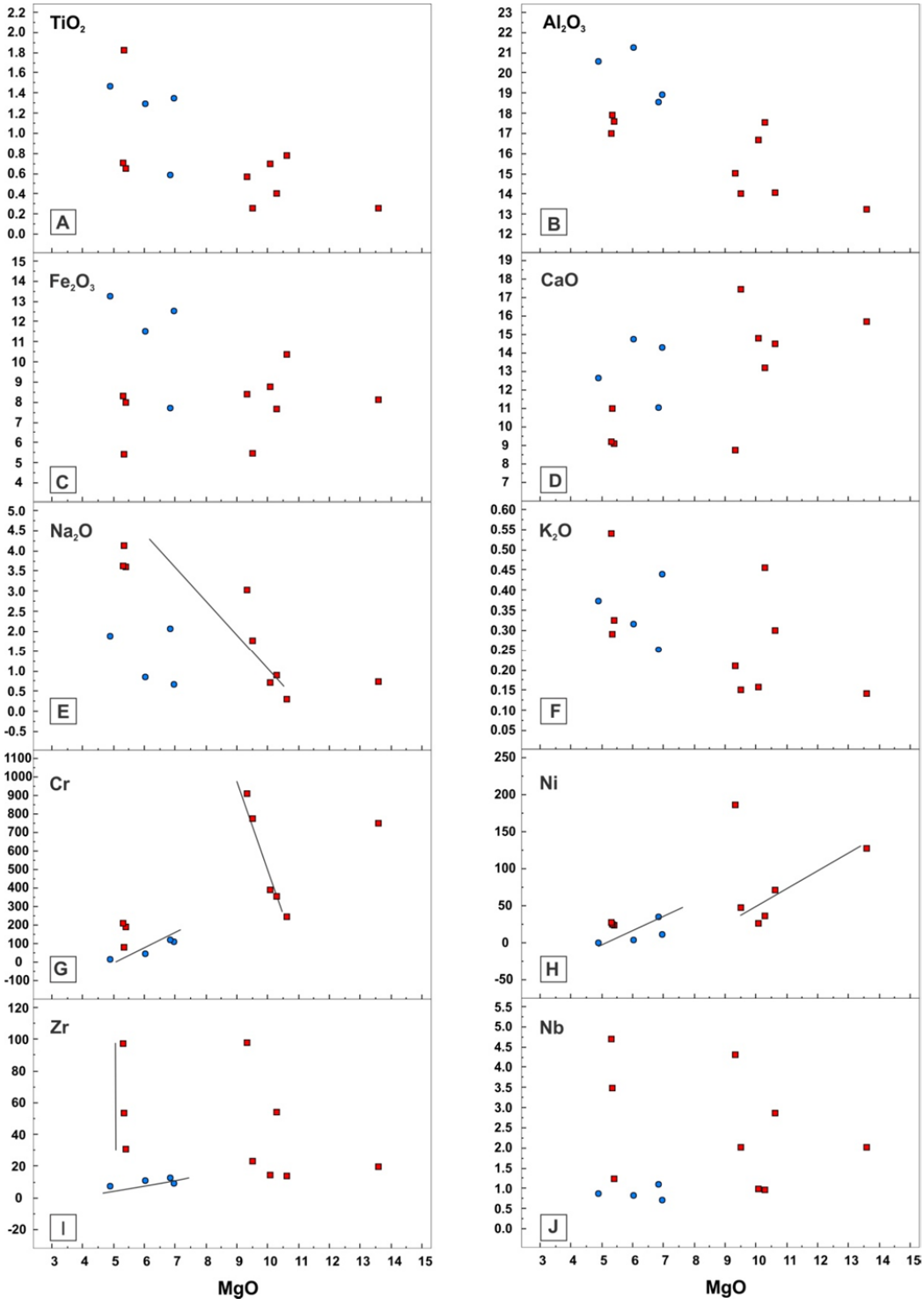

Figure 3-15: (A) to (J) bivariate plotting of some major and trace elements versus MgO of gabbroic composition.

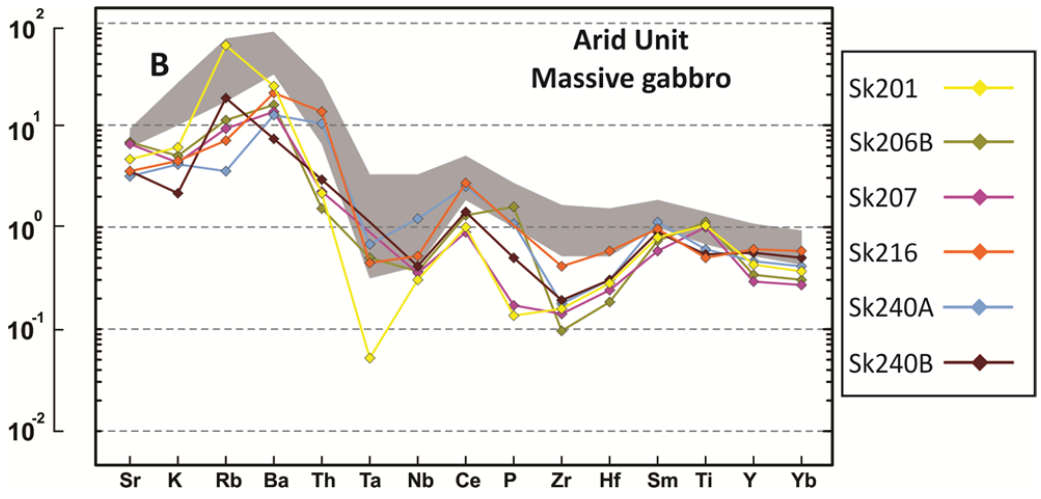

Figure 3-16: MORB multi-element spider diagram of major and trace elements for the massive gabbro of Arid unit.

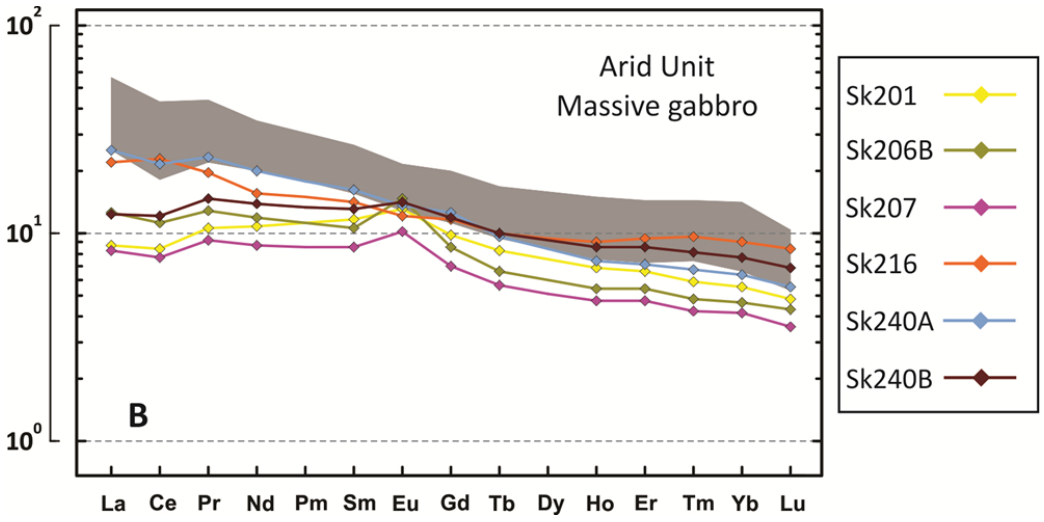

Figure 3-17: Chondrite-normalized rare earth element diagram for the massive gabbro of the Arid unit. The grey shaded areas represent the plots of samples from Vanuatu arc.

A significant positive Eu anomaly (Eu/Eu* ≈ 1.2) dominates the massive gabbro (with exception of samples SK216, SK 240A and SK240B) (Fig. 3-17) and indicates the role of accumulation of plagioclase in the genesis of the lower section of Abutulu unit (Rollinson, 1993; Preccerillo and Taylor, 1976). The three above mentioned samples that show no Eu anomaly also have higher REE abundances (∑REE = 49.2 ppm).

To conclude with, these gabbros can be interpreted to represent a lower section of subduction related arc or back-arc magmas.

3-3-4 Basaltic andesites and andesite meta-volcanics:

The Zr/TiO_2 versus Nb/Y classification diagram (Fig. 3-18) demonstrates the classification of the meta-volcanic rocks as basaltic andesite and andesite with most of the samples falling in the latter category.

The meta-volcanics are characterized by moderate silica (42.8% – 64.87%) and relatively high TiO_2 (up to 2.40%), Al_2O_3 (11.96% - 17.59%), Fe_2O_3t (5.12% - 15.71%) and MgO (2.13% - 9.75%). Transitional metals (Cr & Ni) reach an average of 135.49 ppm and 22.36 ppm, respectively (Appendix 3-3).

On a MORB-normalized multi-element incompatible element plot (Fig. 3-19), the meta-andesite show LILE-enriched, HFSE depleted patterns, characteristic of arc derived magma, a well developed negative Nb-Ta trough (with variable degree of depletion) and a negative Zr-Hf trough shown by sample SK51.

All of these geochemical signatures are features of subduction-related magmas. The meta-andesite shows a better correlation with the Vanuatu arc than the massive gabbro

and the pillowed basalt. The main difference between the meta-andesite is the enrichment of Th relative to MORB which may indicate an increasing sedimentary component from the subducting slab (Plank, 2005) or an increase in the thickness of the arc crust which allows Th enrichment (Küster and Liėgeois, 2001 and references therein).

A chondrite-normalised REE diagram of the Abutulu meta-volcanic (meta-andesite) rocks (Fig. 3-20) shows a fractionated pattern similar to those of the Arid unit (lava and gabbro), however the REE abundances are higher than those of the basalts and the gabbros ∑REE ≈ 150 ppm. A negative Eu anomaly (Eu/Eu* ≈ 0.67) is a pronounced feature in the REE pattern of all Abutulu meta-volcanic data. The meta-volcanic rocks are enriched in LREE and show good correlation in the REE pattern with Vanuatu arc (Peate et al., 1997).

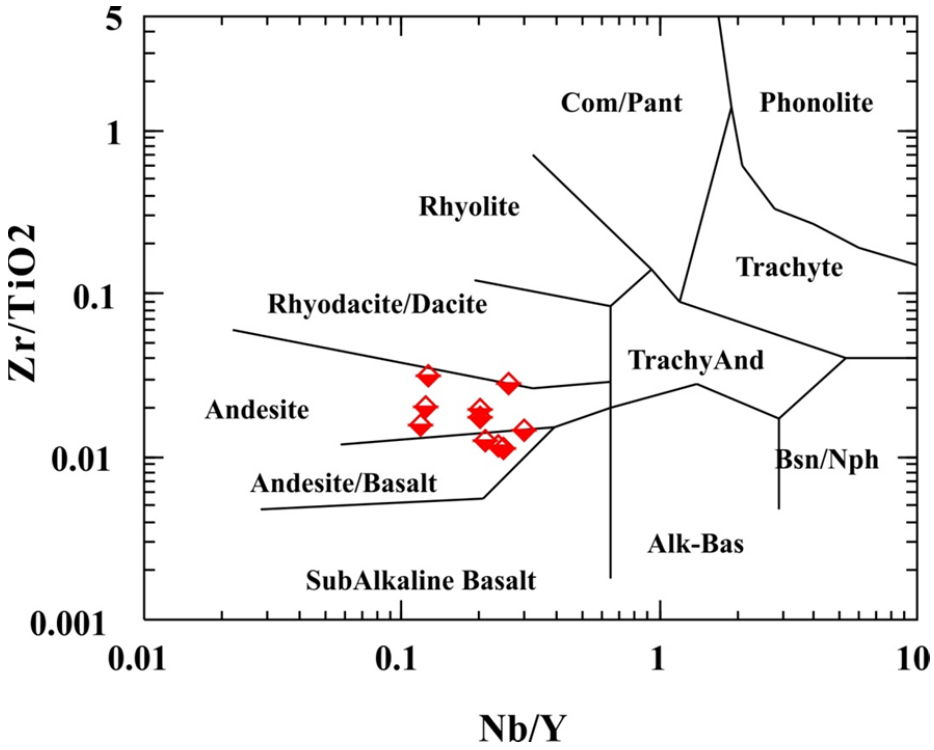

Figure 3-18: The Zr/TiO_2 vs Nb/Y classification diagram (Winchester and Floyd, 1977) which classify the Abutulu rocks as basalt and basaltic andesite.

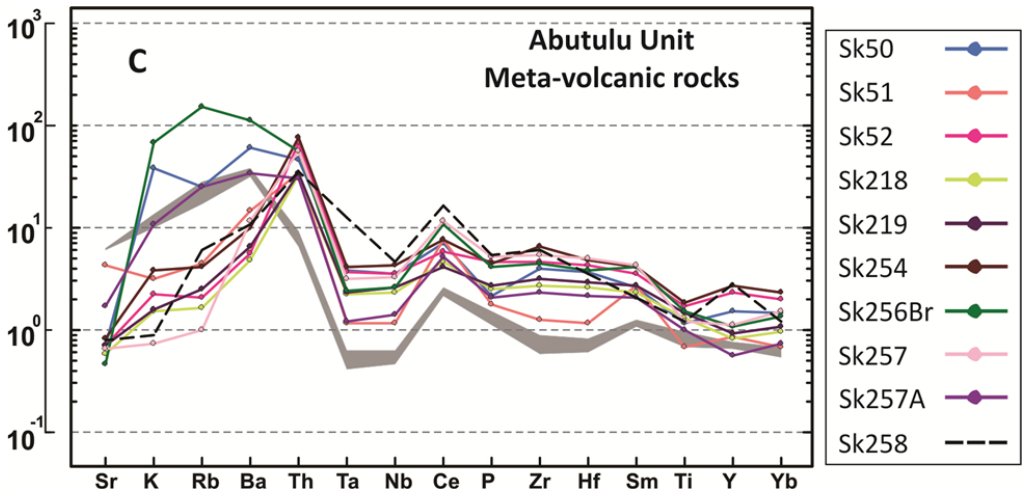

Figure 3-19: MORB multi-element spider diagram of major and trace element for the meta-andesite of Abutulu unit. The grey shaded areas represent samples from Vanuatu arc.

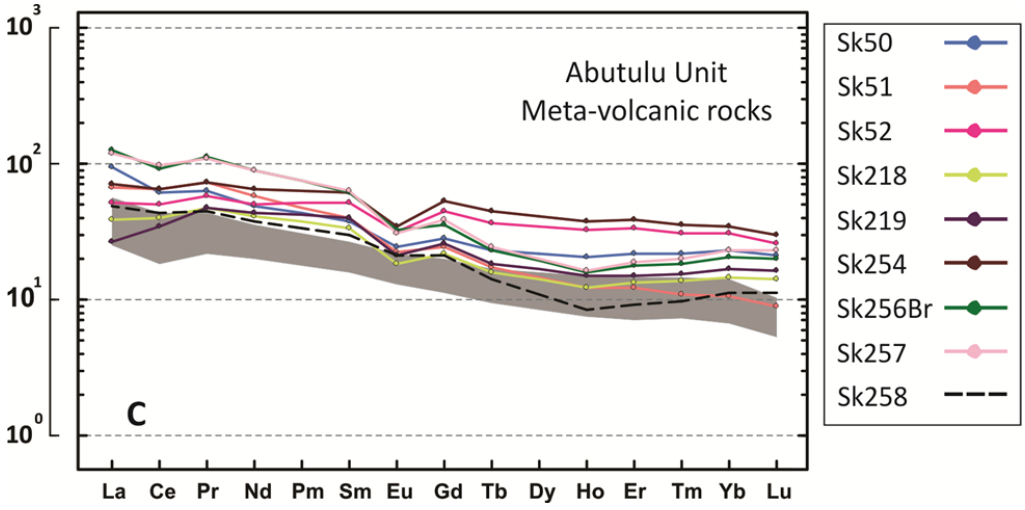

Figure 3-20: Chondrite normalized rare earth element diagram for the meta-andesite of the Abutulu unit. The grey shaded areas represent samples from Vanuatu arc.

3-3-5 Late-orogenic granitoids:

The plotting of the late-orogenic samples in the Ab-An-Or (Fig. 3-21) (O'Connor, 1965) and the Q' (F')-ANOR (Fig. 3-22) (Streckeisen and LeMaitre, 1979), classification diagrams, reveal that all of the four samples plotted in the field of granite in the first and they split in the latter between the fields of granite and syeno-granite.

These granitic and the syeno-granitic samples have a shoshonite composition (Fig. 3-23). The term shoshonite is used in this context to describe rocks with a very high-K content, although the term was originally defined for volcanic rocks. They are slightly to moderately peraluminious, with aluminum saturation index (ASI), (also known as A/CNK ratio = molar $Al_2O_3/CaO+Na_2O+K_2O$), ranges from 1.01 to 1.14. The SiO_2 content in these rocks is restricted only from 70.24% to 74.11% (Appendix 3-1). Tight ranges also characterize the contents of Al_2O3 (14.30% - 15.62%), Na_2O (3.12% - 4.10%) and K_2O (5.24% - 5.97%). Negative correlation against SiO_2 is noticed in the following major oxide and trace elements; TiO_2, Al_2O_3, Fe_2O_3, MgO, P_2O_5, Ba and Zr. This feature is less obvious in K_2O, Rb and Nb (Fig. 3-24). The range of trace element (Zr, Nb, Ce, Y, and Zn) is well within the limit of I, S and M-types of Whalen et al., (1987).

Utilizing the Nb versus Y discrimination diagram of Pearce et al., (1984) all samples plot within the VAG (volcanic arc granite) with one sample on the boundary with the syn-COLG (syn-collisional granite) field. All of the late-orogenic granites occupied the VAG and the syn-COLG field (Fig. 3-25). When the samples are plotted in the Yb versus Ta classifications diagram (Pearce et al., 1984), (which separate the VAG and the syn-

COLG field of the previous diagram into individual fields), all of the samples fall in the VAG field (Fig. 3-26).

On the chondrite normalized rare earth element diagram (Fig. 3-27) all of the granite and syeno-granite samples have moderate ΣREE values between 106 ppm to 238 ppm, a fractionated REE pattern ($(La/Yb)_N$ between 17.1 and 77.1) and a slightly negative Eu anomaly (0.71 to 0.89).

On the normal mid-oceanic ridge basalt (N-MORB) normalized multi-element spidergram (Fig. 3-28), all of the late-orogenic granites show a pronounced Ta and Nb negative anomaly, depletion in Sr, P_2O_5 (shown by SK 224), Y and Ta. All of the samples show enrichment in K_2O and Rb. The late-orogenic granite REE pattern and MORB normalized spidergram show a close resemblance to the Nabati pluton of the Bayuda desert of northern Sudan, which is akin to the subduction-related continental margin rhyolites and rhyodacites (Kùster et al., 2008).

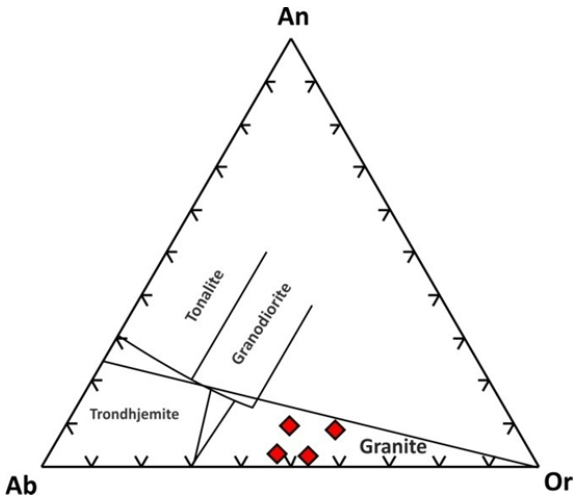

Figure 3-21: Ab-An-Or Norm classification diagram (Barker, 1975) which classify the late-orogenic granitoids as granite.

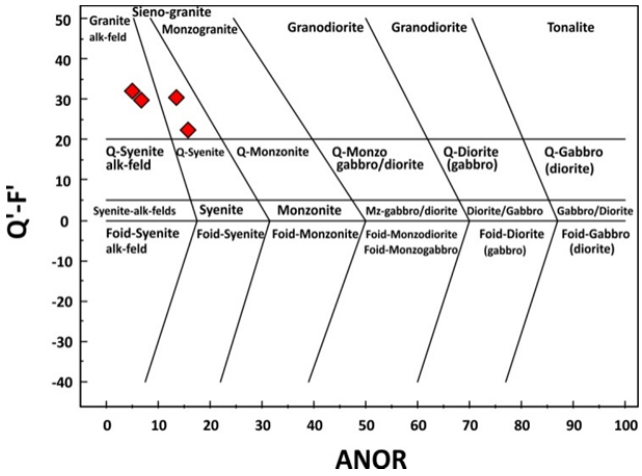

Figure 3-22: The Q-F vs ANOR classification diagram for the late-orogenic granite rocks (Streckeisen and Le Maitre, 1979). Q = Q/(Q+Or+Ab+An); F = (Ne+Lc+Kp)/(Ne+Lc+Kp+Or+Ab+An); ANOR = 100 x An/(Or+An).

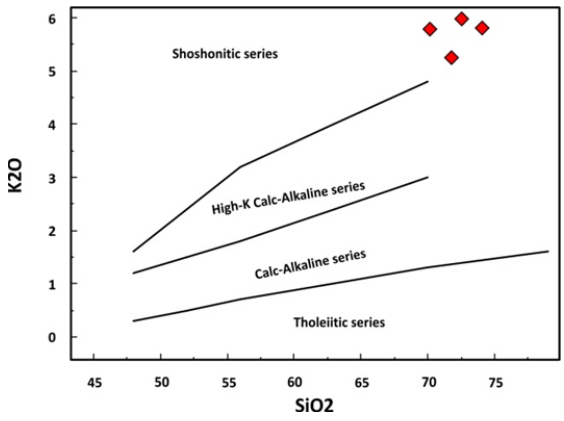

Figure 3-23: K_2O vs SiO_2 classification diagram that classify the late-orogenic granite as shoshonitic.

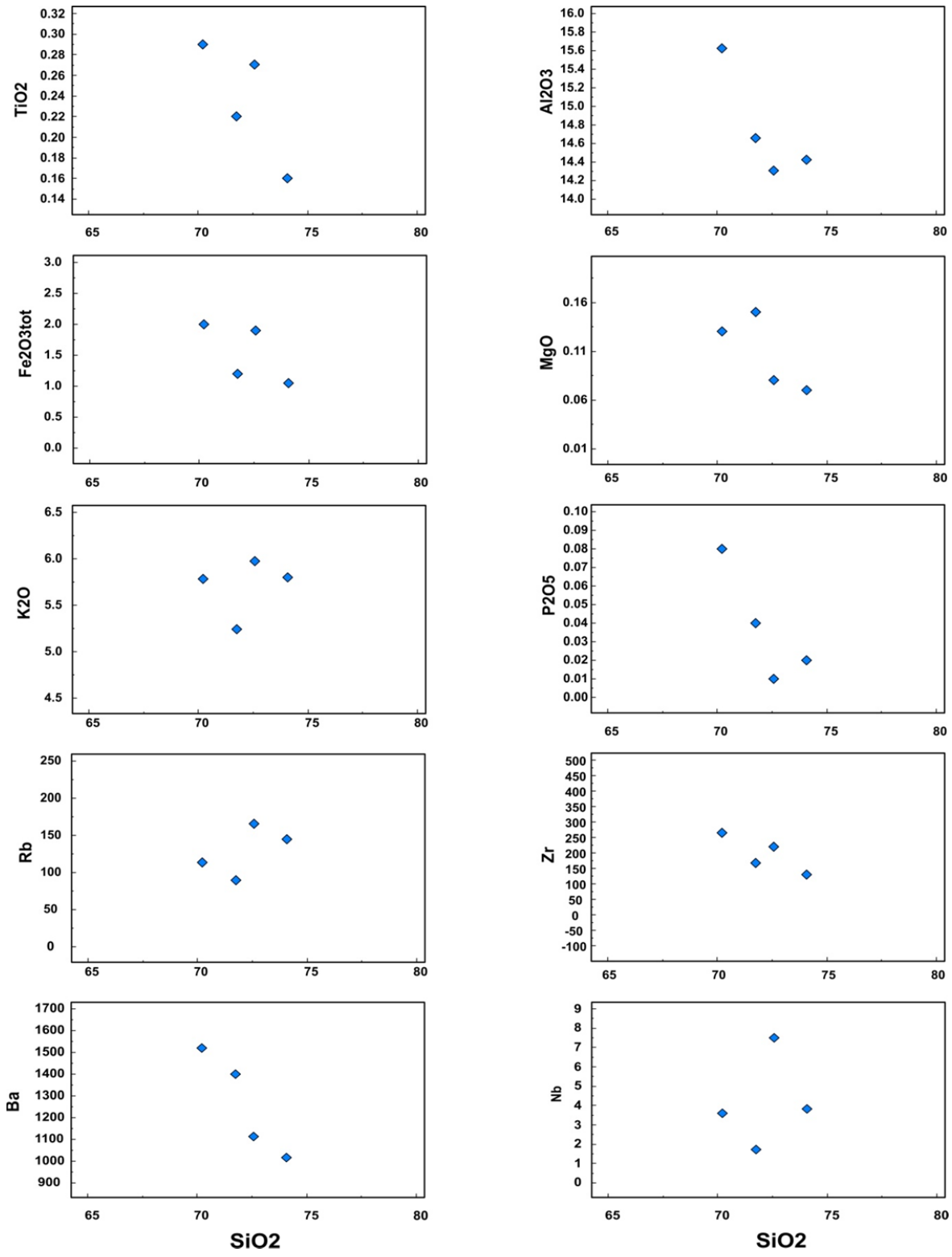

Figure 3-24: Bivariate plotting of various elements versus silica for the late-orogenic granite.

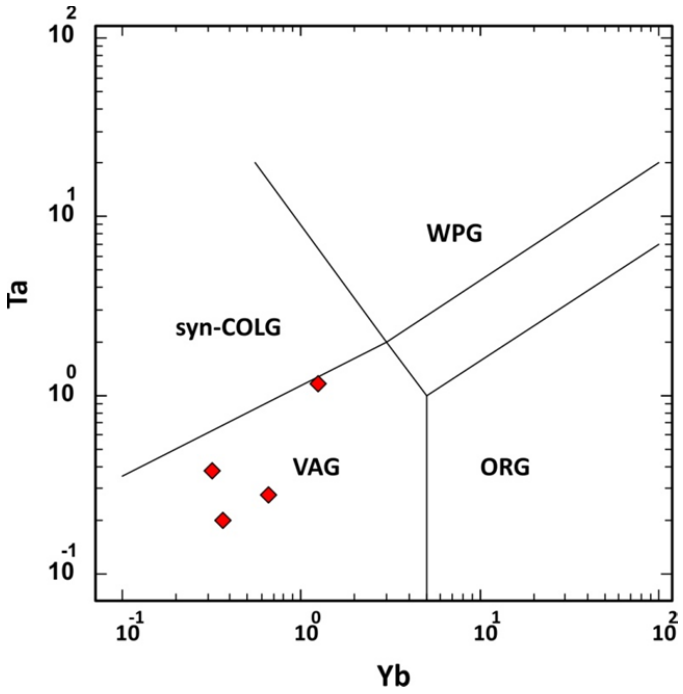

Figure 3-25: The Ta versus Yb discrimination diagram of Pearce et al., (1984), which classify the granitic rocks as volcanic arc granite (VAG), syn-COLG = syn-collisional granite; ORG = oceanic ridge granite.

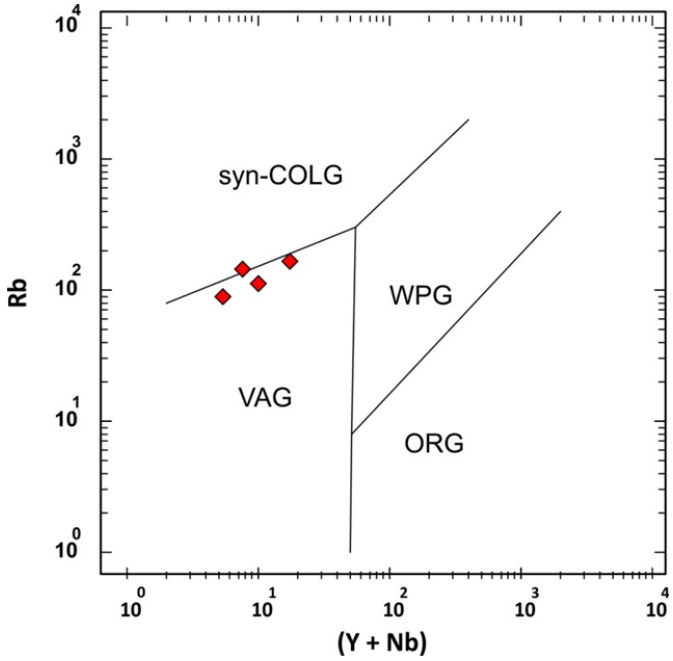

Figure 3-26: The Rb versus (Y+Nb) discrimination diagram of Pearce et al., (1984), which also identify the late-orogenic granite as volcanic arc granite (VAG), syn-COLG = syn-collisional granite; ORG = oceanic ridge granite.

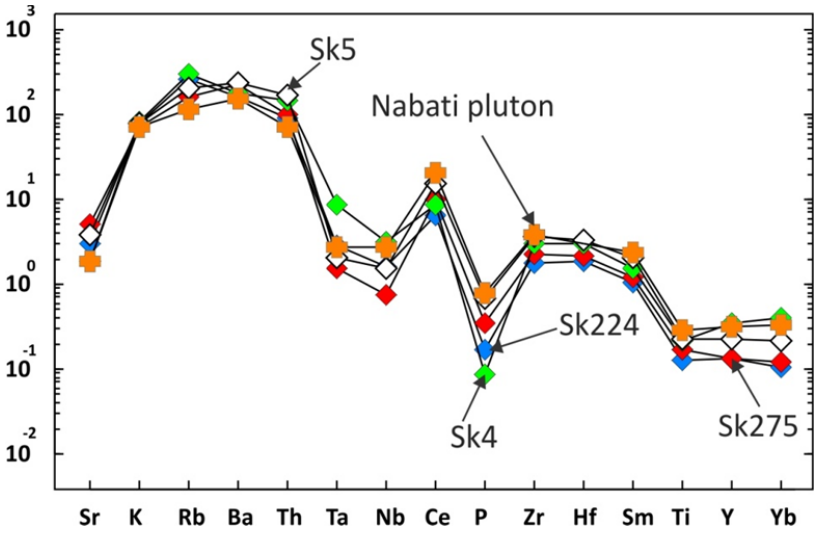

Figure 3-27: NMORB-normalized multi-element spider gram (normalization values are of Sun and McDonough, 1985) for late-orogenic granite. The orange cross represent sample from Nabati outcrop of the Bayuda desert of northern Sudan.

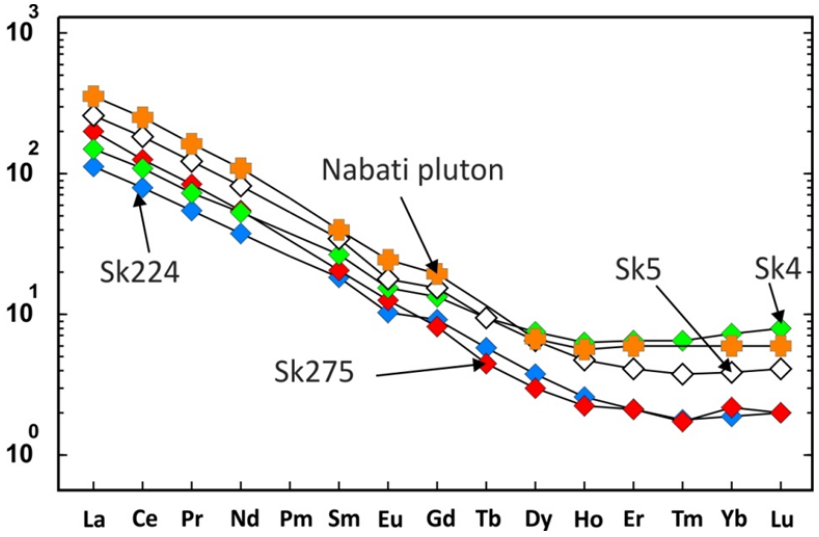

Figure 3-28: Chondrite-normalized REE plot (normalization values are of Boynton, (1984) for the late-orogenic granite.

4- Structural Evolution of the Western Nuba Mountains:

4-1 Introduction:

This chapter deals with the structural evolution of the Abutulu shear zone. The work is based on structural observations and evidence acquired from four main localities (Fig. 4-1) and from supplementary geotraverses within the study area.

This chapter will also provide data to better understand the structural evolution of belts of the low-grade metavolcano-sedimentary sequence commonly associated with the ophiolites that are evident within the SMC.

These low-grade associations are generally explained by two tectonic models, both resulting from the opening and closing of restricted oceanic basin or an oceanic re-entrant.

1- Some associations are developed as fold and thrust belts without the development of subduction zones and an arc edifice eg. the Rahib fold and thrust belt (Abdel Rahman et al., 1990).
2- Others are associated with early S-verging ophiolite nappes and thrusts due to closure and terrane collision along an E-trending suture, followed by E-W shortening as a result of the collision between east and west Gondwana eg. the Atmur – Delgo Suture (Schandelmeier et al., 1994; Abdelsalam et al., 1995).

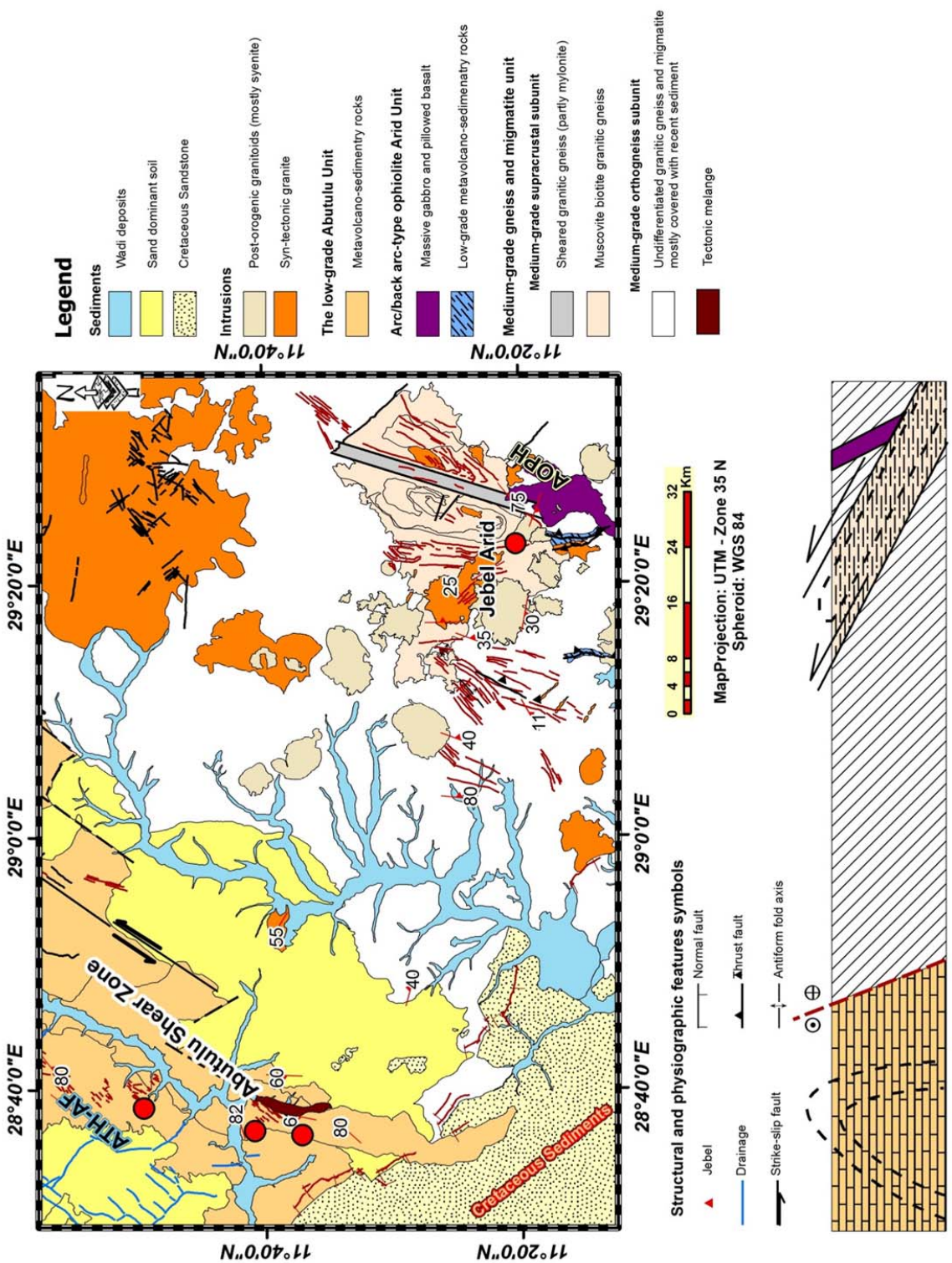

Figure 4-1: Structural map of the western Nuba Mountains. ATH-AF = Althwani antiform fold. AOPH = Arid ophiolite. Red cycles= location of data.

4-2 Geology of the Abutulu Shear zone:

The general geology of the Abutulu shear zone is discussed in chapter two. The Abutulu shear cuts three lithological units that are from west to east; the Al Thawani-Tugula metasedimentary and metavolcanic rocks, the Abutulu-Arid metavolcanic rocks and the western peripheries of medium-grade gneisses. The Al Thawani-Tugula metasedimentary rocks are composed of a fining upwards repetitive cycle of pebbly congolomerate, coarse-grained sandstone and medium-grained sandstone (turbidites) and basic to intermediate volcanics (now chlorite schist) that are interpreted to represent passive margin sediments and volcanic rocks. The Abutulu metavolcano-sedimentary unit is mainly meta-andesite, meta-acidic volcanic rocks of arc affinity and mica and mica quartz schists. The medium-grade gneisses are mainly I-type orthogneisses with minor S-type varieties that show a high-K calc-alkaline and arc affinity.

4-3 Deformation history of the gneisses of the Nuba Mountains:

Three phases of deformation were recognized in the basement rocks of the Nuba Mountains (El Ageed and El Rabaa, 1981; Abdelsalam and Dawoud, 1991). These authors identified two early phases of folding and a third phase of brittle faulting with the second phase of deformation being the major phase, characterized by a doubly plunging antiform, and east-verging thrusts (El Ageed and El Rabaa, 1981) with tight, slightly overturned east- verging folds (Abdelsalam and Dawoud, 1991).

4-3-1 D_1 Deformation:

Within the basement of the western most Nuba Mountains, the earliest recognizable phase of deformation (D_1) is characterized by the development of a mappable scale doubly plunging antiform (F_1) (Fig. 4-1) and the development of a strong S_1 foliation plane which is considered to be related to F_1 folds. The axial plane of the major F_1 folds northeast of Jebel Arid has an almost N-S trend. S_1 is parallel to the bedding plane (S_0) along the limbs of F_1 and cuts S_0 at higher angle at the hinges (i.e. S_1 is axial planar cleavage to F_1 folds). In the gneisses, elongated quartz and feldspar crystals together with oriented biotite and minor muscovite define the foliation.

4-3-2 D_2 Deformation:

This deformation event is characterized by the development of isoclinal to tight recumbent folds (F_2) (Plate. 4-1) and is associated with shallow-dipping northwest-verging thrust planes. The planar fabric associated with D_2 deformation is mainly a shallow dipping migmatitic foliation (S_2) that is defined by compositional layering and preferred orientation of platy minerals (mainly biotite) in the metasedimentary rocks. In most of the gneisses and the migmatite foliation S_2 is the only fabric present. The lineation associated with D_2 deformation is a shallow southeast plunging L_2 stretching lineation (Fig. 4-2). The D_2 folding is characterized by folding of granitic leucosome portion of migmatites and compositional metamorphic layering rather than folding of foliation of different generations seen in later deformational events. This kind of parallelism and folding of granitic melt and leucosome portion of migmatites might suggest a high-temperature metamorphic environment during D_2.

Plate 4-1: A photograph showing the recumbent isoclinal folds F_2.

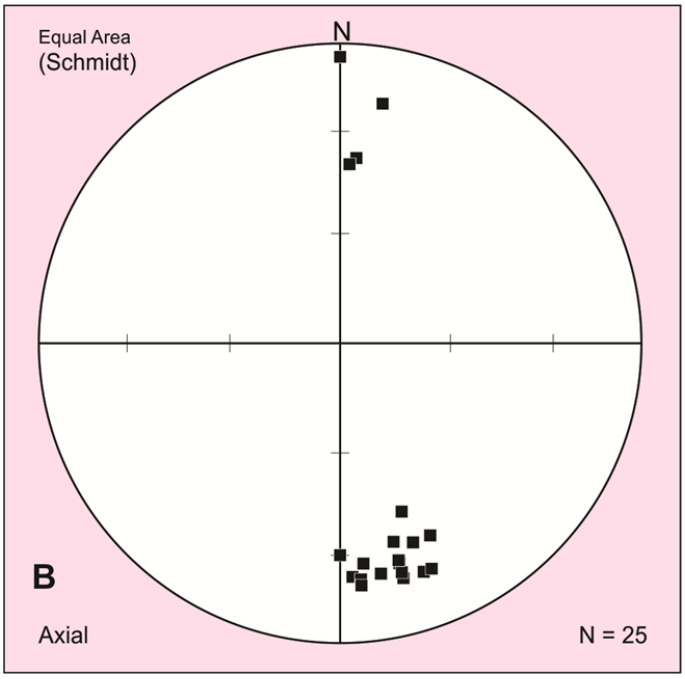

Figure 4-2: Plot of L_2 stretching lineation.

Folds in D_2 are generally small scale isoclinal folds, with wavelength that range from 30 centimeters to a few meters and the two limbs are usually parallel to sub-parallel. The thickness of the folded layer reflects similar fold geometry.

4-4 The Abutulu Deformation:

4-4-1 D_3 Deformation Sinistral translation dominant phase:

This deformation is characterized by the development of a steeply-dipping north to northeast-trending sinistral strike-slip shear zone together with steeply-plunging tight to open folds (F_3) (Fig. 4-3) associated with a moderately spaced S_3 foliation plane (Plate 4-2). D_3 is considered to represent the earliest phase of deformation in the relatively young metavolcano-sedimentary sequence since it folds the S_0 bedding plane along the axis of F_3 folds. D_3 is also responsible for development of a tectonic mélange along the boundary between the medium-grade gneiss and the low-grade metavolcano-sedimentary unit, where a narrow zone of lenses of hornblendite, gabbro and basalts of variable size, (up to 20 meter in width) are imbedded into a highly sheared, matrix of psammopelitic schist (Fig. 4-1).

The S_3 Planar fabric associated with D_3 is a magmatic foliation, which is marked by the parallel alignment of euhedral crystals of feldspar that show minor internal deformation. Both right-hand and left-hand rotation of crystals has been observed within the outcrop scale suggesting a component of pure shear. The magmatic-stage foliation, when moving towards the centre of the shear zone, gradually grades into a shear-related mylonitic fabric, the tabular feldspar crystals tend to be flattened into lensoidal shapes (augen) surrounded by a well-developed foliation of generally mica-rich matrix.

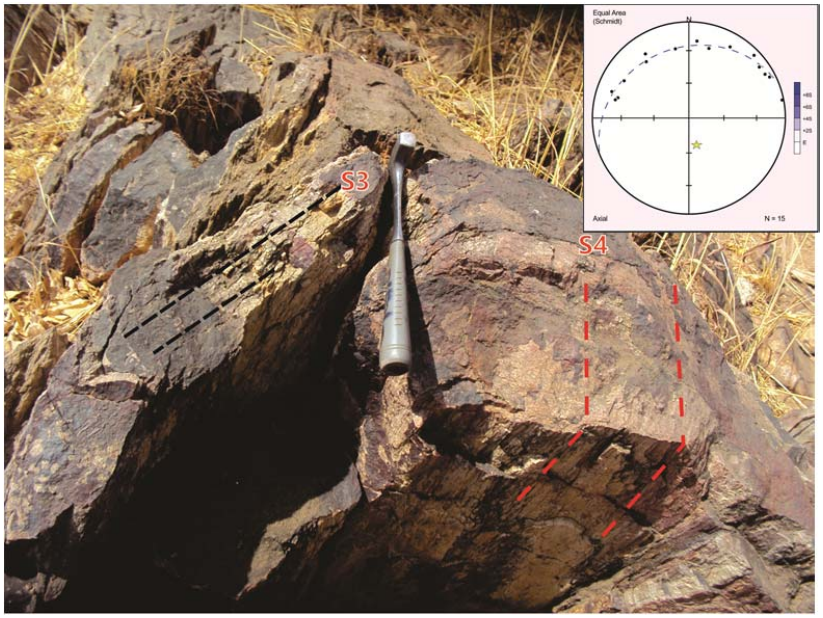

Figure 4-3: A photograph showing the steep plunging nature of F_3 folds and the development of a S_3 axial planar cleavage. At the corner of the figure is the S-pole diagram with the β axis.

Plate 4-2: A photograph showing the dominant S_3 foliation planes in Al Beida outcrop.

Ultramylonite occasionally associated with pseudotachylite veins is developed in parts of the meta-sediments of the central part of the shear zone.

The S_3 foliation dips steeply east (60˚ – 80˚) and locally shows a well-developed stretching lineation L_3 that either plunges steeply east (down dip) or is oblique and plunges moderately steeply to the northeast (Fig. 4-4). The rare existence of L_{2-3} intersection lineations between an early (much localized) S_2 cleavage with dominant S_3 mylonitic foliation can be found (Plate 4-3a & 4-3b). The L_{2-3} intersectional lineation plunges moderately to the northeast. The D_2 planar fabric is a generally an even-spaced cleavage, bounded by S_3 foliation planes. The regularity of S_2 makes it difficult for it to be considered as bedding planes but rather suggests it belongs to an earlier D_2 deformation event.

Locally, S_3 planes are developed into steeply, south plunging isoclinal F_3 folds (Fig. 4-5a and 4-5b) suggesting that the sinistral displacement accompanied S_3 foliation development. This is also indicated by localized development of foliation fish, rotated porphyroblasts and a possible S-C foliation.

Mesoscopic folds related to D_3 are reported at two localities; the Al Beida outcrop and the Tugula outcrop (Figs. 4-6 and 4-7). They have variable geometry including similar, concentric and chevron folds with variable inter-limb angles including, isoclinal, tight and gentle folds. Wider hinge zones (concentric folds) and less steep plunging fold axes are characteristics of the Al Beida outcrop (Plate 4-4a), while narrow hinge points (chevron folds) and steeper plunging axes (vertical in some folds) are characteristic of the Tugula outcrop (Plate 4-4b & 4-4c).

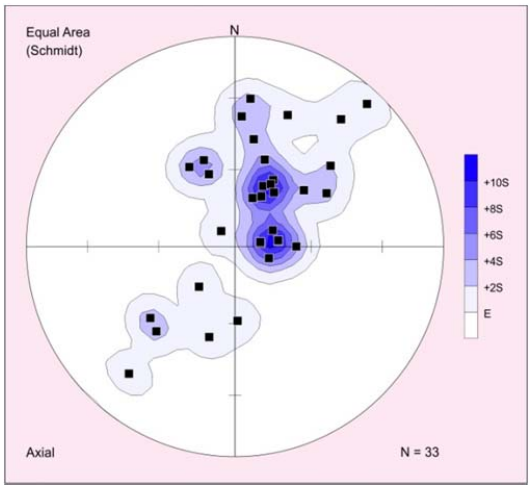

Figure 4-4: Steeply easterly to NE plunging L_3 stretching lineation at Al Beida outcrop.

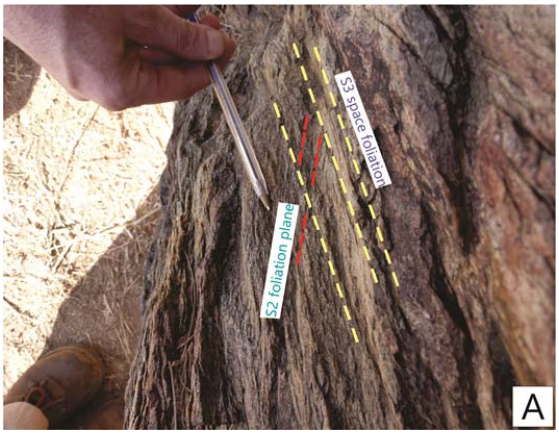

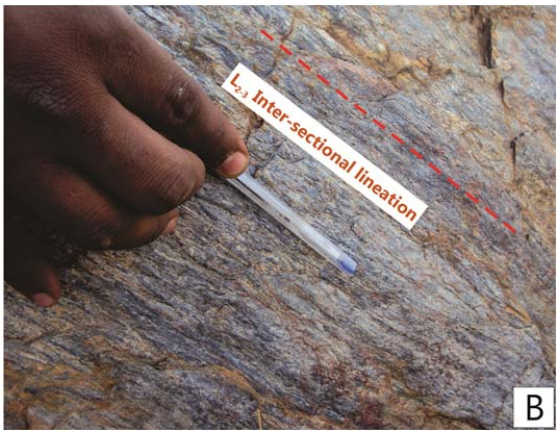

Plate 4-3: (a) The dominant Planar fabric in the Abtulu unit S_3 constraining an early much localized S_2 fabric in the northern part of Al Beida outcrop. (b) The moderately northeast plunging $L_{2\text{-}3}$ inter-sectional lineation.

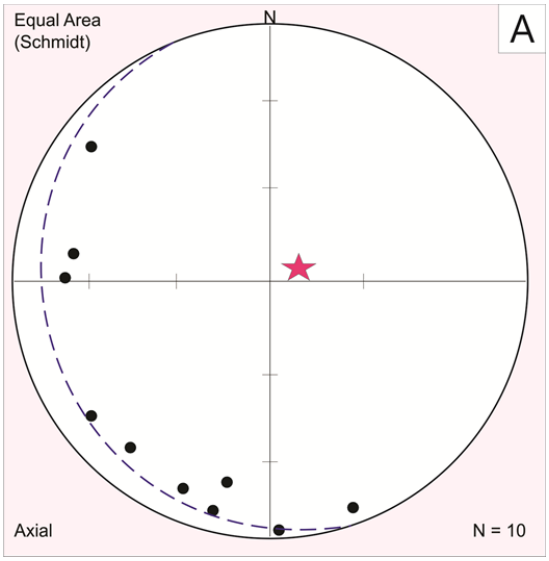

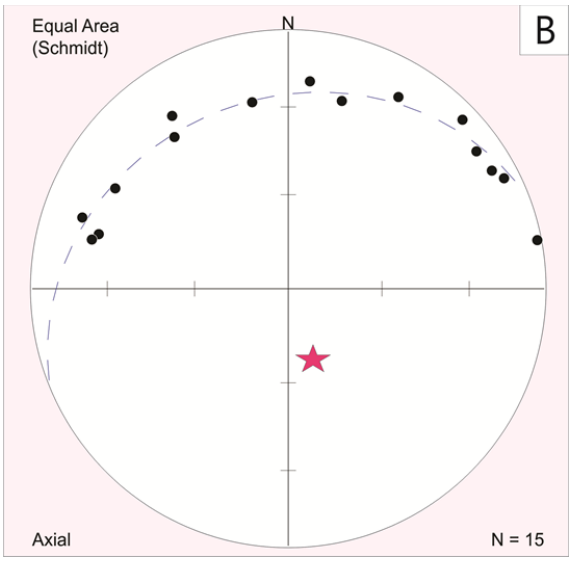

Figure 4-5a and 4-5b: Both of the figures show the S-pole diagram with β axis for different orientations (068/79 and 165/75) of F_3 Tugula outcrop.

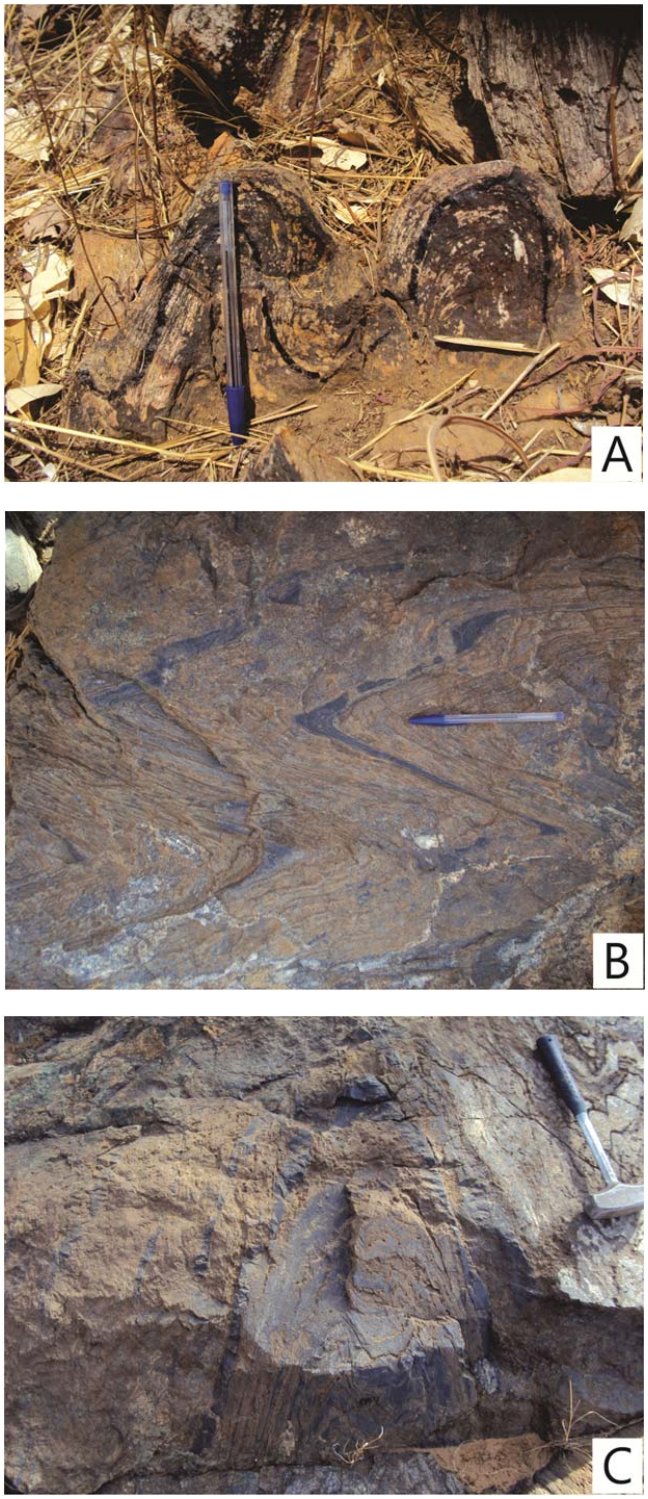

Plate 4-4 (a, b and c): A photographs showing the varying geometry of F_3 folds. Photos are from Al Beida and Tugula outcrops.

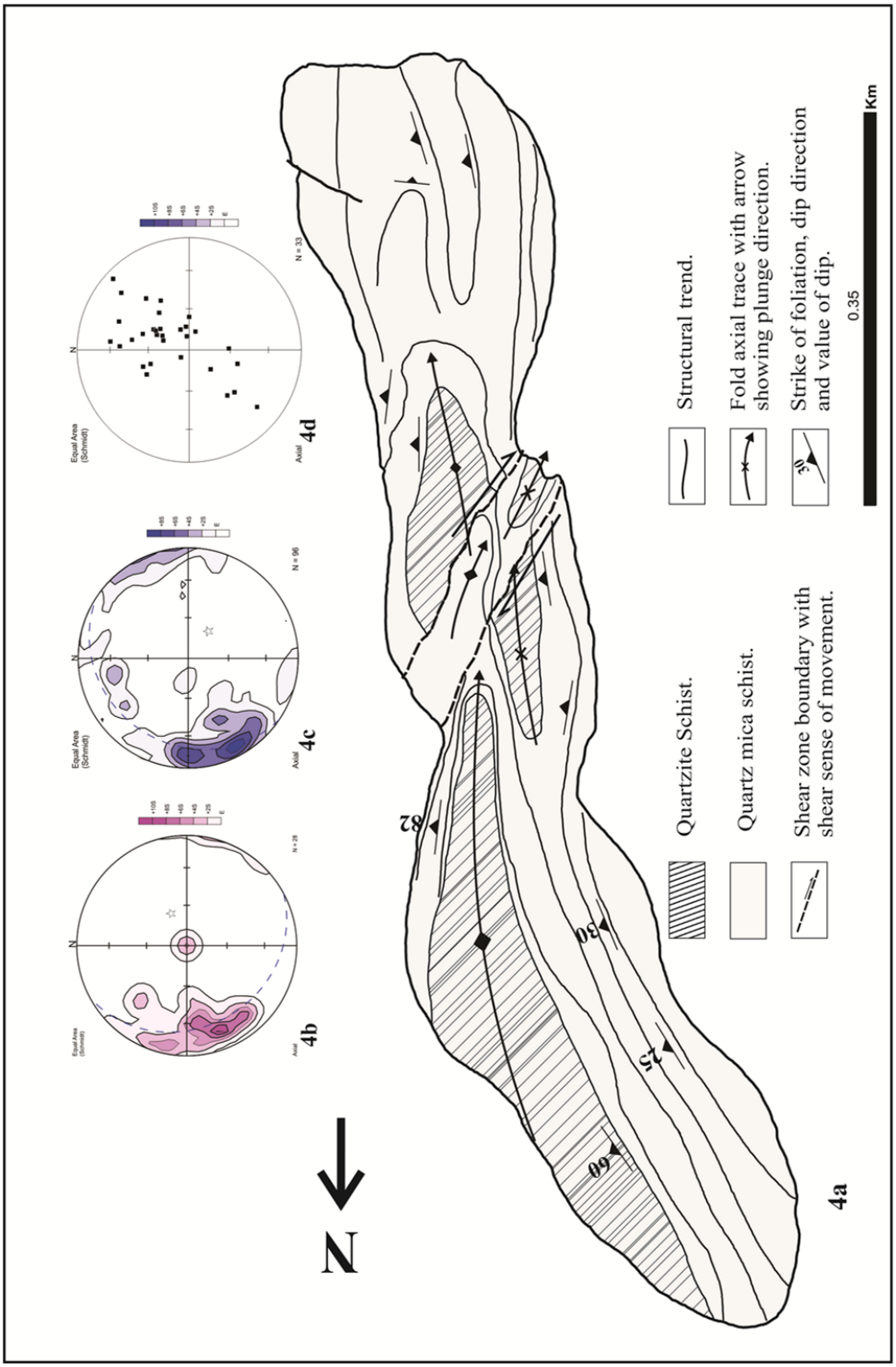

Figure 4-6: (a) Structural map of Al Beida outcrop (b) π-diagram of S_0 bedding planes (c) π-diagram of S_3 foliation planes (d) plot of axes of F_3 folds.

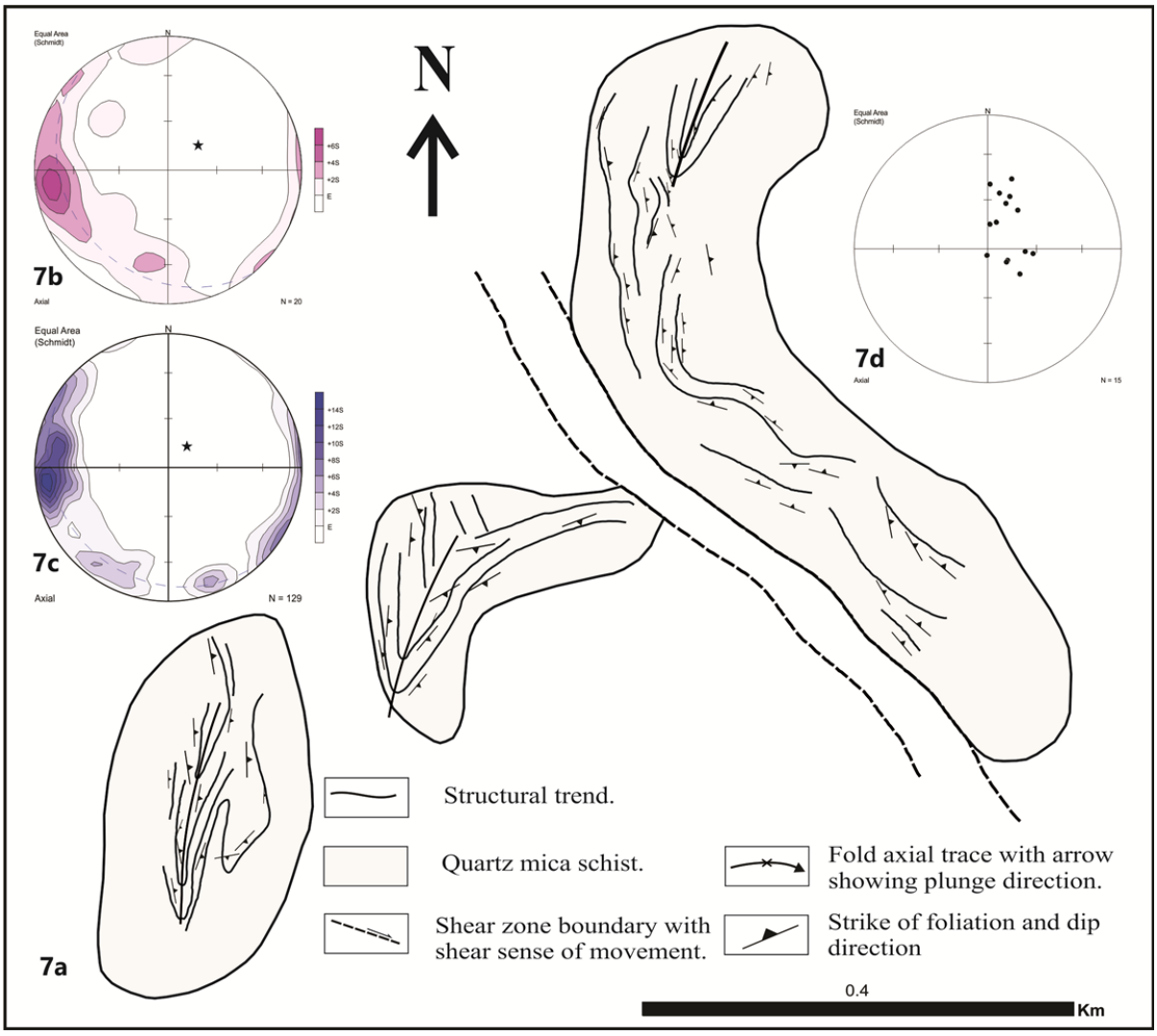

Figure 4-7: (a) Structural map of Tugula outcrop (b) π-diagram of S_0 bedding planes (c) π-diagram of S_3 foliation planes (d) plot of axes of F_3 folds.

The orientation of the axial plane and axes of these folds are dependant on their position in respect to the subsequent D_4 folds. Anticlockwise rotation and refolding of the F_3 axial plane is commonly evident at a variety of locations, suggesting the progressive deformational nature of the D_3 sinistral translation. This is also evident from the anticlockwise rotation of F_3 hinge lines (Fig. 4-6).

The main D_3 fold is preserved in the southern part of the Al Beida outcrop (Fig. 4-6). This fold plunges steeply (60˚-70˚) southeast and verges towards the west (Fig. 4-5a and 5b). An axial planar cleavage associated with D_3 folding is moderately-spaced (Plate 4-2) and is mostly steeply dipping to the southeast. The lineation associated with D_3 folding is an intersectional lineation L_{3-4} between the S_3 foliation plane and S_4 axial planar cleavage foliation, and is generally parallel to F_3 fold axes (Fig. 4-8).

The D_3 deformation is also responsible for the generation of the ophiolitic mélange. The best example is situated east of the metavolcano-sedimentary sequence of Abutulu, where fragments of gabbro and basalts are enclosed in a highly sheared matrix of mica schist.

Well preserved S_0 bedding planes are located within the graphitic slate of the Tugula outcrop. The S_0 orientation is generally dependant on its position on the F_3 folds which are steeply to vertically plunging tight to gentle folds. This led to development of a steeply dipping S_3 axial planar cleavage and intersection lineation L_{0-3}, which steeply plunges to the southeast.

4-4-2 D_4 Deformation: East-west directed compression dominant phase:

D_4 is characterized by the development of tight to open asymmetrical west-verging folds (F_4) in which both bedding planes (S_0) and foliations (S_3) are folded around northeast-trending axes in the northern Abutulu shear, and north-northwest axes in the southern Abutulu shear. F_4 fold axes are generally sub horizontal that gently plunge either towards north (common) or south (rare). These F_4 folds locally developed an S_4 cleavage which dips moderately steeply to the east (Fig. 4-9b) (Usually less steeply than the S_3 planes) and is axial planar to F_4 folds (Fig 4-9a). The orientation of F_4 axial planes remain very consistent (Fig. 4-9c), however local rotation of F_4 axial planes by D_5 conjugate shearing is not uncommon.

F_4 folding is developed on a variety of scales from mesoscopic to large scale. The major F_4 structures were mapped on the southern part of Abutulu shear zone in the Al Beida outcrop, where the southern part of the outcrop is an F_4 fold. The Al Beida structure is verging west and gently plunges to south. The eastern limb is characterized by vertical to steeply east dipping quartzite schist while the western limb is characterized by horizontal to shallow east dipping quartz mica schist (Fig. 4-6a). Occasionally the hinge zone of F_4 is occupied by very tight crenulation folding (parasitic folds).

A major change in the S_3 dip direction is recorded to the northwest of the Tugula outcrop in a series of outcrops known as Al Thawani, where steeply (60˚ – 80˚) northwest dipping turbidites extend over a kilometer length (Fig. 4-10). This reversal in S_3 dip direction suggests that the Al Thawani outcrop represents the western limb of a major northeast-trending antiform named as the Al Thawani antiform.

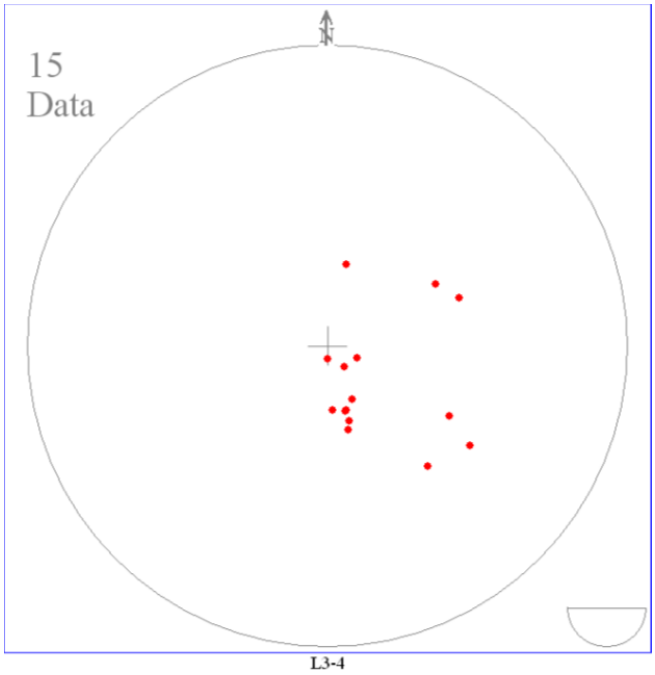

Figure 4-8: Plot of the L_{3-4} intersectional lineation.

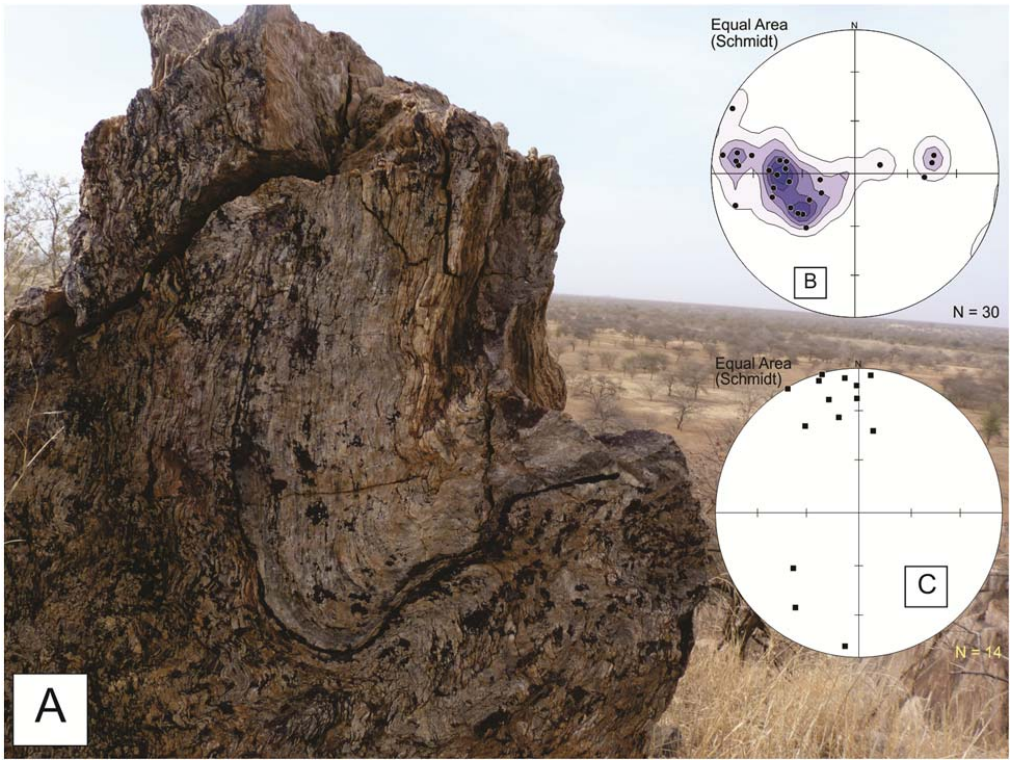

Figure 4-9: (a) A photograph showing the nature of the westerly verging F_4-fold and the development of an S_4 axial planar cleavage (b) π-diagram of S_4 axial planar cleavages (c) plot of F_4 fold hinges.

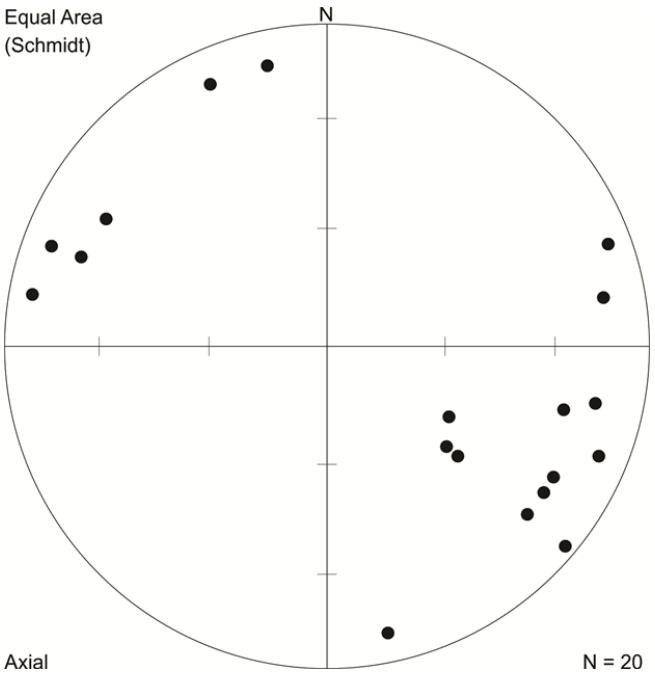

Figure 4-10: Stereographic plot of poles to S_3 planes from the Al Thwani outcrop showing a major reversal in the dip.

The graphitic slate of Tugula outcrop (Fig. 4-1) marks the eastern limb of this antiform. The hinge area of this major antiform (which is eroded and hidden under the thick Quaternary sand of the Nuba Mountains) is co-axial but not co-planar with F_4.

The planar fabric associated with D_4 is mostly in the form of an axial planar cleavage foliation. In places the S_3 foliation plane is dominant and only a weak S_4 foliation can be seen. Whereas in other places especially in the north of the Al Beida the S_4 foliation is the dominant fabric. The orientation of S_4 foliation trends north-northwest to north and dips moderately east and it remains consistent in contrast to S_3 foliation. In quartz-mica schist of Al Beida, both S_3 and S_4 axial planar cleavages can be seen together as a crenulation cleavage, which plunges gently toward the southwest. In mica-rich schist the F_4 folding is represented by kink bands.The lineation in D_4 is mainly an intersectional lineation (S3/S4) which plunges moderately either toward the NNE or SE.

4-4-3 D_5 Deformation:

D_5 is characterized by the development of minor conjugate sets of synthetic and antithetic shear zones. These zones are generally of 5-10 meter wide and can be traced for over 100 meters in the Al Beida and Tugula outcrops (Fig. 4-6a). The planes of these shear zones dip moderately to steeply either to the north-northeast (sinistral) or east to southeast (dextral). These shear zones either locally rotated the generally north – south S_3 shear planes and F_4 hinges clockwise, along northeast striking-dextral shear zones or anticlockwise along east to southeast striking sinistral shear zones (Plate 4-5) to produce the cross-cutting planar fabric S_5. The development of the S_5 planar fabric is due to a ductile bending of previous fabrics (S_3 & S_4) to parallelism along the trends of the conjugate sets of shear suggesting a ductile environment for D_5. A rigid body

translation of the S_3 & S_4 fabrics is occasionally reported indicating a possible later brittle stage for D_5. Rare development of a drag fold-like structures also indicate the initiation of D_5 shear zones in a ductile environment. The stretching lineation L_5 associated with D_5 is generally either moderately NE-plunging (sinistral) or SE-plunging (dextral). Rare steeply-plunging lineations are also documented. The stretching lineation is possibly related to a later brittle stage of the synchronous conjugate shear sets. The kinematic indicators suggest the net slip is mainly strike-slip but with a minor dip-slip component. These D_5 structures suggested an east – west directed shortening and a north – south extension.

4-5 Younger deformation:

Faulting in the Nuba Mountains is the most prominent and noticeable deformation event that affected all the lithological units from the gneisses to the post-alkaline intrusions. Three sets of faulting and lineaments were recognized both in the field and from the interpretation of Landsat image data.

NE- trending faults: The northeast-trending faults are the oldest set of faults that displace the gneisses and the low-grade metavolcano-sedimentary sequence and they usually represent thrust and minor shear contacts that separate the two units as seen in the low-grade metavolcano-sedimentary belt west of the Damik Complex (Fig. 4-1). These sets of faults have no impact on the younger alkaline intrusions. Reactivation of these faults can be seen where younger slickenside lineations are superimposed on earlier planes with stretching lineations (Plate 4-6. These slickenside lineations show a down-dip displacement suggesting a later extensional event.

Plate 4-5: A photograph showing a cross cutting fabric in the Al Beida outcrop developed by the S_5 shear planes of D_5 cutting the main S_3 foliation planes.

Plate 4-6: A photograph showing the development of slickenside lineations on the extensionally re-activated S_2 shallow-dipping thrust planes.

E-trending Lineaments: These approximately east-trending lineaments are characterized by an absence of movement and record the emplacement of granitic dykes (such as those south of Ed Deling) and veins of quartz (Kurmadi) (Fig. 4-1).

NW-trending faults: The northwest trending faults are the most recognizable set of faults that affect the younger alkaline intrusions together with the older lithologies. Characteristic wrench faults have both sinistral and dextral displacements. The amount of displacement may reach few hundred of meters as shown by the left lateral fault NE of Arid complex, and right lateral movement seen in Damik and Keig Elkhail complexes.

4-6 Kinematics and shear sense indicators:

The study of mylonites and other sheared rocks to examine geological features that are usually used to deduce the sense of shear (shear sense indicators), are an important part of understanding the deformation in shear zones. Information about shear sense indicators should always be obtained from a plane that is perpendicular to the rotational axis (vorticity vector), that is perpendicular to the mylonitic foliation and parallel to the lineation (Passchier and Simpson, 1986; Hanmer and Passchier, 1991). Movement on the Abutulu shear zone is dominantly oblique, with stretching lineation moderately pitched along sub-vertical to steeply dipping foliation planes. In such cases the horizontal plane does not truthfully represent the observation plane and one should be cautious in determination of shear sense indicators.

4-6-1 Shear sense in low-grade meta-volcanic rocks:

The graphitic slate and the mica quartz schist show excellent shear sense indicators at both microscopic and outcrop scales. Winged porphyroclasts show a ‘σ’ type (Plate 4-

7a) morphology where the tail geometry clearly indicates sinistral senses of shear. Folds, boudinaged folds and boudinaged deformed competent veins (Hanmer and Passchier, 1991) have been widely observed, their geometry showing the progressive nature of the deformation where the vein moved from the shortening quadrant to the extensional quadrant during anticlockwise rotation, indicating a sinistral sense of shear. This is also suggested from the vergence of S-shape asymmetric intrafolial folds that fold the boudinaged folds (Plate 4-7b). S-C fabrics (Plate 4-7c), where the acute angle between S and C plains suggests a sinistral sense of shear, are widely preserved in the sandy part of a turbidite sequence in the far northern part of the mapped area. The oblique quartz ribbons that show oblique foliation defined by the sigmoidal quartz lenses, similarly suggest a sinistral sense of shear. Conflicting dextral shear sense indicators are locally found in both the high-grade and the low-grade units, which may be explained as a result of either a phase of dextral shear prior to the dominant sinistral shear zone or due to a component of pure shear. The second option is favoured here, as components of pure shear are commonly seen in transpressional regimes due to strain partitioning.

4-6-2 Shear sense in the medium-grade granitic gneiss:

A well-developed S-C fabric is shown by the foliated sheared granite at the eastern boundary of Abutulu shear zone, suggesting a sinistral sense of shear. Asymmetric ‘stair stepping’ of the σ-type porphyroclasts indicate a sinistral sense of shear. Well preserved asymmetrical granitic boudins with an inferred sinistral sense of shear within the migmatites rocks are seen.

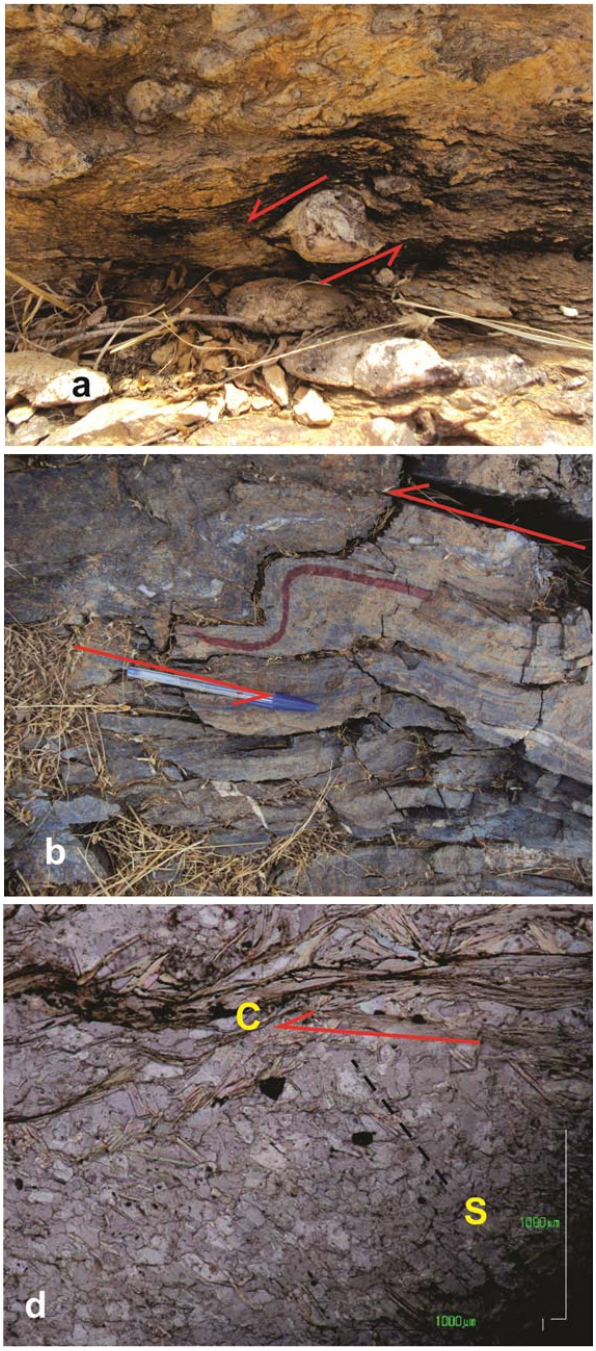

Plate 4-7: (a) Sigma-type porphyroclast (b) S-shape asymmetric fold suggesting sinistral shear (c) S-C fabric

4-7 Summary of the structural evolution of the western Nuba Mountains:

The Abutulu shear zone is a major structural feature in the western Nuba Mountains. The shear zone resulted from the oblique closure of the back-arc basin that developed on the eastern edge of the intra-oceanic arc developed over the westerly dipping Kabus subduction zone.

Structures in the study area can be viewed at as pre-Abutulu, Abutulu and post Abutulu shear zone structures. The early D_1 and D_2 are interpreted as pre-Abutulu structures that resulted from the subduction of the Kabus subduction zone. The subsequent Abutulu structures (D_3, D_4 & D_5) results from the closure and obduction of the Kabus ophiolite. D_1 and D_2 are characterized by doubly plunging folds, isoclinal to tight recumbent folds and a shallow-dipping northwest-verging thrust planes.

The Abutulu structures started with a sinistral translation dominant phase D_3 that is characterized by steeply-dipping north to northeast-trending sinistral strike-slip shear together with steeply-plunging tight to open folds. D_3 is the earliest deformation phase recognized in the volcano-sedimentary sequence which is also responsible for the formation of a tectonic mélange along the contact with medium-grade gneiss. The following D_4 deformation is mainly an east-west direct compressional phase that result in tightening of the earliest structures and led to the formation of tight to open asymmetrical west-verging folds in the Abutulu metasediments. In the Al Thwani metasediments D_4 is manifested as upright northeast trending folds. The early structures were rotated by conjugate sets of synthetic and antithetic D_5 shear zones.

The post Abutulu structures resulted from post collisional, intra-plate deformation.

5- Rb/Sr, Sm/Nd and SHRIMP-Zircon Isotopes Chemistry and Geochronology

5-1 Introduction:

The importance of acquiring geochronological data to determine the age of geological events and units of the Sudan and to correlate them with those of both of the region and the neighbouring units was long be highlighted by Vail (1990) in his compilation of the Sudan geochronological data. The need for such geochronological data in the study area (western Nuba Mountains) is indeed of vital importance due to the almost lack of existing ages (Fig. 5-1), in addition to the poor exposures which hindered the obtaining of any significant field relationships.

Abdelsalam and Dawoud (1991) suggested that the crust of the Nuba Mountains is divided along the Kabus suture into two tectonic domains, an easterly younger juvenile Neoproterozoic crust of the ANS and a westerly older mostly reworked pre-Neoproterozoic continental crust of the SMC. This suggestion is based mostly on the interpretation of the medium to high-grade gneisses of the Nuba Mountains as belonging to the cratonic crust of the now SMC, in contrast to the low-grade volcano-sedimentary domain of the ANS. Very little geochronological evidence was available to support this interpretation. Beside this, most of the data available was derived either from single sample (K-Ar) determinations or from methods known to be sensitive to late-Precambrian tectonothermal events (K/Ar and Rb/Sr).

The usefulness of the Sm/Nd method in investigating metamorphosed gneisses has been shown by Harris et al., (1984), Reischmann et al., (1985) and Schandelmeier et al., (1987). The only two Nd-model ages (Harris et al., 1984) available suggest an early Neoproterozoic crust formation age for the Nuba Mountains crust.

Geochronological results presented in this work were aimed first towards the determination of the ages of the main geological units within the basement complex and then to test the validity of the previous suggestions regarding the age and geodynamic provenance of the Nuba Mountains crust.

5-2 Analytical Techniques:

Samples SK 202A, SK 202B, SK 203, SK 204, SK 240 and SK 240A (six samples) from the Arid Unit, samples SK 14 and SK 254 to SK 258 (six samples) from the Abutulu unit and samples SK 25, SK 25A, SK 27, SK 93, SK 231, SK 234 and SK 272 (seven samples) from the medium-grade unit were selected for Rb/Sr and Sm/Nd isotope analysis. Four samples of the late-orogenic granite unit were selected for Rb/Sr and Sm/Nd isotope analysis and the first two samples in this group were selected for SHRIMP zircon dating.

Neodymium and Sr-isotope analyses were conducted at the Department of Geological Science, University of Cape Town, South Africa. Sample powders were dissolved using Hf-HNO_3 acid mixture in closed Teflon beakers on hotplates at 140°C for 2 days. Any minor undissolved material was removed by centrifuging the samples prior to sequential Sr and Nd separation chemistry (Pin et al., 1994; Míková & Denková, 2007; Pin & Zalduegui, 1997). Final Sr and Nd fractions were analysed for isotopic compositions

using a Nu Instruments DSN-100 desolvating nebuliser and NuPlasma HR-MC-ICP-MS instruments.

The external 2 sigma errors for the measured Sr and Nd isotope ratios are better than ± 0.000015. The BHVO-2 basaltic standard reference material yields values of 0.703530±0.000009 for $^{86}Sr/^{88}Sr$ and 0.513005±0.000009 for $^{134}Nd/^{144}Nd$, comparing well with published data (Weis et al., 2006).

Concentrations of Rb, Sr, Sm and Nd were measured using ICP-MS. The error on Rb/Sr and Sm/Nd is <4%. The Geodate software (Eglington and Harmer, 1999), which uses algorithms similar to those of Ludwig (1999), was used for the calculation of Sm/Nd and Rb/Sr ages. Geodate software only accepts errors given at 1σ level.

Two syn-orogenic granite samples were selected for sensitive high mass resolution ion microprobe (SHRIMP) U-Pb zircon analysis at the isotope laboratory at Australian National University.

Approximately 2 kg of samples were crushed using jaw crusher, milled and sieved to about 60 mesh at the Council for Geoscience, Pretoria. The heavy minerals (e.g. zircon, apatite and sphene) were separated from the light minerals (e.g. quartz and feldspar) using a Wilfley table. Then the zircons were separated from other heavy minerals using methylene iodide heavy liquid with a density of 3.31g/cc.

The zircon grains were mounted onto epoxy resin discs and subsequently polished to expose the centers of the grains at the laboratory of the Australian National University, Canberra, Australia. Standard zircon crystals Temora (417 Ma) as well as uranium standards from zircon of known U content (SL 13 with U content of 238ppm) were

mounted with the investigation zircon. The zircon crystals on the epoxy discs were then photographed and gold coated.

Cathodoluminescence (CL) imaging of the samples was conducted at the Electron Microscopy Unit of the Australian National University, using a FEI Verios scanning electron microscope equipped with a Gaton MonoCL4 Elite cathodoluminescence system. CL imaging was used to select the proper spots for analysis, in doing so, inclusions and mixing between different domains were avoided.

Zircon U-Th-Pb analyses were conducted using the SHRIMP II ion-microprobe at the Research School of Earth Science, Australian National University. The analytical procedures were described by Williams (1998). Spots of 25-30 μm and a depth of few micrometers (typically 1 μm) were consumed by the O_2^+ primary beam operated at ~5nA. The data for each spot were collected in sets of seven scans through the mass range. Lead correction was based on the $^{208}Pb/^{206}Pb$ ratio (Composton et al., 1984). The Temora standard zircon was used for U-Pb calibration. Analysis of the sample and the standard zircon were alternated every 3 to 4 analysis for the best control of Pb/U ratios.

Processing of the data was accomplished through the use of the SQUID program designed by Ludwig (2002) following the methods described by Williams (1998) and Ireland and Williams. The results are presented in appendix 5-1.

5-3 Field and Sample Description:

5-3-1 Arid Unit:

The Arid unit rocks are low-grade basalts (partly pillowed) and gabbro that are part of the supra-subduction arc/back arc ophiolite. Six samples from the Arid unit were used to produce Sm/Nd and Rb/Sr isochron ages, Nd model ages and different radiogenic discrimination diagrams. The samples selected comprised four basalt (SK 202a, SK 202b, SK 203 and SK 204) and two gabbro (SK 240 and SK 240a) samples. The location of the samples is shown in figure 5-1. Appendixes 3-1; 3-2; 3-3 provide descriptions of the chemistry of the samples and they are discussed in chapter three.

5-3-2 Abutulu Unit:

The metavolcanic rocks of Abutulu are interpreted as evolved arc/back-arc-related lavas (chapter 3). Five samples of meta-andesite and basaltic andesite (SK254, SK255, SK256, SK257 and SK258) and one acidic metavolcanic (SK14) were used for Sm/Nd and Rb/Sr isotope geochronology and geochemistry. Location of the samples is presented in figure 5-1. The isotopic data for the samples are provided in appendixes 5-1 and 2 and their chemistry and petrography discussed in chapters two and three.

5-3-3 Medium-grade gneiss and syn-orogenic granite:

The medium-grade gneiss unit represents the major unit within the mapped area and consists of ortho- and paragneiss. Detailed description of the protololith characterization is provided in chapter 2. Biotite gneiss and minor hornblende biotite-bearing varieties with SiO_2 content > 60% are considered as orthogneiss.

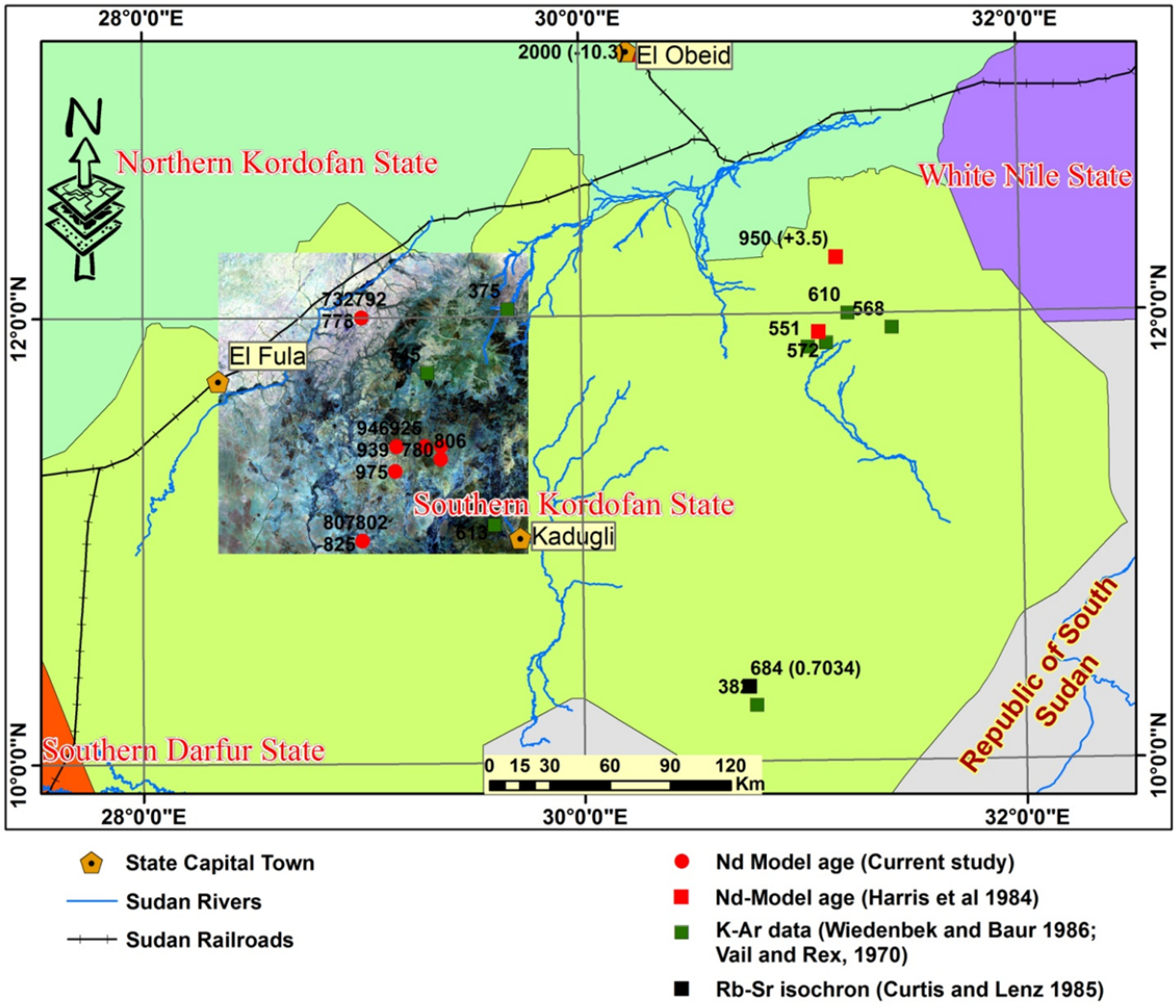

Figure 5-1: Location of geochronological sample sites for rocks representing the different lithological units within the study area.

Foliated biotite syn-orogenic granite with similar mineralogical composition and chemistry are also grouped within the gneiss unit. Six samples of the orthogneiss and the syn-orogenic granite were used for Sm/Nd and Rb/Sr isotopes studies.

Three samples (SK25, SK25A and SK27) out of the six were selected from the vicinity of Jebel Tareen immediately east of Jebel Lagawa from one of the major post-orogenic intrusions in the map area. Locations of the samples are shown in figure 5-1 and their isotopic data presented in appendix 5-2. The petrography and chemistry of the samples were described in chapter 2 and 3.

5-3-4 Late-orogenic Intrusions:

Four samples (SK4, SK5, SK224 and SK275) from the late-orogenic granite were selected for Rb/Sr and Sm/Nd isotope studies. From the four samples samples SK4 and SK5 were selected for zircon separation and further SHRIMP analysis, the two zircon fraction were labeled ZR1 and ZR2.

5-4 Results:

5-4-1 Sm-Nd and Rb-Sr whole rock dating and initial ratios:

5-4-1-1 Arid unit:

The six Arid unit samples produced an isochron age of 832±241 Ma and initial $^{143}Nd/^{144}Nd$ ratio of 0.51187±0.000253. The MSWD = 2.3. The $\varepsilon Nd_{832\pm241}$ = +6.2±4.9 (Fig. 5-2a). The Arid unit samples have low Rb/Sr ratios which prohibited the calculation of a meaningful age.

5-4-1-2 Abutulu unit:

The six Abutulu samples define an errochron of 768±123 Ma, Nd initial ratio (NdIR) at 768Ma = 0.51194±0.000117 and $\varepsilon_{Nd768\pm123}$ = +5.8±2.3 and a MSWD = 3.1 for the 6 whole rock errochron (Fig. 5-2b). When both of the Arid and Abutulu unit samples are plotted together, they define a 12 WR Nd isochron of 778±90 Ma, $NdIR_{778}$ = 0.51193±0.000090 equivalent to ε_{Nd}778±90 = +5.9±1.8 (Fig. 5-2c). The meta-andesite and basaltic andesite of the Abutulu unit provide a 6 point Rb/Sr isochron (MSWD = 1.3) of 582±10 Ma (Fig. 5-3) equivalent to a Sr initial ratio (SrIR) = 0.70421±0.000358.

The 778±90 Ma age is interpreted as the emplacement age of the arc magma and the ε_{Nd} value of +5.9±1.8 as that of the mantle magma source. The 778±90 Ma emplacement age is used in the calculation of the initial Nd and Sr ratios and the ε_{Nd} value for the Arid and Abutulu units (Appendix 5-1).

Both the samples of the Arid and the Abutulu units have ε_{Nd778} average value of eleven samples of +6.0±0.5 and an average initial Nd ratio of 0.511899 and average initial Sr ratio of 0.703593.

5-4-1-3 Medium-grade gneiss and syn-orogenic granite:

Six samples of the medium-grade biotite gneiss and the syn-orogenic granite define an Nd isochron of 976±58 Ma and an initial Nd ratio of 0.511699±0.000043 equivalent to ε_{Nd} value of +6.3±0.9. The MSWD value = 2.0 (Fig. 5-4a). When we only plot the three syn-orogenic granite samples of Jebel Tareen they define Nd isochron of 982±63 Ma, NdIR = 0.511700±0.000050 (εNd = 6.5±0.9), MSWD = 2 (Fig. 5-4b).

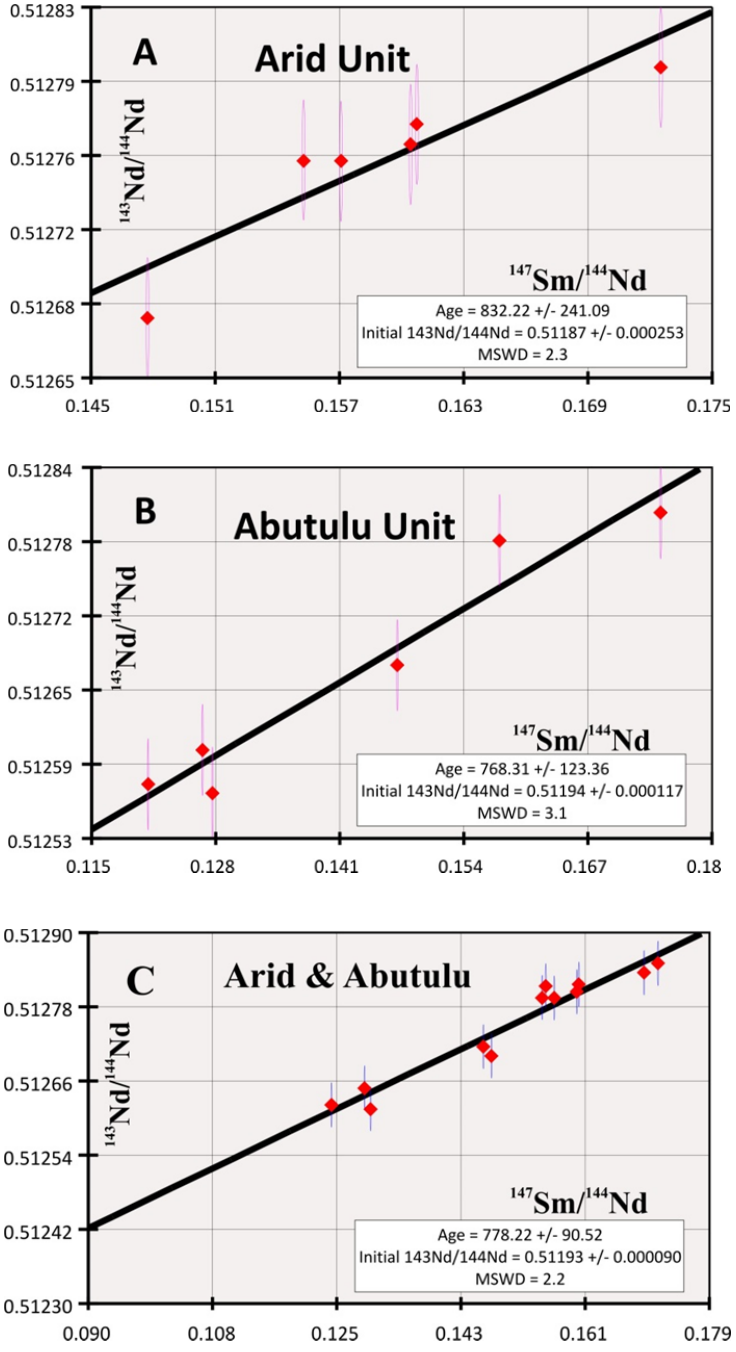

Figure 5-2: Sm=Nd isochrons for (A) the six Arid basalt and gabbro (B) six Abutulu meta-andesite and (C) the 12 sample from both Arid and Abutulu unit.

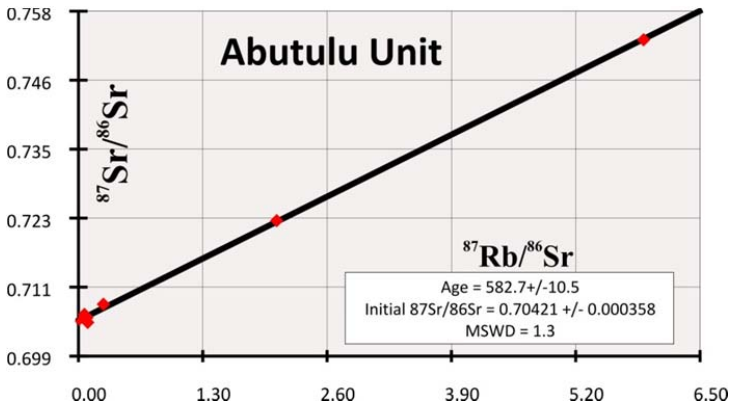

Figure 5-3: Rb-Sr isochron for the six meta-andesite samples from the Abutulu unit.

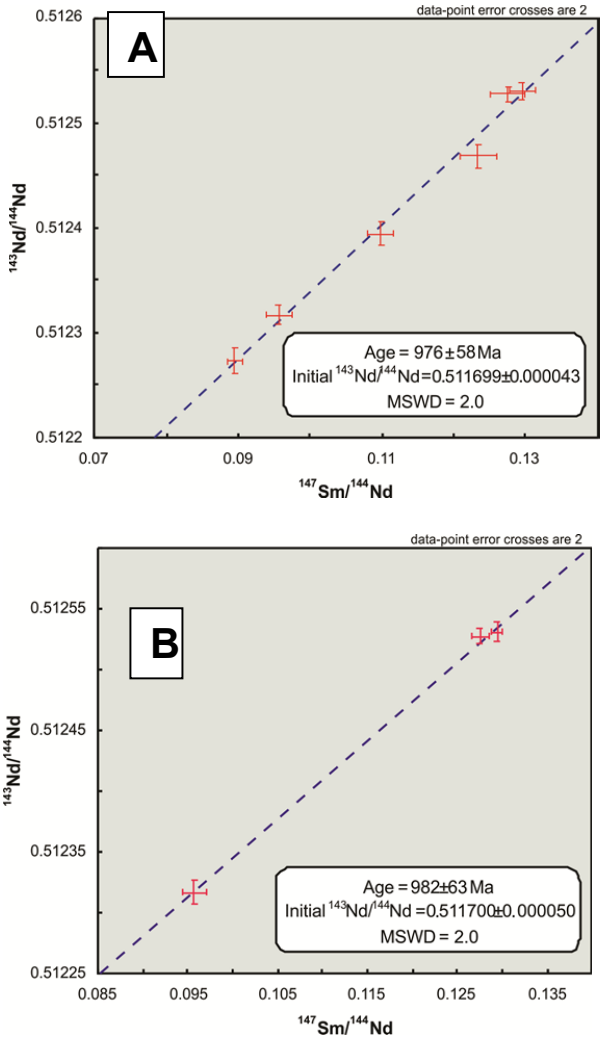

Figure 5-4: Sm-Nd isochron for (A) the six gneiss and syn-orogenic granitoids. (B) Three syn-orogenic granite samples.

An imprecise Sr isochron of 690±280 Ma resulted from the plotting of six point gneiss and syn-orogenic granite (not provided). The initial Sr ratio value = 0.703±0.026 and the MSWD value = 79. The great uncertainty in the Sr age and the MSWD value far beyond the analytical uncertainty suggest that the Rb/Sr isotopic system may have suffered post-magmatic open system behavior.

However, when we plot only the samples of Jebel Tareen, they produced a three point isochron of 854±34 Ma, SrIR = 0.6965±0.0033 and a MSWD value = 2.4 (Fig. 5-5).

5-4-1-4 Late-orogenic intrusions:

Four late-orogenic granite samples produced an Nd isochron age of 636±75 Ma with MSWD = 1.4. The corresponding initial $^{143}Nd/^{144}Nd$ ratio = 0.512029±0.000043 (equivalent to ε_{Nd} = +4.2) (Fig. 5-6).

The Sr isochron for the same for sample define an age of 595±16 Ma with NSWD = 1.7 (Fig. 5-7). The corresponding initial ratio SrIR = 0.70325±0.00045

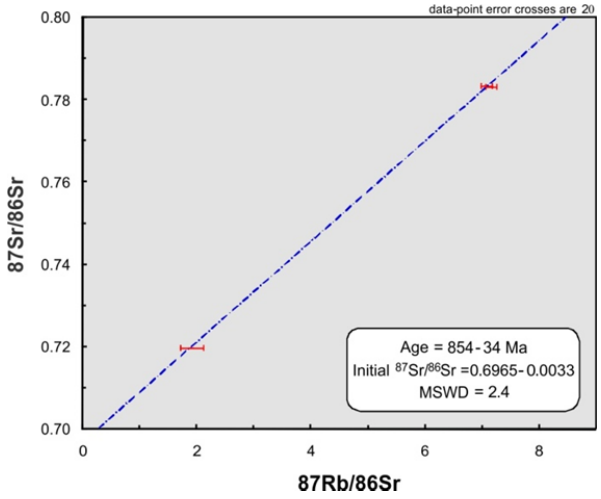

Figure 5-5: Rb-Sr isochron for the three syn-orogenic granite samples.

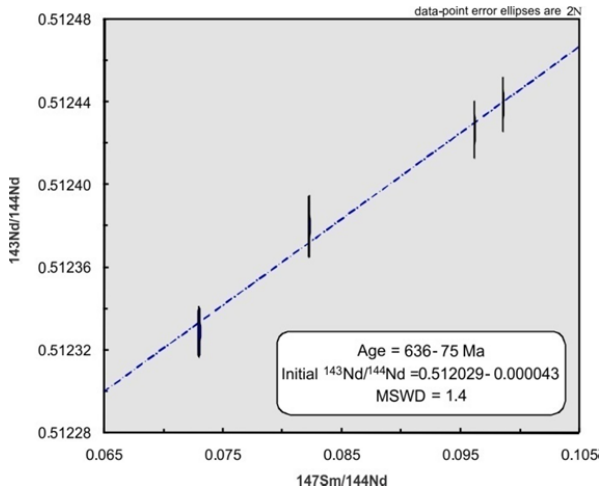

Figure 5-6: Sm-Nd isochron for the four samples of the late-orogenic granite.

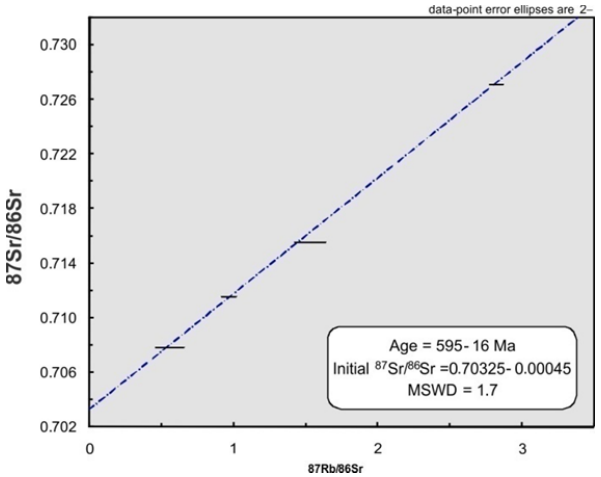

Figure 5-7: Rb-Sr isochron for the four samples of the late-orogenic granite.

5-4-2 Epsilon Nd and T_{DM} model ages:

The values of ε_{Nd} and T_{DM} Nd model ages for 22 samples, six from the Arid unit, six from the Abutulu unit, six from the gneiss unit and 4 from the late-orogenic intrusions unit are presented in appendixes 5-1 and 5-2.

The ε_{Nd} values for the four units were calculated at the best available crystallization age (778 Ma for both Arid and Abutulu unit, 976 Ma for the gneiss unit and 600 Ma for the late-orogenic intrusions). The first three units have very similar ε_{Nd} values that range from +6.8 to +5.3, with an average ε_{Nd} of +6.0±0.5 for both Arid and Abutulu units and an average of +6.2±0.6 of the medium-grade gneiss unit. The overall average for the 18 samples representing the entire three units is +6.1±0.6.

The late-orogenic intrusion unit has lower ε_{Nd} values that range from +3.5±1 to +3.8±1 with average of +3.6±1.

The idea behind the method of T_{DM} Nd model ages is to calculate at what age the sample has a $^{143}Nd/^{144}Nd$ ratio similar to that of depleted mantle. Calculation of Nd model age requires a realistic assumption about the composition of the depleted mantle that produced the rocks under investigation. The two models of DePaolo (1981); Nelson and DePaolo (1985) and Goldstein et al., (1984) are widely used. The latter model of Goldstein et al., (1984) is a linear between εNd equal +10 today and εNd equal 0 at 4.6 Ga, while the DePaolo (1981) is a quadratic expression that utilizes the value of modern oceanic island arc of +8.5 (calculated by the formula $\varepsilon T_{DM(T)} = 0.25T^2 - 3T + 8.5$). In this study, we followed the method of Nelson and DePaolo (1985) in the calculation of the T_{DM} Nd model age for the metavolcanic samples. Since the metavolcanic rocks have

generally high Sm/Nd values that are very close to those of mantle which give rise to unrealistic Nd Model ages. We applied the filter that used by Stern (2002) in which only samples with $^{147}Sm/^{144}Nd$ <0.165 were selected (excluding only one sample; SK240 which has $^{147}Sm/^{144}Nd$=0.1744).

For the felsic igneous rocks, where possible second Sm/Nd fractionation may have occurred (the first having occurred due to mantle melting) as a result of intracrustal process such as crustal partial melting, magma mixing, etc., a two stage depleted mantle may be calculated (Champion, 2013). For the gneiss unit and the late-orogenic granitoids a two stage depleted mantle model age is calculated using the equation and values for depleted mantle ($^{143}Nd/^{144}N$ and $^{147}Sm/^{144}Nd$) and the value of the average crustal reservoir ($^{147}Sm/^{144}Nd$) of Liew & Hofmann, (1988).

The single stage model ages for the 12 metavolcanic rocks of Arid and Abutulu units strongly shows the same age with an average for the Arid unit of 836 Ma and ranges from 778 Ma to 905 Ma, and an average for the Abutulu unit of 805 Ma and ranges from 732 Ma to 859 Ma (appendix 5-1). Ages similar to the Abutulu metavolcanic rocks are shown by the late-orogenic intrusions, with an average of 792 Ma and ranges from 776 Ma to 807 Ma.

The gneiss unit samples show single stage depleted mantle model ages that are older, with an average of six samples of 948 Ma and ranges from 925 Ma to 975 Ma.

The two stage depleted mantle model ages for both the gneiss unit and the late-orogenic intrusion unit show results that are slightly older than those obtained from the single stage model ages. The average of the six ages of the gneiss unit is 1066 Ma and

ranges from 1031 Ma to 1081 Ma. The two stage model age results for the syn-orogenic intrusions unit are not much different from the gneiss unit, in that they show approximately 0.1 Ga older ages (appendix 5-2).

5-4-3 U-Pb SHRIMP dating of zircon:

Most of the zircon grains obtained from sample ZR-1 tend to have rod-shaped, doubly terminated crystals with a length to width ratio (elongation ratio) of ≈ 4 (in the upper part of the 1 to 5 elongation rate range of Corfu et al., 2003). These narrow-width crystals are common in rapidly crystallized high-level granites (Corfu et al., 2003).

All of the analysed crystals have core-rim structures evident in the cathodoluminescence (CL) images (Fig. 5-8). Most of the cores have bright-luminescence on CL, surrounded by dark luminescent rims of various widths. Xenocrystic cores are not uncommon in many igneous intrusions. They may occur as rounded cores mantled by the newly developed zircon rims or as unmantled subrounded or rarely euhedral grains (Corfu et al., 2003).

Well developed oscillatory zoning occurred in both the cores and rims of all of the 5 analysed zircon crystals (Fig. 5-8). Growth zoning is a typical feature of magmatic zircons (Corfu et al., 2003); the zoning reflects compositional variations in Zr, Si, U, Th, trace and REE elements (Fowler et al., 2002; Corfu et al., 2003). Two measures from a single grain from sample ZR-1 produced $^{206}Pb/^{238}U$ ages of 574±9 Ma (spot 3-1 core) and 589±6 Ma (spot 3-2 rim). This younger age of the core possibly reflects lead loss. These two measures correspond to Th/U ratios of 0.40 (core) and 0.16 (rim) respectively. The oscillatory zoning and the relatively high Th/U ratio of the core (spot

3.1; Fig. 5-8) could possibly suggests a magmatic origin of the core (Rubatto and Gebauer, 2000; L. Zhang et al., 2006). Six zircon analysis yield a mean $^{206}Pb/^{238}U$ ages of 599.8±5.8 Ma (MSWD = 1.4) (Fig. 5-9).

The zircon grains from sample ZR-2 have lower elongation ratio ≈ 3 and larger sizes with an average of 114 and 264 µm in major dimensions (Fig. 5-10). Similar to sample ZR-1, all of the 13 analysed grains of sample ZR-2 have core-rim structures (Fig. 5-10). With the exception of grains 2 and 9, all of the other zircon grains are also similar to those of sample ZR-1 in having brighter luminescent cores and darker luminescent rims (Fig. 5-10). This darker luminescent core corresponds to higher U content (568 ppm) compared to the rim (536 ppm).

Variation in the U contents between the core and the rims measured in three zircon crystals, numbered 2, 5 and 8 (Fig. 5-10) of sample ZR-2 show that the U content is lower in the core in crystals 5 and 8 (280 and 457 ppm), while in the rim is 1225 and 1230 ppm and is higher in crystal 2 (568 ppm and 536 ppm in the rim). Analysis of one core produced a $^{206}Pb/^{238}U$ age of of 743±8 Ma (Appendix 5-2). Since the analysis is discordant the 743±8 Ma is a minimum age of the zircon core. The analysis of eight zircon rims of sample ZR-2 produced a mean $^{207}Pb/^{206}Pb$ age of 607±10 Ma (MSWD = 0.59) (Fig. 5-11). The Th/U ratios are higher in the cores (0.26 – 0.43) compare to the rims (0.04 – 0.08). Higher Th/U ratio (>0.1) suggests a magmatic origin (Rubatto and Gebauer, 2000) and hence 743±8 is interpreted as the age of source of the granite. Analyses of magmatic zircon produced concordant dates between 624±7 Ma (core 2.2) and 605±10 Ma (rim 5.1). These are interpreted as a crystallization age. Metamorphic rims discordant dates of 614±8 Ma to 583±6 Ma are nearly indistinguishable from the

magmatic rims ($^{206}Pb/^{238}U$ age 613±6 Ma to 605±10 Ma) and hence a contemporaneous magmatic and high temperature metamorphism is suggested around ≈ 600.

Sample	Rb-Sr isochron/errochron ages	Sm-Nd isochron/errochron ages		Sri at 778Ma	Ndi at 778Ma	εNd at 778±90Ma	TDM Ma
1sk-202a		832.22±241.09 Ma Ndi = 0.51187±0.000253 MSWD = 2.3		0.703537	0.511919	+6.4±0.5	778
sk202b				0.703572	0.511908	+6.2±0.4	802
sk-203b				0.704058	0.5119	+6.1±0.4	825
sk-204				0.70393	0.511907	+6.2±0.5	807
sk-240				0.702349	0.511879	+5.7±0.3	905
sk-240a				0.702797	0.511867	+5.3±0.6	899
		12 samples isochron 778.22±90.52 Ma	The 778±90 Ma obtained from both Arid and Abutulu Units is considered as age for arc emplacement (crystallization age)				
sk-254	589.8±13.6 Ma Sri = 0.70376±0.000288 MSWD = 1.3 Age suggests later resetting for Abutulu Unit	768.31±123.6 Ma Ndi = 0.51194±0.000117 MSWD = 3.1		0.703275	0.511876	+5.7±0.3	859
sk255				0.698354	0.51188	+5.5±0.8	792
sk256				0.687676	0.511918	+6.2±0.8	789
sk257				0.704537	0.511919	+6.3±0.8	854
sk258				0.703732	0.511886	+5.7±0.6	778
sk-014				0.704146	0.511937	+6.8±0.5	732
Sample				Sri at 982Ma	Ndi at 982Ma	εNd at 982±63Ma	TDM Ma
SK 25	Three points 854±34 Ma Ndi = 0.6965±0.0033 MSWD = 2.4 Possible resetting of the gneisses	982±63 Ma Ndi = 0.5117±0.000050 MSWD = 2.0 Age considered age crystallization age for the igneous protolith of the gneisses		0.683274	0.511911	+6.4±0.5	925
SK 25A				0.684693	0.511906	+6.2±0.5	939
SK 27				0.693155	0.511911	+6.3±0.8	946
SK93				0.66473	0.511773	+6.1±0.6	957
SK231				0.700251	0.511767	+6.3±0.8	949
SK234				0.656229	0.51177	+5.9±0.5	975
			U-Pb Concordia	Sri at 778Ma	Ndi at 778Ma	εNd at 778±90Ma	TDM Ma
SK4/ZR1	595±16 Ma Sri = 0.70325±0.00045 MSWD = 1.7	636±75 Ma Ndi = 0.512029±0.000043 MSWD = 1.4	Mean $^{206}Pb/^{238}U$ 599.8±5.8 Ma	0.703088	0.512025	+3.7±0.1	807
SK5/ZR2			Mean $^{207}Pb/^{206}Pb$ 607±10 Ma	0.703316	0.512029	+3.8±0.1	776
SK224			Above ages represents metamorphic ages	0.70252	0.512038	+3.6±0.1	806
SK275				0.703082	0.512026	+3.5±0.1	780

Table 5-1: Showing the results of the various isotopic systems (ages, initial ratios, model ages and epsilon values) for the different investigated rock units and their geological interpretation.

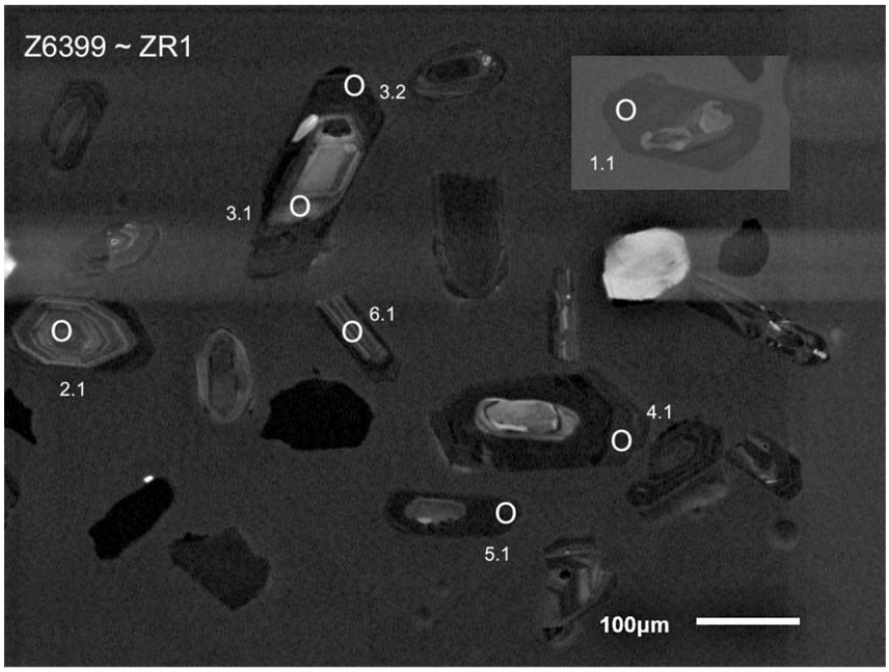

Figure 5-8: CL images of doubly-terminated zircon crystals for SHRIMP U–Pb analyses from the late-granite of sample ZR1.

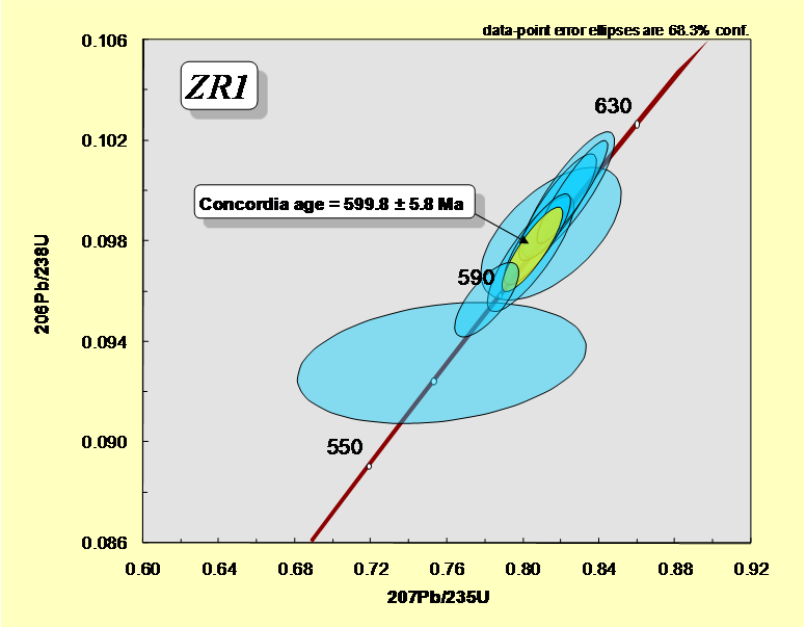

Figure 5-9: Concordia diagrams showing results of SHRIMP data from sample ZR1.

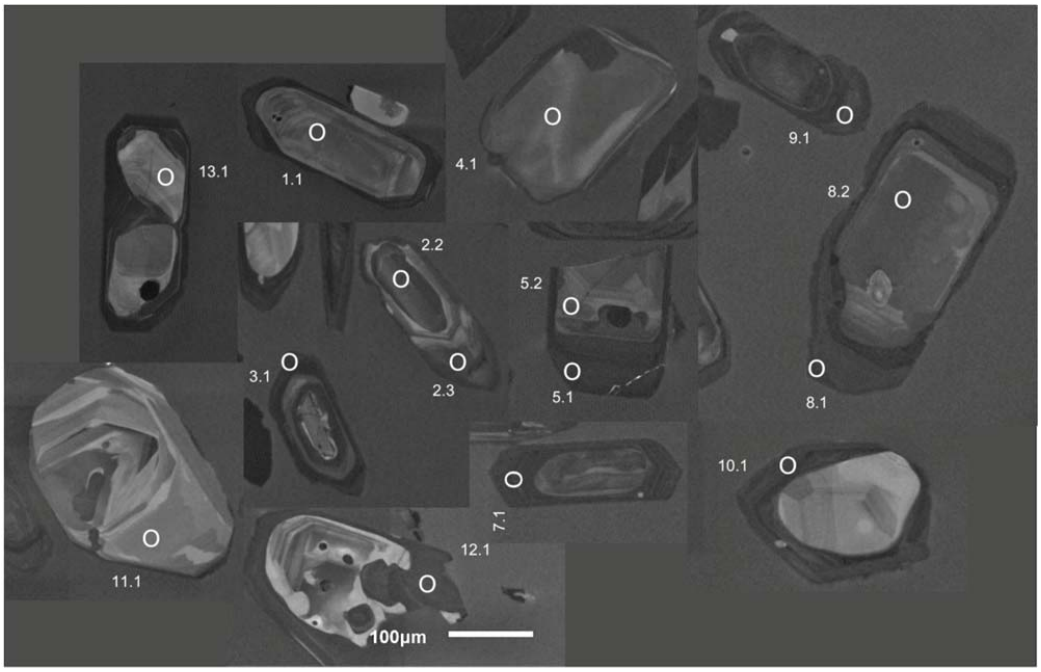

Figure 5-10: CL images of zircon crystals for SHRIMP U–Pb analyses from the late-granite of sample ZR2.

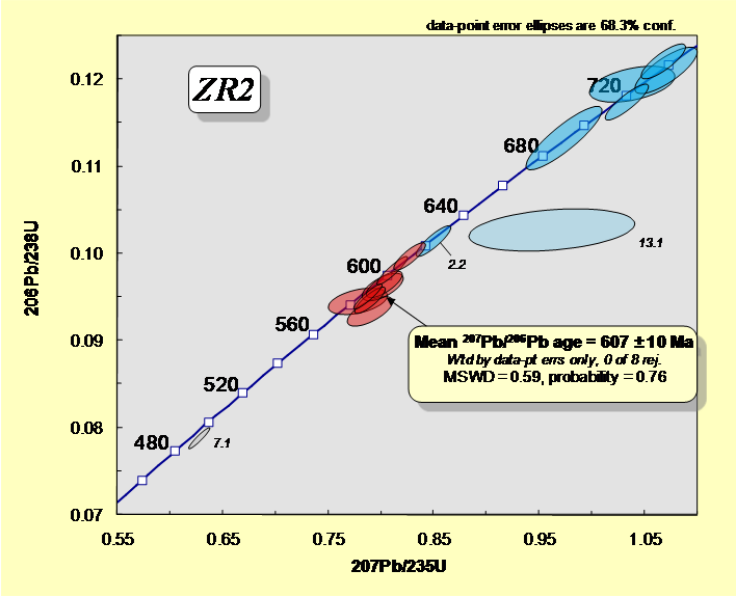

Figure 5-11: Concordia diagrams showing results of SHRIMP data from sample ZR2.

6- Discussion and proposed tectonic model:

6-1 Lithology, chemistry, structure and isotopic data of the low-grade and medium-grade domains:

Geological mapping of the area between Lagawa in the east, El Fula in the west, Abu Zabad in the north and Gingaro in the south reveals the southwestward continuation of the NE-trending belt of low-grade metavolcano-metasedimentary rocks from Abu Zabad through the known occurrences at Jebel Abutulu and further to the southwest. The western contact of these low-grade rocks is hidden under the Quaternary sedimentary cover of central Sudan. From the east it is structurally bounded by a sequence of medium-grade gneiss and migmatite with associated supra-crustal metasediments. This latter unit is the dominant unit within the mapped area and extends further east for approximately 300 km up to the Kabus Ophiolitic mélange (the western boundary of the ANS in central Sudan).

There is no consensus among the geoscientists who investigated the Nuba Mountains regarding the metamorphic grade, age, position within the stratigraphic column and the geodynamic context of the gneiss and migmatite units. Authors, including Vail (1973; 1978), El Ageed and El Rabaa (1981), Abdelsalam and Dawoud (1991) consider these rocks to represent high-grade (amphibolite to granulite facies of regional metamorphism) gneiss and migmatite of pre-Neoproterozoic age, mostly reworked during the Pan-African Neoproterozoic orogeny and that they represent a basement to the subsequent lithological units. However, in more recent publications, Vail, (1983)

and Sadig and Vail (1986) developed a different opinion, where they suggested that the gneisses are composed of (at least in part) sheared and metamorphosed batholitic granitoids or sedimentary units and may only represent limited areas of higher heat flow and doming within the greenschist facies unit. This opinion was adopted by Brinkmann, (1986) who concluded that there are no signs of amphibolite facies regional metamorphism in the Nuba Mountains. The gneisses only represent a mineral paragenesis indicative of a quartz-albite-epidote-almandine subfacies, the highest grade within the greenschist facies.

In the current study we classify the gneiss and migmatite rocks into two subunits; an orthogneiss unit (granitic and quartz monzonitic gneisses) and supracrustal metasediments (paragneiss, calc-silicate, chert, graphite, and quartz mica schist). Isolated outcrops of syn-orogenic granite are present within this metamorphic assemblage.

The mineralogy of the orthogneiss suggests amphibolite grade metamorphism rather than the quartz-albite-epidote almandine subfacies of Brinkmann (1986), because of the presence of oligoclase (together with albite) which marks the transition from greenschist to amphibolite facies metamorphism. Also the paragneisses of the supracrustal rocks show mineral paragenesis indicative of amphibolite facies of metamorphism, similar to the orthogneiss. The presence of diopside in the calc-silicates also indicates amphibolite facies metamorphism.

The geochemistry of both the medium-grade orthogneiss and the syn-orogenic granite are typical of calc-alkaline I-type granitoids. Both of these units show close similarities in

the N-MORB multi-element spidergram and the chondrite normalized REE diagrams where they show features of subduction related magmatism (negative Nb-Ta anomaly and LREE enrichment). These orthogneiss samples are interpreted to be derived from a felsic arc volcanic protolith. Evidence of crustal contamination in the orthogneiss is suggested by the high Th contents and low U/Th ratios.

Two early phases of deformations (D_1 and D_2) were recognized in the medium-grade metamorphic assemblages that did not affect the subsequent units. D_1 is characterized by the development of a mappable-scale doubly-plunging synform (F_1) and the development of strong S_1 foliation planes. D_2 is characterized by the presence of tight to isoclinal recumbent folds (F_2) and is associated with shallow-dipping northwest-verging thrust planes. The lineation associated with D_2 deformation is a shallow, southeast-plunging L_2 stretching lineation. These two phases of deformation are best interpreted to represent an early collisional phase associated with the closing of the oceanic basin responsible for the development of the Kabus ophiolitic mélange.

Three syn-orogenic granite samples around Jebel Tareen define an Nd isochron of 982±63 Ma, NdIR = 0.511700±0.000050 (εNd = 6.5±0.9), MSWD = 2. Also the three analysed gneiss samples from two locations fall within the same isochron giving a Nd isochron of 976±58 Ma and an initial Nd ratio of 0.511699±0.000043 equivalent to ε_{Nd} value of +6.3±0.9. These ages are very similar and the Nd initial ratios are homogenous. Such results are difficult to obtain by metamorphism considering the size of the area covered by the samples (Fig. 5-1). The age of 976±58 Ma is interpreted to represent the age of emplacement of the arc magma and the ε_{Nd} value of +6.3±0.9 to represent that of the mantle magma source. The ε_{Nd} values of the six samples of gneiss

and syn-orogenic granite calculated at 976±58 Ma gave a range between +6.4±0.5 and +5.9±0.5 with an average of +6.2±0.6.These data first suggest that there is no significant involvement of pre-Neoproterozoic crust, since such involvement should result in the presence of significantly negative ε_{Nd} values. It secondly indicates derivation from a depleted mantle source with a time integrated Nd depletion relative to Sm. To solve the conflict of crustal contamination indicated by the Th enrichment (range between 18.2 ppm to 43.3 ppm) it could be suggested that the Nuba Mountains island arc reached a considerable thickness to allow Th enrichment, as suggested for the Birimian island arc (Ama Salah et al., 1996) and the Bayuda arc (Küster and Liégeois, 2001), or a pre-Neoproterozoic crust may occur beneath the Nuba Mountains in a thickness that is insufficient to allow significant contribution to the chemistry of the arc magma that is detectable isotopically. Nd T_{DM} model ages are effective means of estimation of the mean age of the protolith of a geological unit whether magmatic or sedimentary (DePaolo, 1983; Liégeois and Stern, 2010). The values of the Nd T_{DM} model ages calculated following the method of Nelson and DePaolo (1985) clustered around an early Neoproterozoic age of 948 Ma (an average of six samples that range from 925 Ma to 975 Ma). Calculation of a two-stage model age for felsic rocks may be needed under certain conditions discussed in the previous chapter. However, the calculation of a two-stage model age will only result in an age that is approximately 100 Ma older, but most importantly there is no reason for such calculations. The Nd T_{DM} model ages of the six samples are clustered very close to the 976 Ma crystallization age of the same rocks, indicating the juvenile nature of the crust. The Nd T_{DM} model age

values also support the notion of no to insignificant involvement of much older crustal material hence the data then would show a larger spread of Nd model ages.

The outcrops within the metavolcano-sedimentary belt are generally scattered and found as isolated hills with low-topography. Outcrops are of basic to intermediate metavolcanic rocks, slate, phyllite, graphitic and mica quartzitic schists. Mafic complexes are found only along the eastern flank of the metavolcanic rocks. The nature of the latter complexes is similar to that of oceanic crust with a cumulate section composed mainly of layered gabbro and an upper section mainly of massive gabbro and basaltic pillowed lavas. The sheeted dolerite dykes and the basal section typical of preserved ancient ocean crust have not been observed except for talc-carbonate rocks found at the southern part of Al Beida which may be interpreted as altered serpentinite ultramafic rock, and thus part of the typical basal sequence. Conventionally, the existence of sheeted dolerite dykes from sea floor spreading in ophiolite is considered as strong evidence for the origin of oceanic crust now exposed on land, (Gass, 1990; Moores and Vine, 1971). This idea is now debated (Dilek and Furnes, 2011) since the formation of a sheeted dyke complex requires a delicate balance between the spreading rate and the magma injection rate, which is difficult to maintain in a supra-crustal tectonic environment (Robinson et al., 2008). The absence of sheeted dykes may indicate a spreading rate lower than the rate of magma production in the region (Robinson et al., 2008; Dilek and Furnes, 2011). The rock association and structure of the mafic and ultramafic rocks are similar to rock associations defined as ophiolitic by the Penrose conference (Anon, 1972; Coleman, 1977). Also, the absence of any thermal impact of these complexes on the surrounding gneisses and the absence of any

mafic off-shoots and apophasis along the surrounding bounding lithologies support their ophiolitic origin.

Petrographical studies of both the metavolcano-sedimentary sequence as well as the mafic and ultramafic complexes show mineral assemblages of epidote, chlorite, actinolite and albite, indicative of greenschist facies metamorphism. A high-pressure metamorphic event is suggested by the presence of glaucophane within the mineral assemblage of the metasedimentary rocks (Mansour and Iskander, 1960). This metamorphic rock association is in sharp contrast to the medium-grade (amphibolite facies) granitic and granodioritic gneisses to the east. The steeply southeasterly dipping shear zone is considered to mark the boundary between the two units.

Geochemical data facilitated the identification of two groups of volcanic rocks which correlate with evidence from the field: Back-arc (suprasubduction ophiolite) meta-basite, meta-gabbros and minor hornblendite (Arid unit) and arc metavolcanic rocks, mainly andesite and subalkaline basalts (Abutulu unit). The mafic to ultramafic group shows a transitional nature from tholeiitic to calc-alkaline and most of them are basaltic with minor basaltic andesite, while the arc meta-andesites are mainly calc-alkaline.

With the exception of ultramafic cumulate samples that have high Mg# (≈69.14, MgO ≈ 21.2%, Cr ≈ 2778.7 ppm and Ni ≈ 831 ppm) all of the mafic massive gabbros, pillowed basalts and basaltic andesites have low concentrations of MgO (< 9.99%, Cr < 289 ppm and Ni <95 ppm). These values are too low for the rocks to represent primary magma (Baker et al., 1994). They are considered to represent an evolved magma that

underwent various degrees of differentiation, either in a magma chamber or *en route* to surface.

The utilization of a set of discrimination diagrams that used immobile HFSEs and REEs has successfully managed to show the pillow basalts as non-continental basalt. Moreover they show the transitional nature from MORB to IAT of the basalts, a feature of back-arc magmas where magma generation could involve subduction-related materials (Fig. 3-14a and 3-14d). The involvement of subduction-related materials is also suggested from the wide dispersion of data (Fig. 3-14b and 3-14c). This dispersion is indicative of back-arc basin magma and is attributed to the wide range of magmas involved in a subduction influenced igneous regimes.

The low-grade metamorphic assemblage is intensively sheared and folded in a pattern typical of sinistral transpression. The Abutulu shear zone separates two distinct terranes, to the east medium-grade gneisses and migmatites, which are considered as arc-related orthogneiss and supracrustal metasediments and to the west a low-grade metavolcano-sedimentary sequence, interpreted to be a passive margin turbidite and associated massive volcanics. Three phases of deformation- D_3, D_4 and D_5 - are responsible for the development of the Abutulu shear zone.

D_3 is interpreted as a sinistral translation dominant phase that is characterized by the development of a steeply-dipping north to northeast-trending sinistral strike-slip shear zone together with steeply-plunging open to tight folds (F_3). D_3 is suggested to represent the earliest phase of deformation in the relatively young metavolcano-sedimentary sequence, as it folds the S_0 bedding planes along the axis of F_3 folds. D_3 also resulted in

the development of a narrow tectonic melange along the low-grade – medium-grade contact. Planar and linear fabrics related to D_3 were mostly rotated within the course of D_4 which is an east-west directed compression dominant phase. F_4 folds show open to tight asymmetrical geometry and they verge towards the west.

Continuation of the east-west directed shortening associated with a north-south stretching has led to the development of the D_5 conjugate sets of synthetic and antithetic shear zones. D_5 shear zones rotate the previous D_3 and D_4 structure and they locally develop an S_5 planar fabric.

The three phases of deformation D_3, D_4 and D_5 are interpreted to represent oblique collisional structures related to the closing of the newly developed marginal basin, west of the Kabus ophiolitic melange, as will be discused below.

Four occurrences of foliated granitic rocks, identified in the field as late-orogenic granite were found to intrude the medium-grade metamorphic unit. All of the four intrusions were classified as granite and syeno-granite on the Streckeisen and le Maitre (1979) classification diagram. The late-intrusions have the chemistry of high-K calc-alkaline composition. N-MORB normalized incompatible element features are of subduction related affinity.

The four samples define an Nd isochron of 636±75 with a corresponding initial ratio = 0.512029±0.000043 (equivalent to εNd = +4.2). The Sr isochron for the same samples define an age of 595±16 Ma with a corresponding initial ratio SrIR = 0.70325±0.00045. The ε_{Nd636} gave an average of +3.7±0.1. The T_{DM} Nd model ages are not significantly different from those of the Abutulu unit with an average of 792 Ma.

Rims of samples Sk4 (ZR1) and Sk5 (ZR2) define a common mean $^{206}Pb/^{238}U$ ages of approximately 600 Ma, with inherited cores of ~730 Ma, discordance through Pb-loss etc. Because the analyses are discordant, the inherited core age of ~730 Ma is interpreted to represent the age of the source material for the granite and the ~600 Ma rim age is interpreted to represent an age of metamorphism, bearing in mind that some rims and embayments have low Th/U ratios, which could indicate metamorphic growth.

6-2 The geodynamic context:

The Neoproterozoic arc/back-arc metavolcano-sedimentary sequence of the westernmost Nuba Mountains (≈300 km west of Kabus suture) is bounded by medium to high-grade gneiss in both the eastern and western sides. The high-grade gneiss of western Sudan generally reflects Early to Middle Proterozoic crust formation ages with evidence of significant remobilization of older crust (Vail, 1990 and references therein). Sm–Nd T_{DM} model age data from the Wadi Howar (1300 Ma, ε_{Nd} = -6.7; Schandelmeier et al., 1988), from the Nubian Desert (>2200 Ma, ε_{Nd} = -15.8, 1137 Ma, ε_{Nd} = -6.5; Schandelmeier et al., 1988) and from as close to the study area as El Obeid in North Kordofan (>2000 Ma, ε_{Nd} = -10.3; Harris et al., 1984) support this suggestion. Younger K–Ar and Rb–Sr ages were obtained from all of the previously mentioned areas and interpreted to represent a Pan-African imprint (see Vail 1990) for a full compilation of the geochronological data and for the context in which the term ‘‘Pan-African imprint” is used). The younger Rb–Sr age (relative to Sm-Nd age) obtained in this study is also interpreted to represent disturbance of the Rb/Sr system by late Pan-African metamorphism. The metamorphism and/or alteration that affect all the lithologies described in chapter 3 provide evidence supporting open system behavior for the Rb/Sr

system. This mobility in the Rb/Sr system is interpreted as due to younger HT metamorphism at around 600 Ma as suggested for the basement rocks of the Sabaloka area immediately west of the eastern boundary of the SMC in north central Sudan, at around 622 Ma (Küster and Liégeois, 2001 and reference therein). The limited Nd model age data available on the eastern Precambrian outcrops only suggest an early Neoproterozoic age (Harris et al., 1984) for the crust with ε_{Nd750} between +2.2 and +3.5 for the Rashad and Abbasiya outcrops (immediately west of Kabus suture). This is interpreted as suggesting the presence of oceanic material in the crust of central Sudan (Harris et al., 1984).

The model of Abdelsalam and Dawoud (1991) assumes two successive stages of easterly dipping subduction for the development of the northeastern Nuba Mountains metavolcanic rocks and the associated ophiolite. The first resulted in the formation of an intra-oceanic arc (now the metavolcanic sequence of the northeastern Nuba Mountains) and a marginal basin to the west of the arc (now Kabus ophiolite and the metasedimentary rocks of NE Nuba Mountains). The second subduction of the newly formed oceanic crust has led to the formation of the Kabus ophiolitic mélange, as well as an Andean-type arc further west. According to this model, pre-Pan-African crust exists underneath the now eroded Andean-type arc and is separated from the ANS by the Kabus suture.

Unfortunately, there are no isotopic data available on the Pan-African low-grade metavolcanic rocks east of the Kabus suture to assist in correlating the mantle source in the eastern and western Nuba Mountains. However, if we consider the mantle source of the ANS as one entity (although there are some differences in the ε_{Nd} values across the

shield), the isotopic composition of the mantle source of the western Nuba Mountains (average limit ε_{Nd} for 12 metavolcanic rocks ≈ +6 at 778 Ma) is similar to the mantle source reported for the ANS (when considering the errors and uncertainty associated with Sm–Nd data) that is from +6.5 to +8.4 (Stern and Abdelsalam, 1998). According to the model of Abdelsalam and Dawoud (1991), assuming an Andean-type arc west of the Kabus suture, one would expect the geochronological data obtained from the medium-grade gneiss and the granitoid intrusions that intrude the gneiss unit to reflect an isotopic signature that shows contamination with underlying older rocks. The data obtained by Harris et al., (1984) on the syn-tectonic granite of the Rashad and the Abbassyia (recalculated at 976 Ma) (T_{DM} 1000 and 950 Ma and $\varepsilon_{Nd\ 976}$ of +5.1 and +6.1) are in good agreement with the Nd model ages obtained during the course of the current study on six gneisses and syn-orogenic granite and granodiorite samples (see Fig. 5-1 for locations). These indicate $\varepsilon_{Nd\ 976}$ value of +6.2 and a T_{DM} Nd model age of around 948 Ma for crustal formation. The only Paleoproterozoic Nd T_{DM} model age in the area is from El Obeid in North Kordofan (Harris et al., 1984). This age is only estimation, since Harris et al. (1984) found the ratio of Sm^{147}/Nd^{144} to be too high (0.202) to allow for accurate determination of the Nd T_{DM} model age. With the exception of the higher initial Sr ratio (0.7060) at 514 ± 17 Ma of the Jebel Doleibayia outcrop, which is interpreted as the result of assimilation of older crust (Curtis and Lenz, 1985), all the initial Sr ratios obtained by the same authors from the anorogenic granite of Ed Dair and Liri as well as the initial Sr ratio obtained by Harris et al. (1984) on the Syenite of Dumbier suggest either a less depleted mantle source or formation from juvenile crust. Although the number of data are not large enough to systematically cover the

large gneiss unit between the Kabus suture and the Abutulu shear zone, the wide area covered by the samples, the various lithologies of the samples and the tight cluster of the data in both the T_{DM} Nd model ages and the ε_{Nd} would exclude the possibility of a significant contribution of older crust. Based on this assumption we consider the possibility of having older crust between Kabus and Abutulu as highly unlikely, and hence we suggest that the Andean-type arc suggested by Abdelsalam and Dawoud (1991) should be considered instead as an intraoceanic arc, which formed around ~970 Ma.

The six analyzed zoned cores of the late-orogenic granite, sample ZR2 (about 3.95 Km to the southeast (110°) from Um Shara village) have Th/U ranges from slightly high to moderately high values (0.17 – 0.43) indicating a magmatic origin for the cores. Where analysis of both the cores and the rims are available (three grains), the rims (2.3, 5.1 and 8.1) corresponding to the cores (2.2, 5.2 and 8.2) have lower Th/U values (0.04 to 0.08) suggesting metamorphic growth for the rims. The ages of the cores are significantly older than those of the rims where the cores show slight discordance (-3%) and define $^{206}Pb/^{238}U$ ages as old as 743±8 Ma (core 5.2). Younger ages recorded by the cores range from 692±14 Ma to 737±10 Ma. The plot of a U-Pb Concordia of a six zircon cores define an upper intercept age of 723±84 Ma (not presented) with a lower intercept of 591±160 Ma. The 743±8 Ma $^{206}Pb/^{238}U$ age together with the upper intercept age are better interpreted as the age of the early magmatic event, which formed the source of the later magmato-metamorphic event (see later). When the subduction related nature of the granitic material is considered, the earlier identified age is significant in that it defined a lower control on the west dipping subduction event. The

interpretation of the 743±8 Ma $^{206}Pb/^{238}U$ age as age of the source material is supported by the Nd T_{DM} (everage of 4 is 792 Ma) which indicate the presence of slightly older material. The Sm/Nd isochron age of 636±75 Ma is consistent with the concordant (0% discordance) $^{206}Pb/^{238}U$ age of 626±14 of magmatic core 2.2, which is interpreted to represent the age of the latter magmatic event.

With the exception of the syn-orogenic granite, the Rb/Sr whole rock isochron ages of the meta-andesite of the Abutulu unit and the late-orogenic granite have produced six and four point Rb/Sr isochrons of 595±16 Ma and 589.8±13.6 Ma corresponding to SrIR of 0.70325±0.00045 and 0.70376±0.000288 respectively. These ages are only a few million years younger than the ages obtained from U-Pb SHRIMP dating of zircon (a mean $^{206}Pb/^{238}U$ ages of 599.8±5.8 Ma (MSWD = 1.4) for sample ZR1 and a mean $^{207}Pb/^{206}Pb$ age of 607±10 Ma (MSWD = 0.59) for sample ZR2). The younger Rb/Sr age is possibly due to the low closure temperature of the Rb - Sr system (Be'eri-Shlevin et al., 2009). Some of the analyzed rims and embayments show features of metamorphic origin (Th/U < 0.1 together with absence of zoning). This might suggest metamorphic growth for the zircon rims and hence a metamorphic age. However the majority of zircon rims of sample ZR1 and two rims of sample ZR2 (appendixes 5-2a and 5-2b) are of magmatic origin and have similar $^{206}Pb/^{238}U$ and $^{207}Pb/^{206}Pb$ ages to those of metamorphic origin features. This could either indicate that the emplacement of the dated outcrops was contemporaneous with high temperature metamorphism around ≈ 600 Ma or it could only suggest a magmatic event. The latter possibility is supported by a number of recent publications that reported the presence of low Th/U magmatic zircons (Schärer 1984; Sláma et al. 2008). Reasons for such behaviour were provided

by Lopez-Sanchez et al., (2015) (as due to combination of U-rich magma and absence of U-rich accessory minerals) and Küster et al., (2008) (as due to syn-magmatic competition for Th by zircon and other Th-rich accessories such as monazite).

However the interpretation of the ≈ 600 Ma as an age of later magmatic activity does explain the resetting of the Rb/Sr system around the same time that noticed in the meta-andesite of the Abutulu unit (the Abutulu unit has Sm/Nd isochron age of 768±123 and a Rb/Sr age 595±16). For this reason the interpretation of the $^{206}Pb/^{238}U$ ages of 599.8±5.8 age for ZR1 and the mean $^{207}Pb/^{206}Pb$ age of 607±10 age for ZR2 as representing both the ages of intrusion and of metamorphism are favoured in this study. This interpretation is suggested by Küster et al., (2008) for the Banjedid high-K granite of the Sabaloka region of northern Sudan.

Although there is no geochronological data to constrain the age of the initiation of the subduction that formed the proposed intra-oceanic arc, it must have started earlier than the 976 Ma age of the arc magmatism and the syn-orogenic granite. This subduction and then collisional activity is earlier than what is recognized in the northern part of the Nubian Shield where Küster et al., (2008) identified the age of the early Pan-African accretionary phase in the ANS to be between 850 and 650 Ma. The age of the oceanic lithologies in the ANS was found to be between 890 and 690 Ma (Stern et al., 2004).

6-3 Proposed tectonic model:

The initiation of a west-dipping subduction zone to the west of the Kabus ophiolitic mélange (Abdelsalam and Dawoud, 1991) led to the formation of an intra-oceanic arc (Fig. 6-1a) around 976±58 Ma (the age of the felsic arc related magmatism the protolith

of the orthogeniss) as well as the emplacement of volcanic arc granite and gabbro (now the syn-orogenic granitoids) at 982±63 Ma (three point Nd isochron for the syn-orogenic granite).

The co-existence and occasional intercalation between Neoproterozoic arc/back-arc metavolcanic rocks, arc related sedimentary rocks and turbiditie (the Arid assemblage) necessitate the existence of an early Neoproterozoic marginal basin (i.e. before 778 Ma the age of metavolcanic rocks) further west of the intra-oceanic arc. The arc/back-arc signature of the metavolcanic rocks precludes the simple model assuming opening and closing of a small marginal basin without developing subduction zones as has been proposed for the Rahib fold and thrust belt in northwestern Sudan (Abdel-Rahman et al., 1990).

Opening of the marginal basin led to the extrusion of the back-arc volcanism (andesite and basaltic andesite of the Abutulu unit) (Fig. 6-1b) and at a later stage (after the 778 Ma age of back-arc magmatism), the basin started receiving sediments from the western continental side and possibly from the eastern intra-oceanic arc (Fig. 6-1b). Continuous opening of the marginal basin caused the formation of a limited oceanic basin crust (the pillow basalt, massive and layered gabbro of the Arid unit) (Fig. 6-1b). The uncertainty on the ages does not allow for accurate estimation of the timing of arc activity.

The closure of the basin took place sometime after the accumulation of the continental sediments and the continental block to the west collided against the arc/back-arc

assemblage which led to the development of the Abutulu sinistral shear zone (Fig. 6-1c).

Future dating of the Hagar El Tair and Um Shair syntectonic granite intrusions and granodiorite, affected by the sinistral shearing, may set good constraints on the lower age of this collision. Post-collisional tectonism took place probably until around 550 Ma (the age of the alkaline granitoids of Ed Dumbier and Ed Dair) (Harris et al., 1984).

We further suggest that the Neoproterozoic Pan-African crust indeed exists further west of the Kabus suture (at least as far as the Abutulu metavolcanic unit). Also, the Abutulu shear zone may represent a major geological suture separating not only rocks of different lithology, grade of metamorphism and structural style but it also separates terranes of different age and mantle sources.

The Neoproterozoic crust of the western Nuba Mountains can be correlated with that of the Bayuda desert in north central Sudan in terms of age (806 Ma for the Bayuda and 778 Ma for the Nuba Mountains), geochemical affinity (both show an arc-related signature) and structural trends (both show a NE-trend of foliation) and may then support the proposed hypothesis of Küster and Liégeois (2001) that the boundary of the SMC (referred to as the East Saharan ghost craton) must lie below or further west than what was previously expected.

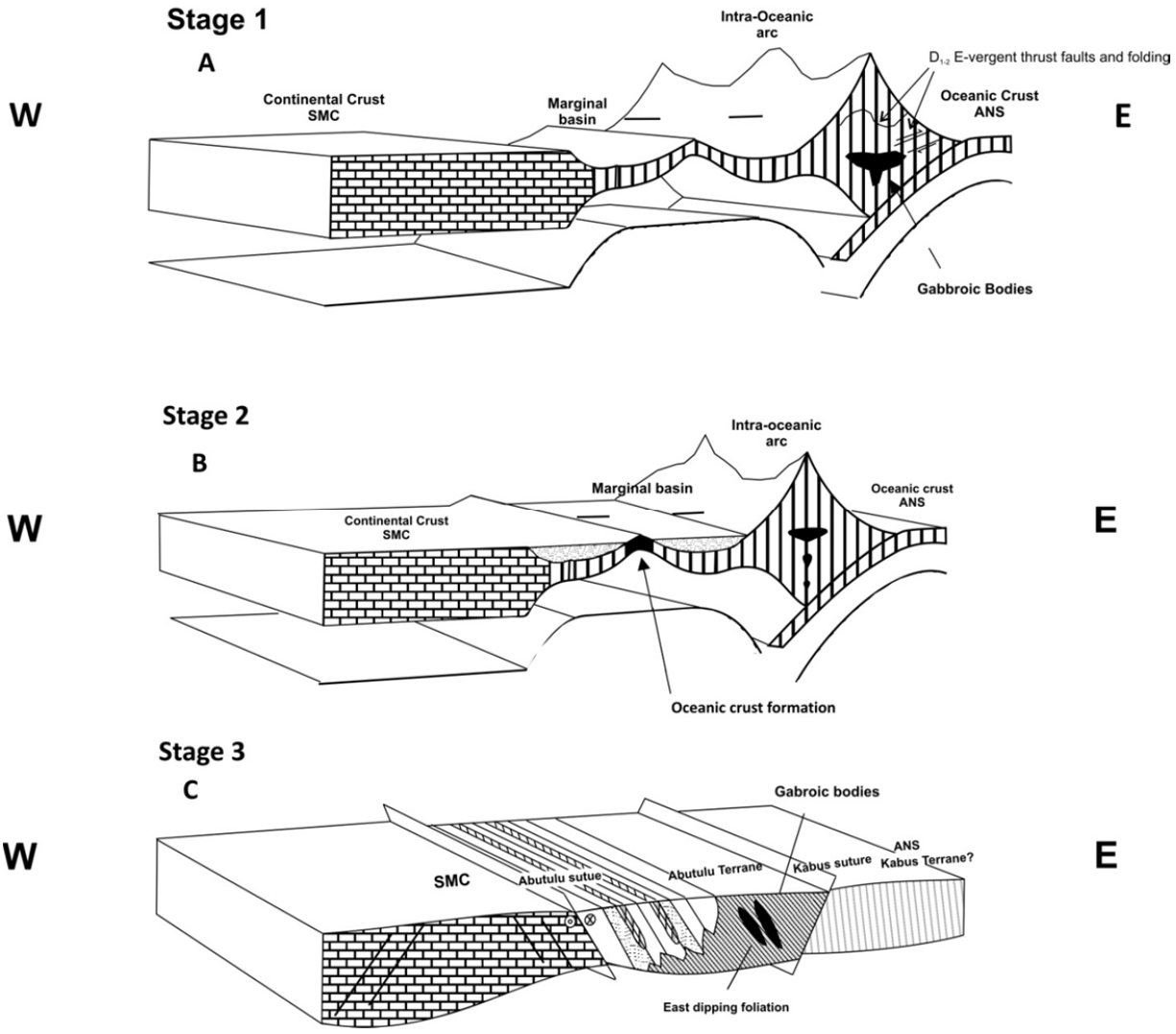

Figure 6-1: Proposed tectonic model for the Nuba Mountains, Sudan. (a) The development of intra-oceanic arc west of the Kabus subduction zone, formation of marginal basin west of the arc and beginning of the collision between the arc and the ANS (b) development of oceanic crust along the marginal basin, formation of passive margin along the continent side and passive margin begin of the receiving of sediments (c) closing of the marginal basin and formation of the Abutulu suture.

6-4 Conclusions:

- Geological mapping of the area between Abu Zabad and Abutulu, southern Sudan, confirms that a low-grade metavolcano-sedimentary sequence (meta-andesite, meta-basalt, slate, graphitic and quartzitic schist) is continuous throughout the area. This sequence is associated with occurrences of mafic and minor ultramafic rocks that show most of the features typical of Penrose conference-type ophiolites.

– The mafic complexes have all of the geochemical characteristics set by Dilek and Furnes (2011) for back-arc supra-subduction ophiolites and hence they are considered to represent remnants of a continental back-arc basin that developed to the west of the Kabus ophiolitic melange.

– On the basis of the variation in lithology, geochemistry, inferred tectonic environment and isotopic characteristics, the low-grade metavolcano-sedimentary sequence and associated supra-crustal back-arc ophiolite are considered to represent a Neoproterozoic arc terrane, the ‘Abutulu terrane’, that extends from Abu Zabad in the north to a few kilometers southwest of Abutulu in the south. These rocks are separated from the medium-grade gneisses in the east by the Abutulu sinistral shear zone. Its western boundary against the pre-Neoproterozoic SMC is hidden under the Quaternary sediments of the Nuba Mountains.

The gneissic unit bounded by the Kabus and the Abutulu sutures, represents orthogneisses and supracrustal metasediments, both having mineral assemblages of amphibolite facies of metamorphism. The unit is intruded by syn-orogenic granite. The geochemistry of both the orthogneiss and synorogenic granite are that of arc-related

magmatism. The orthogneiss is considered to have originated from felsic arc volcanism and synorogenic granite that have features of volcanic arc granite. The ε_{Nd} values of both of the orthogneiss and the synorogenic granite are that of depleted mantle similar to that of the ANS.

The gneiss unit is interpreted as an intra-oceanic arc, developed beneath a westerly dipping subduction zone to the west of the Kabus suture. The Nd isochron age of six gneiss samples and the Nd TDM model ages calculated for each sample suggest an early Neoproterozoic age for the intra-oceanic arc.

– It is possible that the Abutulu Shear Zone represents the eastern edge of the SMC, approximately 300 km further west than was previously thought (Abdelsalam and Dawoud, 1991).

Acknowledgments.

This work has been carried out at the Department of Geology, Faculty of Natural and Agricultural Sciences of the University of Pretoria. The work was sponsored by the Secretary of Academic Affairs, Al Neelain University and the Ministry of Higher Education and Scientific Research of the Republic of Sudan; they are gratefully acknowledged.

My special thanks and gratitude goes to my main supervisor professor Adam Bumby of the University of Pretoria and to my co-supervisor professor Geoffery Grantham of the University of Johannesburg. Their keen supervision and invaluable advice throughout the study are highly regarded.

My appreciations are due to Dr, El Sheikh Abdelrahman, Dr Salih Ali, Dr Mohammed Yahya, Mr Musab El Jah, Mr Waleed Abdel Gabar, Mr Modathar Balaha and Mr Wadah all of Al Neelain University for their support in different aspects of the study.

Special thanks to Professor Pat Eriksson for providing funds for geochemical analysis. Dr Richard Armstrong of the Australian National University helped with the SHRIMP analysis and this is highly appreciated.

The Geological Research Authority of Sudan provided logistical support in two field trips so they are specially thanks. Mr Musab EL Mahi of Greater Nile Petroleum Operating Company is thanks for his support in the last field trip.

The National Research Foundation of the Republic of South Africa is thanked for providing funds for geochronological analysis through professor Adam Bumby.

Finally I would like to thanks my extended and small family for their support and patient during the period of study.

References:

Abdel-Rahman, E.M., Harms, U., Schandelmeier, H., Franz, G., Darbyshire, D.P.F., Horn, P., Muller-Sohnius, D., 1990. A new ophiolite occurrence in NW Sudan—Constraints on late Proterozoic tectonism. Terra Nova 2, 363–376.

Abdel-Rahman, E.M., Matheis, G., Schandelmeier, H., Karfis, M.A., Gadir, I., El Khedir, M., 1993. Evolution of the Keraf back-arc basin: Constraints on the Nubian Shield margin. In: Thorweihe, U., Schandelmeier, H. (Eds.), Geoscientific Research in NE Africa. Balkema, Amsterdam, pp. 93–98.

Abdelsalam, M.G., Dawoud, A.S., 1991. The Kabus ophiolitic melange, Sudan, and its bearing on the W boundary of the Nubian Shield. Journal of the Geololgical Society London 148, 83– 92.

Abdelsalam, M.G., Stern, R.J., Abdel-Rahman, E.M., Elfaki, E.M., Elhur, B., Ibrahim, F.M., 2000. Neoproterozoic deformation in northern Sudan: The third cataract shear zone. Journal of African Earth Sciences 30, 2.

Abdelsalam, M.G., Stern, R.J., Copeland, P., Elfaki, E.M., Elhur, B., Ibrahim, F.M., 1998. The Neoproterozoic Keraf suture in NE Sudan: Sinistral transpression along the eastern margin of West Gondwana. Journal of Geology 106, 133–148.

Abdelsalam, M.G., Stern, R.J., Schandelmeier, H., Sultan, M., 1995. Deformational history of the Keraf Zone in NE Sudan, revealed by Shuttle Imaging Radar. Journal Geology 103, 475–491.

Abdelsalam, M., Liégeois, J.P., Stern, R.J., 2002. The Saharan metacraton. Journal of African Earth Sciences 34, 119–136.

Ali, E.A., Abdel Rahman, E.M., 2010. New ophiolite occurrences in Sudan and constraint on the western boundary of the Nubian Shield: Petrographical and geochemical evidence. Journal of African Earth Sciences 59, 101-110.

Almond, D.C., Ahmed, F., 1987. Ductile shear zones on N Red Sea Hills, Sudan and their implication for crustal collision. Geological Journal 22, 175–184.

Ama Salah, I., Liégeois, J. P., Pouclet, A., 1996. Evolution d'un arc insulaire océanique Birimian précoce au Liptako Nigérien (Sirba): Géologie, géochronologie et géochimie. Journal of African Earth Sciences, 22, 235–254.

Andonaegui, P., Castiñeiras, P., González Cuadra, P., Arenas, R., Sánchez Martínez, S., Abati, J., Díaz García, F., Martínez Catalán, J.R., 2012. The Corredoiras orthogneiss (NW Iberian Massif): geochemistry and geochronology of the Paleozoic magmatic suite developed in a peri-Gondwanan arc. Lithos 128–131:84–99

Anon, 1972. Penrose Conference on Ophiolites, 17. Geotimes, pp. 24–25.

Barth, H., Besang, C., Lenz, H., Meinhold, K.-D., 1983. Results of petrographical investigation and Rb/Sr age determinations on nonorogenic ring complexes in the Bayuda Desert, Sudan. Geologisches Jahrbuch 51, 3–34.

Batchelor, R.A., Bowden, P., 1985. Petrogenetic interpretation of granitiod rock series using multications parameters. Chemical Geolology. 48, 43-55. Amsterdam.

Be'eri-Shlevin, Y., Katzir, Y., Whitehouse, M.J., 2009. Post-collisional tectonomagmatic evolution in the northern Arabian-Nubian Shield: Time constraints from ion-prope U-Pb dating of zircon. Journal of the Geological Society, London. V 166, p. 71-85.

Bennett, H., Oliver, G.J., 1993. XRF analysis of ceramics, minerals and allied materials. Journal of Chemical Education 70 (1), p A25. DOI: 10.1021/ed070pA25.1.

Bertrand, J.-M., Caby, R., 1978. Geodynamic evolution of the Pan-African orogenic belt: A new interpretation of the Hoggar Shield (Algerian Sahara). Geologische Rundschau 67, 357–388.

Best, M.G., 2003. Igneous and metamorphic petrology 2nd edition. Blackwell Science Ltd. Printed in Italy. ISBN 1-40510-588-7.

Black, R., Liégeois, J.-P., 1993. Cratons, mobile belts, alkaline rocks and continental lithospheric mantle: The Pan-African testimony. Journal of the Geological Society, London 150, 89–98.

Brinkmann, K., 1982. Mineral Prospecting in the Northeast Nuba Mountains, Southern Kordofan. Federal Institute for Geosciences and Natural Resources BGR) Report, West Germany, Hannover.

Brinkmann, K., 1986. Geology and mineralization of the basement complex in the northeastern Nuba Mountains, Sudan. Geol. Jahrbuch. 64, 3–34.

Brophy, March, 1985. On the origin of high-alumina arc basalt and the mechanics ofmelt extraction. Journal of Petrology. 27 (4), 763–789.

Browne, S.E., Fairhead, S.D., 1983. Gravity study of the central African rift system: a model for continental disruption, 1. The Ngaoundere and Abu Gabra Rifts. Tectonophysics 94, 187–203.

Cann, J.R., 1970. Rb, Sr, Y, Zr and Nb in some ocean floor basaltic rocks. Earth Planet. Science. Lett. 10, 7–11.

Champion, D.C., 2013. Neodymium depleted mantle model age map of Australia: explanatory notes and user guide. Canberra: Geoscience Australia.

Chappell B.W., 1999. Aluminium saturation in I- and S-type granites and the characterization of fractionated haplogranites. Lithos 46, 535–551

Coleman, R.G., 1977. Ophiolites. Springer-Verlag, Berlin, 229.

Corfu, F., Hanchar, J. M., Hoskin, P. W. O. & Kinny, P. (2003). Atlas of zircon textures. In: Hanchar, J. M. & Hoskin, P. W. O. (eds) Zircon. Reviews in Mineralogy and Geochemistry 53, 469–499.

Coogan, L. A. Wilson, R.N., Gillis, K.M., MacLeod, C.J., 2001. Near-solidus evolution of oceanic gabbros: Insights from amphibole geochemistry, Geochimica et Cosmochimica Acta, 65(23), 4339–4357, doi:10.1016/S0016-7037(01)00714-1.

Curtis, P., Lenz, H., 1985. Geologic and geochronological investigations of selected alkali igneous complexes in the Nuba Mountains, southern Kordofan, Sudan. Geologisches Jahrbuch. 69, 3–24.

Davidson, J.P., 1996. Deciphering mantle and crustal signatures in subduction zone magmatism. Geophysical Monograph., 96, 251–262

Denkler, T., Franz, G., Schandelmeier, H., 1994. Tectonometamorphic evolution of the Neoproterozoic Delgo suture zone, northern Sudan. Geologische Rundschau. 83, 578–590.

DePaolo, D.J., 1981. Neodymium isotopes in the Colorado Front Range and crust – mantle evolution in the Proterozoic. Nature 291, 193–7.

Dilek, Y., Furnes, H., 2011. Ophiolite genesis and global tectonics: geochemical and tectonic fingerprinting of ancient oceanic lithosphere. Geological Society of America Bull. 123, 387–411.

Drury, S.A., 1993. Image interpretation in geolgy.-^{2}nd ed., -283 pp., London (Chapman and Hall).

Eglington, B.M., Harmer, R.E., 1999. Geodate for Windows Version 1: Isotope Regression and Modelling Software. Open File Report 1999–0206 O, Council for Geoscience, Pretoria, pp. 24.

El Ageed, A.I., 1974. The Geology and Iron Mineralization in the Northeast Nuba Mountains. University of Khartoum, Kordofan Province, Sudan, MSc thesis.

El Ageed, A.I., El Rabaa, S.M., 1981. The Geology and Structural Evolution of the Northeastern Nuba Mountains, Southern Kordofan Province, Sudan. vol. 32. Bulletin of the Geological and Mineral Resources Authority of the Sudan.

El Nadi, A.I., 1980. The geology of the Keig El Kheil, Damik and Umm Dugo igneous complexes, Nuba Mountains, Sudan. Univ. Khartoum, M.Sc. thesis, (unpublished).

Fezaa, N., Liégeois, J.P., Abdallah, N., Cherfouh, E.H., De Waele, B., Bruguier, O., Ouabadi, A., 2010. Late Ediacaran geological evolution (575–555 Ma) of the Djanet Terrane, Eastern Hoggar, Algeria, evidence for a Murzukian intracontinental episode. Precambrian Research 180, 299–327.

Floyd, P.A., Kelling, G., Gökçen, S.L., Gökçen, N., 1991. Geochemistry and tectonic environment of basaltic rocks from the Misis Ophiolitic Melange, south Turkey. Chemical Geology 89, 263-280.

Fowler, A., Prokoph, A. & Dupuis, C. (2002). Organization of oscillatory zoning in zircon: analysis, scaling, geochemistry, and model of a zircon from Kipawa, Quebec, Canada. Geochimica et Cosmochimica Acta 66, 311–328.

Frost, B. R., Arculus, R. J., Barnes, C. G., Collins, W. J., Ellis, D. J. & Frost, C. D., 2001. A geochemical classification of granitic rocks. Journal of Petrology 42, 2033-2048.

Gass, I.G., 1981.Pan-African (Upper Proterozoic) plate tectonics of the Arabian-Nubian Shield. In: Kröner (ed.), Precambrian Plate Tectonics, 387-405, Amsterdam (Elsevier).

Gass, I.G., 1990. Ophiolites and oceanic lithosphere. In: Malpas, J., Moores, E.M., Panayiotou, A., Xenophontos, C. (Eds.), Ophiolites, Oceanic Crustal Analogues, Proceedings of the Symposium ‘‘Troodos 1987": Nicosia, Cyprus, The Geological Survey Department, pp. 1–10.

Goldstein, S.L., O'Nions, R.K., Hamilton, P.J., 1984. A Sm–Nd isotopic study of atmospheric dusts and particulates from major river systems. Earth and Planetary Science Letters 70, 221–36.

Hanmer, S., Passchier, C.W., 1991. Shear sense indicators: a review. Geological Survey Canada Pap 90:1–71

Harms, U., Schandelmeier, H., Darbyshire, D.P.F., 1990. Pan-African reworked early/ middle Proterozoic crust in NE Africa W of the Nile: Sr and Nd isotope evidence. Journal of the Geological Society London 147, 859–872.

Harms, U., Darbyshire, D.P.F., Denkler, T., Hengst, M., Schandelmeier, H., 1994. Evolution of the Neoproterozoic Delgo sutures zone and crustal growth in northern Sudan: geochemical and radiogenic isotope constrains. Geologische Rundschau. 83, 591–603.

Harris, N.B.W., Hawkesworth, C.J., Ries, A.C., 1984. Crustal evolution in north-east Sudan and East Africa from model Nd ages. Nature 309, 773–776.

Hart, R., 1970. K, Rb, Cs contents and K/Rb, K/Cs ratios of fresh and altered submarine basalts. Earth and Planetary Science Letters 6, 295–303.

Hashiguchi, H., Yamada, R., Inoue, T., 1983. Practical application of low Na 2 O anomalies in footwall acid lava for delimiting promising areas around the Kosaka and Fukazawa Kuroko deposits, Akita Prefecture, Japan. In: Ohmoto, H. et al. (Eds.), The Kuroko massive sulfide deposite, Economic geology Monograph, vol. 5, pp. 387–394.

Hastie, A.R., Kerr, A.C., Pearce, J.A., Mitchelle, S.F., 2007. Classification of altered volcanic island arc rocks using immobile trace elements: Development of the Th–Co discrimination diagram. Journal of Petrology 48 (12), 2341–2357.

Hill, I.G., Worden, R.H., Meighan, I.G., 2000. Yttrium: The immobility – mobility transition during basaltic weathering. Geology 28, 923–926.

Hine R., Williams I.S., Chapell B.W., & White A.J.R., 1978. Contrasts between I- and S-type granitoids of the Kosciusko Batholith. Journal of the Geological Society of Australia 25, 219–234.

Hirdes, W., Brinkmann, K., 1985. The Kabus and Balula serpentinite and metagabbro complexes: a dismembered ophiolite in northeastern Nuba Mountains, Sudan. Geologisches Jahrbuch. 58, 3–43.

Humphris, S.E., Thompson, G., 1978. Hydrothermal alteration of oceanic basalts by seawater. Geochimica et Cosmochimica Acta 42, 107–125.

Hynes, A., 1980. Carbonitization and mobility of Ti, Y and Zr in Ascot formation metabasalt, S.E. Quebec. Contributions to Mineralogy and Petrology. 75, 79–87.

Irvine, T.N., Baragar, W.R., 1971. Aguide to the chemical classification of the common volcanic rocks. Can. Journal of Earth Science 8, 523–548.

Jensen, R., 1996. Introductory Digital Image Processing: Aremote sensing perspective. 2nd edition.

Kampunzu, A.B., Bonhomme, M.G., Kanika, M., 1998. Geochronology of volcanic rocks and evolution of the Cenozoic Western branch of the East African rift system. Journal of African Earth Sciences 26, 441–461.

Kennedy, W.O., 1964. The Structural differentiation of the Africa in the Pan-African (± 500 m. y.) tectonic episode. Res. Inst. Afr. Ceol., Univ. Leeds, 8th Annu. Rep. 1962–1963, 48–49.

Key, R.M., Charsley, T.J., Hackman, T.J., Wilkinson, A.F., Rundle, C.C., 1989. Superimposed upper Proterozoic collision controlled orogenies in the Mozambique Orogenic belt of Kenya. Precambrian Research 44, 197–225.

Kröner, A., 1977. The Precambrian geotectonic evolution of Africa: plate accretion vs. plate destruction. Precambrian Research 4, 163– 213.

Kröner, A., Stern, R.J., 2004. Pan-African Orogeny. Encyclopedia of Geology, vol. 1. Elsevier, Amsterdam.

Kröner, A., Stern, R.J., Dawoud, A.S., Compston, W., Reischmann, T., 1987. The Pan-African continental margin in NE Africa: evidence from a geochronological study of granulites at Sabaloka, Sudan. Earth Planetary Science Letters 85, 91–104.

Küster, D., Liegeois, J.P., 2001. Sr, Nd isotopes and geochemistry of the Bayuda Desert high-grade metamorphic basement (Sudan): an early Pan-African oceanic convergent margin, not the edge of the East Saharan ghost craton? Precambrian Research 109, 1–23.

Küster, D., Liégeois, J.P., Matukov, D., Sergeev, S., Lucassen, F., 2008. Zircon geochronology and Sr, Nd, Pb isotope geochemistry of granitoids from Bayuda Desert and Sabaloka (Sudan): evidence for a Bayudian event (920–900 Ma) preceding the Pan-African orogenic cycle (860–590 Ma) at the eastern boundary of the Saharan Metacrat. Precambrian Research 164, 16–39.

Liew, T.C., Hofmann, A.W., 1988. Precambrian crustal components, plutonic associations, plate environment of the Hercynian Fold Belt of central Europe: Indications from a Nd and Sr isotopic study. Contributions to Mineralogy and Petrology, *98*, 129-138.

Liégeois, J.-P., Black, R., Navez, J., Latouche, L., 1994. Early and late Pan-African orogenies in the Air assembly of terranes (Tuareg Shield, Niger). Precambrian Research 67, 59–88.

Liégeois, J.P., Abdelsalam, M.G., Ennih, N., Ouabadi, A., 2013. Metacraton: nature, genesis and behavior. Gondwana Research 23 (2013), 220–237.

Lopez-Sanchez, M.A., Aleinikoff, J.N., Francisco, M., Marcos, A., Martínez, J., Llana-Fúnez., S., 2015. An example of low-Th/U zircon overgrowths of magmatic origin in a late orogenic Variscan intrusion: the San Ciprián massif (NW Spain). Journal of the Geological Society. doi:10.1144/jgs2015-071 | Vol. 173 | 2016 | pp. 282–291

Loubser, M., Verryn, S., 2008. Combining XRF and XRD analyses and sample preparation to solve mineralogical problems. South African Journal of Geology, 111, 229 - 238.

Ludwig, K.R., 1999. Using Isoplot/Ex Version 2.01, A Geochronological Toolkit for Microsoft Excel. Berkeley Geochronology Center Special Publication No. 1a, Berkeley, CA, 47 pp.

Luhr, J.F., 1997. Extensional tectonics and diverse primitive volcanic in the western Mexican volcanic belts. Can. Mineral. 35, 473–500.

Lyns, H., Campbell-Smith, W., 1921. Preliminary note on rocks of Darfur. Geological Magazine 58, 206–215.

Manikyamba, C., Sohini Ganguly, M., Santosh, M., Saha, Abhishek., Lakshminarayana, G., 2015. Geochemistry and petrogenesis of Rajahmundry trap basalts of Krishna-Godavari Basin, India. Geosci. Front. 6 (2015), 437–451.

Mansour, A.O., Iskander, W., 1960. An Iron Ore Deposit at Jebel Abutulu. Geological Survey, Sudan. Bull. 6.

Mansour, A.O., Samuel, A., 1957. Geology and Hydrogeology of Sheet 66-A Rashad and Sheet 66-E Talodi. Geological Survey, Sudan. Mem. 1.

McCulloch, M.T., Gamble, J.A., 1991. Geochemical and geodynamical constraints on subduction zone magmatism. Earth and Planetary Science Letters 102, 358–374.

Meinhold, K.-D., 1979. The Precambrian basement complex of Bayuda Desert, northern Sudan. Review Geology, Geography Physics 21, 359–401.

Míková, J., Denková, P., 2007. Modified chromatographic separation scheme for Sr and Nd isotope analysis in geological silicate samples. Journal of GEOsciences 52, 221–226. http://dx.doi.org/10.3190/jgeosci.015.

Moores, E.M., Vine, F.J., 1971. The Troodos massif, Cyprus, and other ophiolites as oceanic crust: evaluation and implications. Philosophical Transactions of the Royal Society of London 268A, 443–466.

Mottl, M.J., 1983. Metabasalts, axial hot springs, and the structure of hydrothermal systems at mid-ocean ridges. Geological Society of America Bull. 94, 161–180.

Nelson, B.K., DePaolo, D.J., 1985. Rapid production of continental crust 1.7 to 1.9 b.y. ago: Nd isotopic evidence from the basement of the North American midcontinent. Geological Society of America Bull. 96, 746–754.

O'Conner, J.T., 1965. A classification for quartz-rich igneous rock based on feldspar ratios. U.S Geological survey. Prof. Paper 525B, B79-B84.

Passchier, C.W, Simpson C., 1986. Porphyroclast systems as kinematic indicators. Journal of Structural Geology 8:831–844

Pearce, J.A., 1996. A users guide to basalt discrimination diagrams. In: Wyman, D.A. (Ed.), Trace Element Geochemistry of Volcanic Rocks: Applications for Massive Sulphide Exploration, vol. 12. Geological Association of Canada, Short Course Notes, pp. 79–113.

Pearce, J.A., 2008. Geochemical fingerprinting of oceanic basalts with applications to ophiolite classification and the search for Archean oceanic crust. Lithos 100, 14– 48.

Pearce, J.A., Cann, J.R., 1973. Tectonic setting of basic volcanic rocks determined using trace element analyses. Earth and Planetary Science Letters19, 290–300.

Pearce, J.A, Stern, R.J., 2006. Origin of Back-Arc Basin Magmas: Trace Element and Isotope Perspectives. Back-Arc Spreading Systems: Geological, Biological, Chemical and Physical Interactions. Geophysical Monograph Series 166 Published in 2006 by the American Geophysical Union 10.1029/166GM06.

Pearce J.A., Harris N.B.W., Tindle A.G., 1984. Trace element discrimination diagrams for the tectonic interpretation of granitic rocks. Journal of Petrology. 25:956-983.

Pearce, J.A., Baker, P.E., Harvey, P.K., Luff, I.W., 1995. Geochemical evidence for subduction fluxes, mantle melting and fractional crystallization beneath the south Sandwich island arc. Journal of Petrology 36, 1073–1109.

Peate, D.W., Pearce, J.A., Hawkesworth, C.J., Colley, H., Edwards, C.M.H., Hirose, K., 1997. Geochemical variations in Vanuatu arc lavas: the role of subducted material and a variable mantle wedge composition. Journal of Petrology 38, 1331–1358.

Pin, C., Zalduegui, J.F.S., 1997. Sequential separation of light rare-earth elements, thorium and uranium by miniaturized extraction chromatography: application to isotopic analyses of silicate rocks. Analytica Chimica Acta339, 79–89.

Pin, C., Briot, D., Bassin, C., Poitrasson, F., 1994. Concominant Separation of strontium and samarium–neodymium for isotopic analysis in silicate samples, based on specific extraction chromatography. Analytica Chimica Acta 298, 209–217.

Plank, T., 2005. Constraints from Thorium/Lanthanum on sediment recycling at subduction zones and the evolution of the continents. Journal of Petrology 46, 921–944.

Polat, A., Kerrich, R., Wyman, D., 1999. Geochemical diversity in oceanic komatiites and basalts from the late Archean Wawa greenstone belt, Superior Province, Canada: trace element and Nd isotope evidence for a heterogeneous mantle. Precam. Res. 94, 139–173.

Preccerillo, A., Taylor, S.R., 1976. Geochemistry of calc-alkaline volcanic rocks from the Kastamonu area, Turkey. Contributions to Mineralogy and Petrology. 58, 63–81.

Robinson, P.T., Malpas, J., Dilek, Y., Zhou, M.F., 2008. The significance of sheeted dike complexes in ophiolites. Geological Society of America Today 18 (11), 4–10.

Rocci, G., 1965. Essai d'interpretation de mesures geochronologiques. La structure de l'Ouest africain. Sciences Terre Nancy 10, 461–479.

Rollinson, Hugh R., 1993. Using Geochemical Data: Evaluation, Presentation, Interpretation. Longman Geochemistry Series, Harlow, England.

Rubatto, D., Gebauer, D., 2000. Use of cathodoluminescence for U– Pb zircon dating by ion microprobe: some examples from the Western Alps. In: Pagel, M., Barbi, V., Blanc, P., Ohnenstetter, D. (Eds.), Cathodoluminescence in geosciences. Springer, Berlin Heidelberg New York, pp. 373–400.

Sabins, F. F., 1996. Remote sensing: Principles and interpretation. 3rd edition.

Sadig, A.A., Vail, J.R., 1986. Geology and regional gravity traverses of the Nuba Mountains, Kordofan Province, Sudan. J. African Earth Sciences 5, 329–338.

Saunders, A.D. and Tarney, J., 1979. The geochemistry of basalts from a back-arc spreading centre in the East Scotia Sea. Geochima Acta, 43, 555-72.

Schandelmeier, H., Richter, A., Harms, U., 1987. Proterozoic deformation of the East Sahara Craton in southeast Libya, south Egypt and north Sudan. Tectonophysics 140, 233–246.

Schandelmeier, H., Darbyshire, D.P.F., Harms, U., Richter, A., 1988. The E Saharan craton: Evidence for pre-Pan-African crust in NE Africa W of the Nile. In: El Gaby, S., Greiling, R.O. (Eds.), The Pan-African Belts of NE Africa and Adjacent Areas: Wiesbaden. Friedr Vieweg and Sohn, pp. 69–94.

Schandelmeier, H., Richer, A., Harms, U., Abdel-Rahman, E.M., 1990. Lithology and structure of the late Proterozoic Jebel Rahib fold-and-thrust belt (SW Sudan). Berliner Geowissen Abher (A) 120 (1), 15–30.

Schärer, U. 1984. The effect of initial 230 Th disequilibrium on young U–Pb ages: The Makalu case, Himalaya. Earth and Planetary Science Letters, 67, 191–204, http://dx.doi.org/10.1016/0012-821X(84)90114-6.

Shackleton, R.M., 1979. Precambrian tectonics of Northeast Africa. In: Tahon, S.A., (Eds.), Evolution and mineralization of the Arabian-Nubian Shield, Proceed. Symp., 2, 1-6, Oxford (Pergamon Press).

Shaddad, M.Z., Kropachev, S.M., Khalil, B.E., 1979. Regional geological setting of the Nuba Mountains. Geological Survey Egypt Ann. Rep. 9, 446–454.

Shervais, J.W., 1982. Ti-V plots and the petrogenesis of modern and ophiolitic lavas. Earth and Planetary Science Letters. V. 59. p, 101 – 118.

Shkol'nik, S.I., Reznitskii, L.Z., Belichenko, V.G., Barash, I.G., 2009. Geochemistry, petrogenesis, and geodynamic typification of metavolcanics of the Tunka terrane (Baikal–Hövsgöl region). Russian Geology and Geophysics. 50 (2009), 779– 788.

Sláma, J., Kosler, J. et al. 2008. Plesovice zircon—A new natural reference material for U–Pb and Hf isotopic microanalysis. Chemical Geology, 249, 1–35, http://dx.doi.org/10.1016/j.chemgeo.2007.11.005.

Steiner, L., 1987. The Nuba ophiolite and its geologic setting. In: Matheis, G., Schandelmeier (Eds.), Current research in African Earth science, Extended Abstracts, 14th Colloquium of African Geology, Berlin West, pp. 101–104.

Stern, R.J., 2002. Crustal evolution in the East African Orogen: a neodymium isotopic persprective. Journal of African Earth Sciences 34, 109-117.

Stern, R.J., Abdelsalam, M.G., 1998. Formation of Juvenile Continental Crust in the Arabian-Nubian shield: evidence from Granitic rocks of the Nakasib Suture, NE Sudan. Geologische Rundschau 87, 150–160.

Stern, R.J., Dawoud, A.S., 1991. Late Precambrian (740 Ma) charnockite, enderbite, and granite from Jebel Moya, Sudan: a link between the Mozambique Belt and the Arabian-Nubian Shield? Journal of Geology 99, 648–659.

Stern, R.J., Kröner, A., Reischmann, T., Bender, R., Dawoud, A.S., 1994. Precambrian basement around Wadi Halfa: a new perspective on the evolution of the Central Saharan Ghost craton. Geologische Rundschau 83, 564–577.

Stern, R.J., Johnson, P.R., Kröner, A., Yibas, B., 2004. Neoproterozoic Ophiolites of the Arabian-Nubian Shield. In: Kusky, T., Kusky, T. (Eds.), Precambrian Ophiolites and Related Rocks, Developments in Precambrian Geology, vol. 13, pp. 95–128. http://dx.doi.org/10.1016/S0166-2635(04)13003-X.

Streckeisen, A.L., LeMaitre, R.W., 1979. Chemical approximation to modal QAPF classification of the igneous rocks. Neus Jahrbuch fur Mineralogie, 136, 169-206.

Sultan, M., Bickford, M.E., El Kaliouby, B., Arvidson, R.E., 1992. Common Pb systematics of Precambrian granitic rocks of the Nubian Shield (Egypt) and tectonic implications. Geological Society America Bulletin 104, 456–470.

Sultan, M., Chamberlin, K.R., Bowring, S.A., Arvidson, R.E., Abuzied, H., Al Kaliouby, B., 1990. Geochronologic and isotopic evidence for involvement of pre-Pan-African crust in the Nubian Shield, Egypt. Geology 18, 761–764.

Sultan, M., Tucker, R.D., El Alfy, Z., Attia, R., Ragab, A.G., 1994. U–Pb (zircon) ages for the gneissic terrane west of the Nile, southern Egypt. Geologische Rundschau 83, 514–522.

Sun, S.S., Mc Donough, W.F., 1989. Chemical and isotopic systematics of oceanic basalts: implications for mantle composition and processes. Geological Society,

London, tectonic fingerprinting of ancient oceanic lithosphere. Geological Society America Bull. 123 (3/4), 387–411.

Tatsumi, Y., Eggins, S., 1995, Subduction zone magmatism: Boston, Blackwell Science, 211 p.

Tollstrup, D.L., Gill, J.B., 2005. Hafnium systematics of the Mariana arc: evidence for sediment melt and residual phases. Geology 33 (9), 737–740.

Toteu, S.F., Michard, A., Bertrand, J.M., Rocci, G., 1987. U/Pb dating of Precambrian rocks from the northern Cameroon, orogenic evolution and chronology of the Pan-African belt of central Africa. Precambrian Research 37, 71–87.

Vail, J.R., 1971. Geological reconnaissance in part of Berber District, Northern Province, Sudan: Sudan Geological Survey Deptartment Bull. 18, 76.

Vail, J.R., 1972. Geological reconnaissance in the Zalingei and Jebel Marra areas of western Darfur Province. Sudan Geological Survey Department Bulletin 14, 50 p.

Vail, J.R., 1973. Outline of the Geology of the Nuba Mountains and Vicinity Southern Kordofan Province, Sudan, vol. 23. Bulletin of the Geological and Mineral Resources Authority of the Sudan.

Vail, J.R., 1976. Outline of the geochronology and tectonic units of the basement complex of Northeast Africa. Proceedings Royal Society, London A 350, 127–141.

Vail, J.R., 1983. Pan-African crustal accretion in northeast African. J. African Earth Sciences 1, 285–294.

Vail, J.R., 1985. Pan-African (late Precambrian) tectonic terranes and reconstruction of the Arabian-Nubian Shield. Geology 13, 839–842.

Vail, J.R., 1988. Tectonics and evolution of the Proterozoic basement of NE Africa. In: El Gaby, S., Greiling, R.O. (Eds.), The Pan- African belts of NE Africa and Adjacent areas. Friedr Vieweg and Sohn, pp. 185–226.

Vail, J.R., 1990. Geochronology of the Sudan. Overseas Geology and Mineral Resources, vol. 66.

Watson, J.S., 1996. Fast, simple method of powder pellet preparation for X-Ray fluorescence analysis. X-Ray spectrometry, 25, 173-174.

Weis, D., Kieffer, B., Maerschalk, C., Barling, J., de Jong, J., Williams, G.A., Hanano, D., Pretorius, W., Mattielli, N., Scoates, J.S., Goolaerts, A., Friedman, R.M., Mahoney, J.B., 2006. High-precision isotopic characterization of USGS reference materials by TIMS and MC-ICP-MS. Geochemistry, Geophysics, Geosystems 7, Q0800.

Whalen J.B., Currie K.L., Chappell B.W., 1987. A-type granites: geochemical characteristics, discrimination and petrogenesis. Contributions to Mineralogy and Petrology. 95:407-419

Wilson, M., 1989. Igneous Petrogenesis: A Global Tectonic Approach. Unwin Hyman, London, 466p.

Winchester, J.A., Floyd, P.A., 1977. Geochemical discrimination of different magma series and their differentiation products using immobile elements. Chem. Geol. 20, 325–343.

Wolf, R.E., 2005. What is ICP-MS? …and more importantly, what can it do? https://crustal.usgs.gov/laboratories/icpms/What_is_ICPMS.pdf Ruth E. Wolf Ph.D., Research Chemist, USGS/CR/CICT, March 2005:

Wolf, M.B., London, D., 1994. Apatite dissolution into peraluminous haplogranitic melts: an experimental study of solubilities and mechanisms. Geochimica et Cosmochimica Acta 58, 4127–4145.

Appendix 1-1 Methodology:

1-1-1 Photogeology and digital image processing:

The pre-fieldwork phase started with the preparation, enhancement and interpretation of Landsat images for the purpose of rock type discrimination and delineation of structures. The data used for digital image processing was Landsat 7 Enhanced Thematic Mapper Plus (ETM+) images with 8 visible (reflected light) bands with 30 m resolution (bands 1-5, 7), a thermal infrared channel with 60 m spatial resolution (band 6) and a panchromatic band with 15 m spatial resolution (band 8) and Landsat 8 images with eleven bands; bands 1 - 4 sense visible light, band 5 are near infrared band (NIR), bands 6 and 7 are shortwave infrared (SWIR), band 8 is the panchromatic, band 9 measures a very narrow slice of the electromagnetic spectrum (only 1370 ± 10 nanometers) and bands 10 and 11 are thermal infrared (TIR). All of the bands have spatial resolution of 30 m except band 8 which is 15 m and bands 10 and 11 which are 100m.

Several techniques were implemented in order to enhance the Landsat 8 sub scene to a level that was useful for mapping purposes.

A color composite technique: To produce a color composite image any three bands of the multi spectral bands can be combined together to produce an image. There are various methods to assist in selecting the proper band combination (Drury, 1993 and Jensen, 1996). In this study a combination of bands (7, 6, and 4) set in the RGB positions respectively were chosen to produce a false color composite image (Fig. 1-4) on the basis of testing various bands combination and selecting the one with the best ability to discriminate between the various rock units.

Contrast enhancement: this is one of the image processing techniques that aims to improve obscured object data to a more visible status to the interpreter. Contrast stretching enhancement expands the original bright values of an image to the full range of the grey values (0 – 255) (Sabins, 1996).

Among the different types of contrast stretching enhancement, a linear stretching type is used in this study resulting in a more informative image (Fig. 1-5).

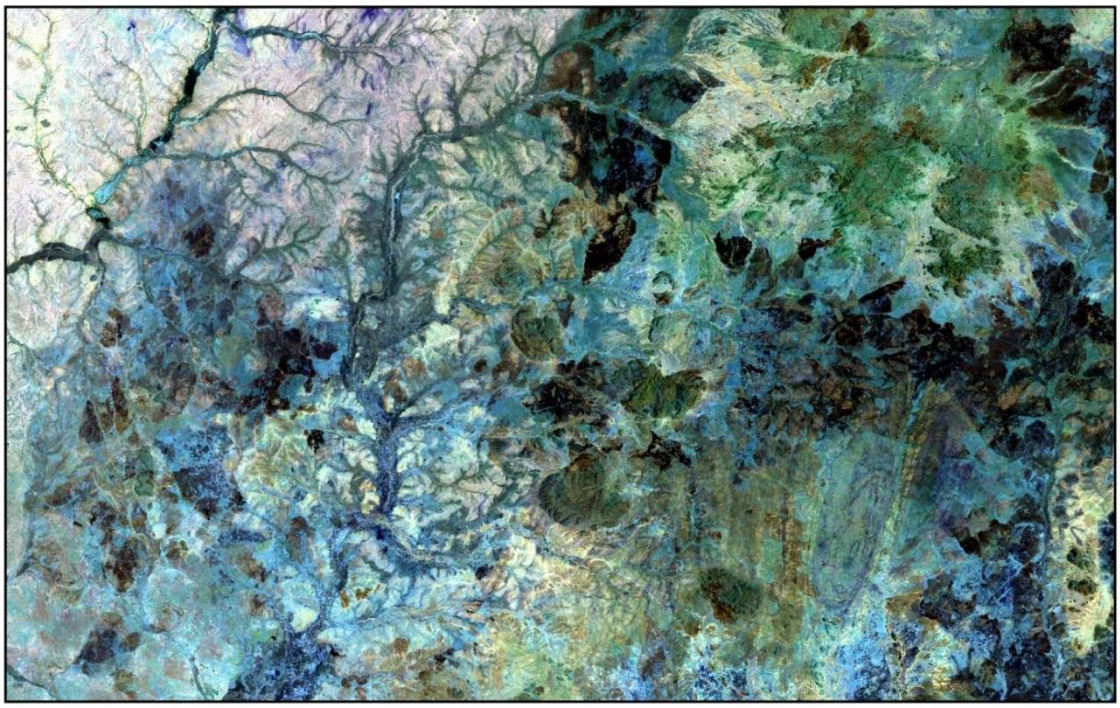

Figure 1-4: Color composite image of bands 7, 6 and 4 for the study area.

HSV Sharpening: is one of the processes that enables the generation of a high-resolution Landsat color images by merging a high-spatial resolution panchromatic band and low-spatial resolution multispectral bands. Transformation of the RGB (Red, Green and Blue) into HSV (Hue, Saturation and Value) color space will replace the value band with the high-resolution band and will automatically resample the hue and saturation bands to the high-resolution pixel size, via one of the convolution techniques. Then the image will be transformed back into RGB color space. The

Landsat 8 image of the study area benefited from the 15m resolution of the panchromatic (band 8) and the color composite image of bands 7, 5 and 1.

Saturation stretching: to produce a more color-saturated image, the original 3 band color image was transformed from RGB space to HSV space. The application of a Gaussian stretch allows the use of the entire saturation range. Finally the HSV data is transformed back into RGB space. The greater range of color tones in the output image (Fig. 1-6) helps more in lithological discrimination.

1-1-2 Field Methods: Four field visits were conducted between 2011 and 2015 with 40 days spent on the field. One regional traverse was carried out to link the eastern and the western part of the Nuba Mountains (Fig. 1-2). The major lithological units of the study area were examined through three major traverses of approximately 100 km length (Fig. 1-2) and more detail regarding each unit was obtained along shorter traverses. Planning and execution of these traverses was aided by the use of Touratech QV navigation software and various Landsat images. The Bahr-alarab sheet of the Robertson Research International, 1988 maps with scale of 1:100000 were also used for navigation (after being geo-referenced).

1-1-3 Microscopic Analysis:

Over two hundred thin-sections of the different lithologies in the Nuba Mountains were partly prepared at the laboratories of the Faculty of Petroleum and Minerals of Al Neelain University and partly at the Geological Research Authority of Sudan (GRAS). Microscopic examination were subsequently carried out at the Petrography Lab of the Geology Department of the University of Pretoria to work out the mineral composition, textural and microstructural characteristics, degree of alteration and metamorphism and to select representative samples for further chemical analysis.

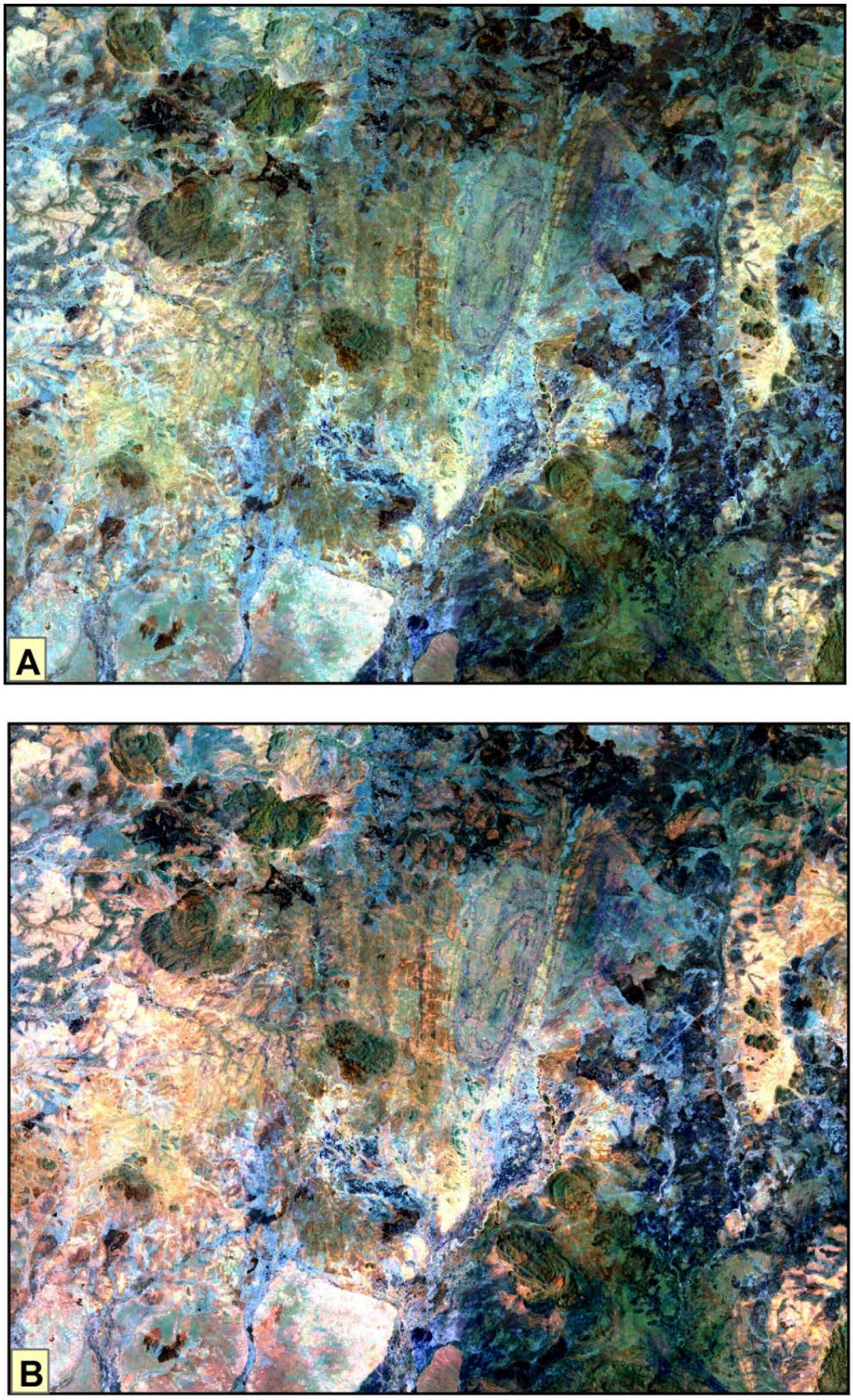

Figure 1-5: Comparison between (A) unstretched and (B) stretched color composite image of bands 7, 6 and 4 in RGB using linear contrast enhancement.

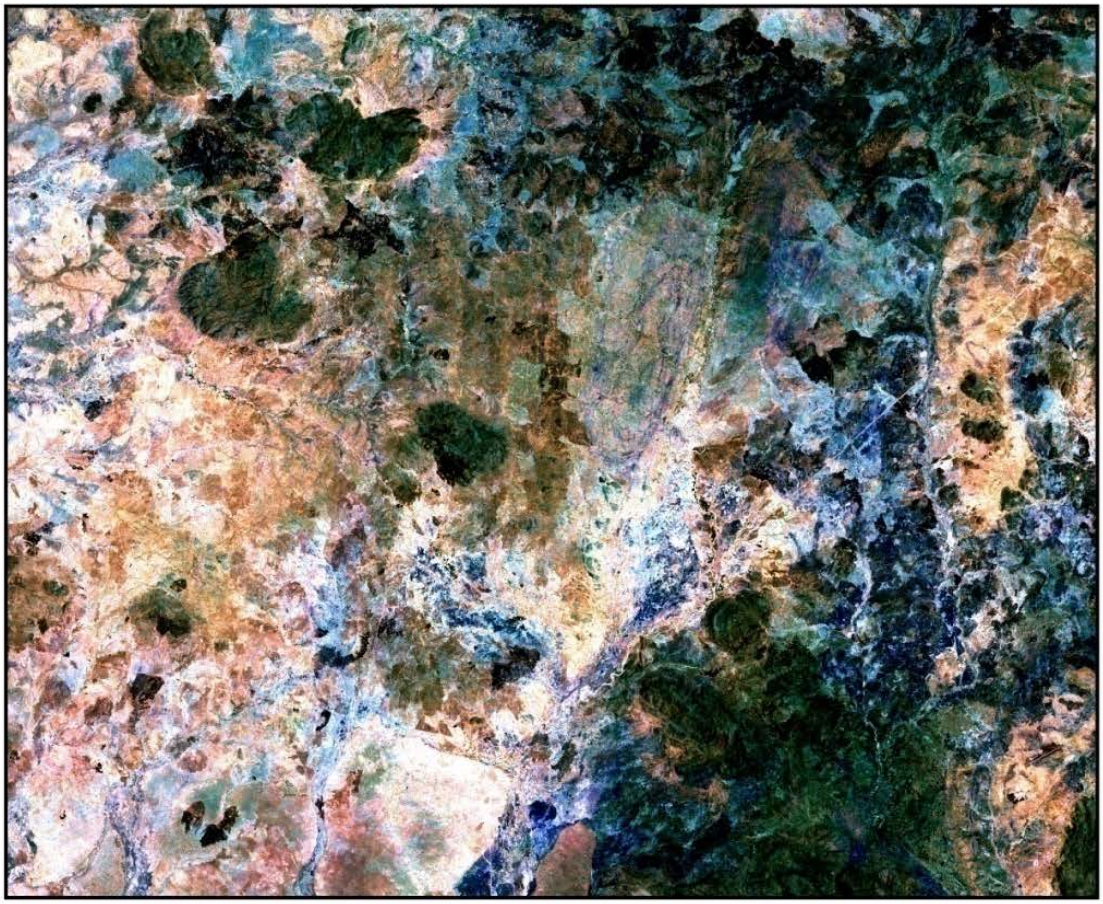

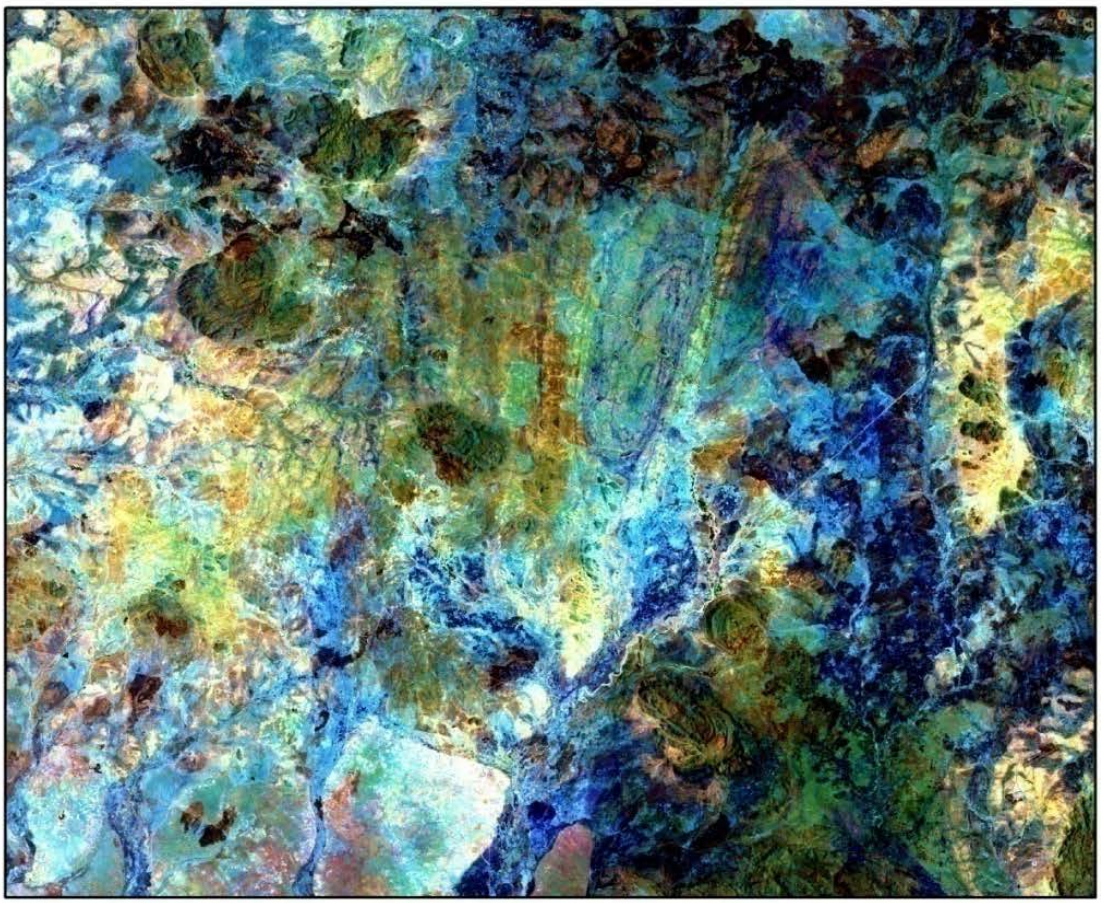

Figure 1-6: (A) color composite image of Landsat 8 converted to high spatial resolution image using hue, saturation and value technique (B) Landsat 8 bands 7, 6 and 4 saturation stretched image

1-1-4 Geochemical Analysis:

Various chemical analytical techniques were conducted on the selected samples during this work in order to determine their chemical composition. Depending on the nature of each analytical technique a certain treatment must be applied to the powdered sample.

1-1-4-1 Sample preparation: the rocks were prepared for the analysis as follows:

1- Fresh samples were selected and the weathering crust was removed.
2- The samples were split into two halves and then one half was crushed with a mechanical jaw-crusher.
3- A portion of the crushed material was ground in a Tungsten Carbide milling vessel to ca. 80% below 75 µm and then stored in plastic bags for further analysis.
4- An amount of the rock powder was heated at 1000°C to determine the loss on ignition (LOI) due to expulsion of the chemically bound volatiles by subtracting the weight of the sample after heating from the weight before heating.
5- For ICP-MS analysis a 500 mg of the sample powder was dissolved in a mixture of concentrated hydrofluoric acid (HF) and perochloric acid ($HClO_4$) at the laboratories of the Geological Science Department of the University of Cape Town and heated to dryness. After cooling, $HClO_4$ diluted with distilled water was added to form a clear solution. In the case of samples rich in ores and organic materials it was necessary to add conc. nitric acid (HNO_3).
6- For XRF analysis the major elements were measured on a fused bead following the method of Bennett and Olivers (1992) listed in Loubser and Verryn (2008). In this method 1g of powder (after heated for LOI) and 6g of

lithium tetraborate ($Li_2B_4O_7$) were mixed in a 5% Au/Pt crucible and fused at 1000C° in a muffle furnace automated fluxer.

7- Trace elements were measured by XRF on pressed pellets using the method of Watson (1996). 20g of powder mixed with few drops of polyvinyl alcohol 40-88 (binder) in a zip-lock plastic bag and then pressed under 20 ton/cm^2 in a collapsible aluminum holder for 2 minutes and then heated at 110 °C until dry.

1-1-4-2 Analytical techniques:

1-1-4-2-1 X-Ray Fluorescence (XRF): is the most widely used analytical method in determination of major and trace elements of rock samples (Rollinson, 1995). The technique is capable of analyzing large groups of elements of different concentrations (up to 80 elements) in a short space of time and with reasonable accuracy. The technique is based on the irradiation of a sample by X-ray beam which will excite secondary X-rays (X-ray fluorescence) that have wavelength characteristics of the elements occurring in the sample. The concentrations of the various elements under investigations are a function of the intensities of the secondary X-rays by reference to a calibrated standard.

For major and trace elements analysis, fused beads and pressed pellets of rock samples were prepared as described in the previous section. The major limitation of the XRF technique is the inability to analyze elements smaller than Na (atomic number = 11) as well as inability to analyze certain trace elements eg. most of the REE.

The instrumentation, the data reduction software and methods and the calibration references used at the laboratories of the University of Pretoria are detailed in Loubser and Verryn (2008).

1-1-4-2-2 Inductively Coupled Plasma Mass Spectrometry (ICP-MS): is an analytical technique that is capable of analyzing most of the elements in the periodic table with a low-detection limit with good precision.

The principal of the technique is to convert the atoms of the elements in the sample into ions through a high temperature source (inductively coupled plasma) and then these ions will be separated and detected by a mass spectrometer. The ICP source is a flow of argon atoms heated by the inductive heat of a radio frequency coil. The temperature of the plasma is about 6000 to 10000°K.

When the sample is introduced to the argon plasma as an aerosol, the high temperature dissociates the chemical bonds of the sample and the elements in the aerosol converted into gaseous atoms and then into ions. These ions are then entered into the mass spectrometer which separates them according to their “mass-to-charge” ratios through various types of filters (e.g. quadrupole mass filter). When the ions are separated according to their “mass-to-charge” they are then detected and counted by a suitable detector which translates the number of ions striking the detector into an electrical signal that can be measured and related to the number of atoms of that element in the sample via the use of calibration standards (Wolf, 2005).

	Gneiss and Syn-orogenic granite																	Late-orogenic granite			
Sample	**230**	**231**	**232**	**233**	**234**	**235**	**236**	**237**	**273**	**272**	**24**	**25**	**25A**	**27**	**91**	**93**		**224**	**275**	**4**	**5**
SiO2	74.1	64.87	64.24	72.18	75.24	76.78	75	75.06	74.88	71.86	74.14	76.34	74.83	70.91	73.12	74.19		74.11	71.78	72.61	70.24
TiO2	0.15	1.24	1.32	0.34	0.17	0.08	0.11	0.03	0.08	0.44	0.08	0.16	0.18	0.38	0.25	0.15		0.16	0.22	0.27	0.29
Al2O3	13.98	15.29	15.81	14.3	13.64	12.67	14.13	13.74	14.17	14.18	14.08	12.86	12.89	14.17	13.37	12.71		14.42	14.65	14.3	15.62
Fe2O3T	1.15	5.12	5.43	2.49	1.59	1.47	1.08	0.63	0.67	2.43	0.84	1.58	1.89	3.06	2.37	2.05		1.05	1.2	1.89	1.99
MnO	0.03	0.06	0.06	0.04	0.01	0.02	0.02	0.08	0.01	0.05	0.01	0.03	0.01	0.06	0.02	0.03		0.02	0.02	0.04	0.02
MgO	0.08	1.12	1.31	0.26	0.02	0.01	0.01	0.01	0.01	0.24	0.01	0.01	0.1	0.17	0.25	0.01		0.07	0.15	0.08	0.13
CaO	0.75	2.62	2.47	0.31	0	0	0.43	0.1	0.7	0.66	0.65	0.85	0.99	1.79	1.03	0.73		0.34	0.43	1.09	1.32
Na2O	3.84	3.58	3.73	3.33	3.13	4.06	3.88	4.22	4.08	2.86	4.16	3.29	3.38	3.01	2.86	4.2		3.51	3.91	3.12	4.1
K2O	4.69	4.83	4.53	5.49	5.6	4.57	4.68	4.3	4.47	6.36	5.59	4.39	5.18	5.56	5.5	5.47		5.8	5.24	5.97	5.78
P2O5	0.02	0.35	0.49	0.08	0.02	0.02	0.01	0	0.02	0.05	0	0	0.04	0.1	0	0.04		0.02	0.04	0	0.08
LOI	0.49	0.68	0.68	0.61	0.74	0.14	0.42	0.45	0.29	0.58	0.41	0.4	0.44	0.22	1.09	0.35		0.5	0.63	0.32	0.21
Total	99.28	99.75	100.06	99.43	100.17	99.81	99.77	98.62	99.38	99.72	99.96	99.89	99.94	99.43	99.85	99.93		100	98.28	99.7	99.76
Ba	1002.9	2382.0	2512.5	932.9	403.7	58.2	902.0	83.7	355.7	850.1	298.3	245.7	243.9	740.9	701.5	268.4		1015.0	1398.0	1113.0	1520.0
Rb	139.3	157.1	152.6	195.7	193.1	106.7	78.6	250.9	171.4	156.0	169.0	171.2	169.5	194.7	77.9	119.3		144.3	89.3	165.3	112.8
Sr	186.5	588.8	552.5	122.6	75.5	15.1	157.6	90.5	145.8	555.1	112.3	69.8	69.9	296.6	58.9	39.6		273.0	462.0	170.1	337.8
Y	3.0	30.0	29.6	23.4	22.0	60.4	5.3	45.4	5.7	44.6	10.9	23.3	20.3	12.6	25.8	52.8		3.7	3.7	9.8	6.5
Zr	89.7	688.1	893.0	267.6	179.7	167.8	99.3	35.6	59.3	534.3	69.7	143.2	181.0	173.2	207.6	302.7		129.5	165.5	219.7	264.1
Nb	6.7	16.2	18.4	13.3	13.8	18.6	4.1	14.5	4.4	24.9	8.5	10.4	10.3	8.1	5.1	12.3		3.8	1.7	7.5	3.6
Th	3.0	33.0	37.7	39.5	40.6	18.5	3.0	11.7	15.4	85.1	13.8	43.2	33.8	23.1	15.3	18.2		11.0	12.1	17.3	20.7
Pb	32.9	27.4	16.9	23.7	28.3	20.0	20.1	54.8	47.8	41.9	50.8	21.0	20.7	37.0	8.2	17.7		31.9	25.3	33.6	27.3
Zn	58.7	152.7	157.4	78.4	35.1	88.6	65.9	21.7	65.7	54.0	144.7	51.7	51.9	82.7	42.8	46.4		64.3	38.4	115.6	76.9
Cu	2.0	13.2	6.5	4.6	19.5	2.2	2.9	1.1	1.7	5.5	2.2	4.7	5.2	7.6	23.5	3.3		1.5	2.4	3.2	3.4
Ni	3.0	65.2	3.0	5.9	9.0	13.9	3.0	4.5	4.8	25.5	16.2	5.0	4.8	11.8	13.9	35.7		12.8	16.7	14.2	25.0
V	16.8	52.8	68.7	18.3	10.2	3.3	16.8	2.2	2.2	14.9	1.9	8.1	8.3	15.9	16.8	6.0		5.1	12.5	9.9	9.9
Cr	106.2	37.7	33.1	6.8	55.6	29.3	103.5	3.3	1.7	5.8	24.6	20.4	24.9	17.4	13.0	38.9		3.5	67.2	41.8	21.8
Hf		15.8			6.5	6.3		2.4	2.3	12.4	2.9	5.2	6.6	4.8		10.1		3.8	4.3	6.2	6.7
Ta		1.3			1.0	1.7		2.6	0.4	1.8	0.5	0.7	0.7	0.6		1.2		0.4	0.2	1.2	0.3
Co	2.4	5.4	7.8	2.4	1.4	0.2	2.4	42.4	25.7	0.9	0.1	21.1	21.8	2.4	3.5	1.0		26.6	0.4	37.1	0.5
U	3.0	5.3	5.3	3.0	14.8	9.5	3.0	4.9	9.8	15.2	5.5	10.1	9.9	6.0	3.0	6.0		2.8	1.8	2.9	3.1

Appendix 3-1a Major and Trace element analysis of the gneiss, syn and late-orogenic granite.

	Gneiss and Syn-orogenic granite																	Late-orogenic granite			
Sample	230	231	232	233	234	235	236	237	273	272	24	25	25A	27	91	93		224	275	4	5
La	32.5	171.3	171.0	97.3	38.6	31.3	33.9	7.7	8.5	183.8	15.0	41.4	29.3	49.3	23.8	79.1		26.8	46.8	35.0	61.2
Ce	31.9	344.2	510.8	275.7	80.2	66.4	38.6	10.6	15.2	304.4	26.9	87.8	61.0	94.9	35.7	160.7		49.2	76.5	66.2	113.5
Pr		37.2			9.6	9.3		1.4	1.6	29.5	3.0	9.8	6.8	9.8		17.3		5.2	8.1	7.0	11.6
Nd		129.7			34.8	36.0		5.3	6.2	92.3	11.2	34.9	24.5	32.8		61.7		17.5	25.8	24.5	38.7
Sm		19.3			7.1	9.3		1.6	1.3	13.5	2.8	7.4	5.3	5.2		11.3		2.8	3.1	4.0	5.3
Eu		2.5			0.7	0.2		0.2	0.3	1.8	0.3	0.5	0.5	0.9		0.5		0.6	0.7	0.9	1.0
Gd		12.1			5.9	10.2		2.8	1.4	10.0	2.8	6.8	5.2	4.0		10.7		1.9	1.7	2.8	3.2
Tb		1.5			0.9	1.7		0.7	0.2	1.4	0.4	1.0	0.8	0.5		1.6		0.2	0.2	0.4	0.4
Dy		7.0			4.7	11.3		5.9	1.1	8.4	2.3	5.2	4.4	2.5		10.4		1.0	0.8	1.9	1.7
Ho		1.1			0.8	2.2		1.6	0.2	1.6	0.4	0.9	0.8	0.4		2.0		0.1	0.1	0.4	0.3
Er		2.8			2.2	6.8		6.3	0.6	4.6	1.0	2.3	2.1	1.2		6.0		0.3	0.4	1.1	0.7
Tm		0.4			0.3	1.0		1.1	0.1	0.6	0.1	0.3	0.3	0.2		0.8		0.0	0.0	0.2	0.1
Yb		2.2			1.9	6.8		9.0	0.4	4.3	0.9	1.8	1.6	1.1		5.7		0.3	0.4	1.2	0.7
Lu		0.3			0.3	1.0		1.5	0.1	0.6	0.1	0.3	0.3	0.2		0.8		0.1	0.1	0.2	0.1
ASI	1.1	1.0	1.0	1.2	1.2	1.1	1.2	1.2	1.1	1.1	1.0	1.1	1.0	1.0	1.1	0.9		1.1	1.1	1.1	1.0
K2O/Na 2O	1.2	1.4	1.2	1.7	1.8	1.1	1.2	1.0	1.1	2.2	1.3	1.3	1.5	1.9	1.9	1.3		1.7	1.3	1.9	1.4
Eu/Eu*	-	0.5		-	0.3	0.0		0.3	0.7	0.4	0.3	0.2	0.3	0.6		0.1		0.7	0.9	0.8	0.7
(La/Sm) N	146.9	4.9		0.7	3.0	1.9		2.6	3.6	7.4	3.0	3.1	3.0	5.2		3.9		5.3	8.2	4.8	6.4
(La/Yb)N	430542.3	46.7		0.5	12.2	2.8		0.5	11.9	26.1	10.5	14.3	10.9	27.7		8.4		50.7	77.1	17.1	56.3
ΣREE	69.0	731.6		-	188.0	193.6		55.7	37.2	656.7	67.3	200.3	142.6	203.0		368.8		106.0	164.5	145.7	238.4

Appendix 3-1b REEs analysis of the gneiss, syn and late-orogenic granite

Table 1 Oxides %	Basaltic Pillow Lava								Massive Gabbro												
Sample	**202A**	**202B**	**203B**	**204**	**205**	**206A**	**215**		**201**	**206B**	**207**	**209**	**240A**	**240B**	**243**	**244**	**244A**	**244B**	**247**	**MG**	**GA**	**216**
SiO2	47.51	46.06	47.34	47.98	43.88	45.06	57.26		44.30	44.95	44.14	58.10	48.48	47.44	48.85	48.76	47.53	47.19	46.96	53.31	47.18	54.05
TiO2	1.46	1.34	1.40	1.47	1.50	1.56	0.71		1.33	1.44	1.27	2.72	0.77	0.68	0.78	0.87	0.57	0.74	0.98	0.56	0.25	0.64
Al2O3	17.37	17.18	17.74	17.47	16.88	18.95	15.02		18.70	20.19	20.87	14.36	13.87	16.37	17.46	20.37	17.89	18.19	18.86	14.98	13.97	17.44
Fe2O3	10.14	8.83	10.68	11.13	14.11	12.95	8.31		12.34	13.00	11.31	8.95	10.22	8.59	7.63	6.08	8.13	8.17	8.36	8.37	5.45	7.96
MnO	0.16	0.15	0.16	0.16	0.24	0.23	0.15		0.21	0.21	0.18	0.11	0.24	0.13	0.13	0.11	0.18	0.18	0.13	0.19	0.21	0.18
MgO	5.10	4.33	6.39	5.07	7.45	5.81	5.33		6.91	4.82	5.95	2.12	10.50	9.94	8.80	7.01	8.86	8.84	9.83	9.35	9.52	5.43
CaO	14.68	19.21	12.30	12.89	12.85	12.54	8.49		14.13	12.42	14.49	5.23	14.27	14.51	13.26	13.77	15.33	14.97	11.66	8.73	17.41	9.07
NaO2	2.37	1.45	2.68	2.50	0.67	1.55	3.20		0.66	1.84	0.83	3.22	0.28	0.70	1.35	1.69	0.13	0.14	1.78	3.03	1.75	3.60
K2O	0.31	0.14	0.50	0.45	1.06	0.43	0.31		0.43	0.37	0.31	3.46	0.29	0.15	0.41	0.29	0.11	0.16	0.33	0.21	0.15	0.32
P2O5	0.25	0.24	0.21	0.24	0.05	0.15	0.12		0.02	0.19	0.02	1.11	0.12	0.06	0.07	0.09	0.23	0.11	0.12	0.11	0.00	0.07
LOI	0.66	1.07	0.58	0.63	1.32	0.76	1.10		0.98	0.57	0.63	0.62	0.96	1.43	1.27	0.96	1.05	1.31	0.99	1.17	4.10	1.26
Total	**100.00**	**100.00**	**100.00**	**100.00**	**100.00**	**100.00**	**100.00**		**100.00**	**100.00**	**100.00**	**100.00**	**100.00**	**100.00**	**100.00**	**100.00**	**100.00**	**100.00**	**100.00**	**100.00**	**100.00**	**100.00**
Sc	35.1	31.0	31.1	32.6	45.1	32.8	18.8		45.1	18.8	31.2	8.7	55.2	23.7	36.3	34.4	35.0	31.7	51.1	15.6	61.3	33.9
V	225	207	217	226	409	360	152		409	198	321	82	288	163	202	232	214	194	270	112	200	193
Cr	243	200	156	221	94.2	30.4	267		94	12	45	21	241	387	923	275	266	935	280	907	774	187
Co	36.6	35.4	30.4	34.8	43.6	34.4	22.1		43.6	38.0	30.6	12.5	48.8	38.4	34.2	21.8	23.2	25.1	40.9	31.8	30.8	20.2
Ni	98.6	133	67.8	83.5	10.9	0	89.8		10.9	0.0	2.6	5.3	70.2	25.7	9.4	38.0	40.5	10.5	44.1	186.2	46.4	23.3
Cu	65.8	109	22.2	28.5	20.2	23.6	26.1		20.2	58.6	71.4	23.7	5.8	21.3	7.3	6.7	12.5	8.9	25.7	80.0	7.2	17.4
Zn	108	73.7	126	156	110	106	63.5		110	103	90	249	192	63	63	73	78	60	66	83	62	68.5
Rb	1.76	2.68	3.02	2.99	34.4	8.81	4.99		34.4	6.4	5.2	126.5	2.0	10.5	15.9	5.0	5.2	14.9	6.6	7.8	4.1	3.95
Sr	624	711	748	901	422	601	371		422	612	599	613	286	316	289	232	241	355	418	325	235	320
Y	27.1	25.2	24.5	27.2	12.2	13.2	29.7		12.2	9.5	8.3	32.9	13.2	15.5	16.7	18.9	21.4	18.8	16.3	20.6	13.6	16.8
Zr	21.7	33.7	19.3	19.5	11.8	11.1	62.9		11.8	7.1	10.6	231	13.4	14.2	51.6	40.3	37.8	58.9	32.9	97.8	22.7	30.7
Nb	2.82	2.56	2.47	2.73	0.71	1.22	3.66		0.7	0.9	0.8	27.5	2.9	1.0	3.1	4.2	3.5	3.1	2.7	4.3	2.0	1.23
Ba	95.1	56.4	227	147	150	117	59.9		149.6	98.2	84.6	1503	78.4	46.3	69.9	33.8	35.2	62.9	45.3	58.0	63.0	131
Hf	1.08	1.28	1.16	1.07	0.59	0.58	1.77		0.6	0.4	0.5	5.4	0.6	0.6	NA	NA	NA	NA	NA	NA	NA	1.19
Ta	0.09	0.08	0.15	0.12	0.01	0	0.22		0.0	0.1	0.0	1.1	0.1	0.0	NA	NA	NA	NA	NA	NA	NA	0.06
Pb	16.6	6.33	5.76	3.11	5.37	4.09	5.10		5.4	3.3	3.4	28.1	2.8	3.2	3.0	3.0	7.1	3.0	3.0	7.7	6.4	5.94
Th	0.41	0.35	0.46	0.44	0.26	0.34	4.21		0.3	0.2	0.3	26.2	1.2	0.4	3.0	4.3	4.7	3.0	3.0	3.0	3.0	1.63
U	0.20	0.19	0.31	0.20	0.22	0.29	1.15		0.2	0.2	0.2	5.8	0.9	0.2	3.0	3.0	3.0	3.0	3.3	3.0	3.0	0.70

Appendix 3-2a Major and trace elements of the Arid Unit

Table 1 Oxides %	Basaltic Pillow Lava								Massive Gabbro												
Sample	**202A**	**202B**	**203B**	**204**	**205**	**206A**	**215**		**201**	**206B**	**207**	**209**	**240A**	**240B**	**243**	**244**	**244A**	**244B**	**247**	**MG**	**GA**	**216**
La	9.34	7.86	8.10	9.29	2.90	4.72	10.9		2.9	4.1	2.7	167.7	8.3	4.0	17.5	17.1	20.5	15.9	18.1	16.2	18.9	7.21
Ce	25.0	20.9	22.1	25.0	7.39	11.9	24.5		7.4	9.9	6.8	350.9	18.9	10.7	4.9	4.9	4.9	4.9	4.9	4.9	4.9	20.1
Pr	3.62	3.10	3.35	3.68	1.18	1.85	3.36		1.2	1.4	1.0	39.2	2.6	1.6	-	-	-	-	-	-	-	2.20
Nd	17.3	15.1	16.1	17.9	6.44	9.71	15.3		6.4	7.2	5.2	151.4	11.9	8.3	-	-	-	-	-	-	-	9.35
Sm	4.48	4.05	4.31	4.69	2.10	2.77	4.34		2.1	1.9	1.5	23.1	2.9	2.4	-	-	-	-	-	-	-	2.58
Eu	1.69	1.60	1.54	1.57	0.91	1.24	0.98		0.9	1.0	0.7	4.1	0.9	1.0	-	-	-	-	-	-	-	0.83
Tb	0.84	0.78	0.79	0.82	0.39	0.45	0.77		0.4	0.3	0.3	1.8	0.5	0.5	-	-	-	-	-	-	-	0.47
Gd	5.39	4.99	4.90	5.36	2.46	3.13	4.74		2.5	2.1	1.7	15.5	3.1	3.0	-	-	-	-	-	-	-	2.88
Dy	5.16	4.78	4.64	5.06	2.41	2.67	5.13		2.4	1.9	1.7	8.0	2.7	3.0	-	-	-	-	-	-	-	3.06
Ho	1.01	0.95	0.97	1.01	0.47	0.53	1.06		0.5	0.4	0.3	1.3	0.5	0.6	-	-	-	-	-	-	-	0.64
Er	2.92	2.70	2.70	2.90	1.32	1.43	3.22		1.3	1.1	0.9	3.1	1.4	1.7	-	-	-	-	-	-	-	1.89
Tm	0.40	0.37	0.40	0.41	0.18	0.19	0.47		0.2	0.1	0.1	0.4	0.2	0.2	-	-	-	-	-	-	-	0.29
Yb	2.54	2.37	2.37	2.58	1.11	1.17	3.12		1.1	0.9	0.8	2.1	1.3	1.5	-	-	-	-	-	-	-	1.82
Lu	0.37	0.34	0.38	0.38	0.16	0.17	0.46		4.1	4.8	3.3	6.1	2.9	4.2	-	-	-	-	-	-	-	-
La/Nb	3.32	3.08	3.28	3.40	4.07	3.86	2.98		1.4	3.0	2.0	12.5	6.9	3.3	-	-	-	-	-	-	-	5.86
Ce/Pb	1.51	3.30	3.83	8.05	1.37	2.91	4.80		3.3	4.3	3.3	4.8	3.1	6.0	-	-	-	-	-	-	-	3.38
Nb/U	13.81	13.45	8.04	13.58	3.28	4.18	3.18		1.4	2.1	1.8	7.3	2.8	1.7	-	-	-	-	-	-	-	1.76
La/Sm	2.09	1.94	1.88	1.98	1.38	1.71	2.51		0.3	0.3	0.3	0.2	0.2	0.3	-	-	-	-	-	-	-	2.80
Sm/Nd	0.26	0.27	0.27	0.26	0.33	0.28	0.28		4.1	4.8	3.3	6.1	2.9	4.2	-	-	-	-	-	-	-	0.28
A.I.	24.1	17.8	31.5	26.4	38.6	30.7	32.6		33.2	26.7	29.0	39.8	42.6	39.9	38.7	32.1	36.7	37.3	43.1	44.9	33.5	31.2

Appendix 3-2b REEs of the Arid Unit

Table 2	Metavolcanics												
SAMBLE	**SK50**	**SK51**	**SK52**	**SK54**	**SK55**	**SK28**	**SK 218**	**SK 219**	**SK 254**	**SK 256Br**	**SK 257**	**SK 258**	**SK 257A**
SiO_2	60.70	42.91	51.66	46.94	52.68	46.49	57.73	53.02	54.45	63.11	59.73	50.43	61.64
TiO_2	1.49	0.87	2.16	1.40	1.36	1.66	1.65	1.87	2.37	1.90	1.53	1.26	1.56
Al_2O_3	14.01	12.42	15.75	16.83	12.10	16.30	12.27	14.66	15.77	17.21	13.75	15.80	14.41
Fe_2O_3	5.51	15.30	15.11	9.08	11.97	11.17	15.76	14.52	10.95	8.16	13.08	11.08	10.08
MnO	0.07	0.22	0.09	0.18	0.28	0.16	0.07	0.09	0.09	0.09	0.15	0.18	0.12
MgO	2.57	8.45	3.41	5.61	7.85	8.15	3.38	4.31	3.33	0.78	3.27	4.28	2.13
CaO	5.28	17.41	2.79	8.28	9.71	11.81	1.48	2.07	3.75	0.24	0.75	5.16	1.23
Na_2O	6.68	0.00	5.92	2.72	1.88	1.75	4.58	5.41	7.14	0.06	4.29	4.43	5.81
K_2O	2.79	0.23	0.16	0.83	0.42	0.71	0.11	0.11	0.28	5.02	0.05	0.77	0.06
P_2O_5	0.25	0.20	0.54	0.30	0.39	0.12	0.29	0.32	0.53	0.47	0.61	0.24	0.63
LOI	0.65	1.97	2.40	7.84	1.34	1.68	2.69	3.63	1.34	2.96	2.79	6.37	2.32
Total	100.00	100.00	100.00	100.00	100.00	100.00	100.00	100.00	100.00	100.00	100.00	100.00	100.00
Sc	18.5	25.3	20.1	22.6	33.7	24.7	25.3	28.1	28.5	25.8	16.3	27.8	26.03
V	71	115	219	194	223	210	293	285	250	154	69	202	73
Cr	5	462	36	85	165	293	42	34	34	56	10	98	7
Co	9	4	22	19	37	39	13	12	12	11	32	18	27
Ni	0	16	9	34	58	10	9	13	5	19	24	13	3
Cu	31	21	12	8	19	12	27	9	13	22	126	7	50
Zn	28	62	54	100	120	95	45	55	47	28	67	94	61
Rb	14	3	1	10	9	16	1	1	2	84	1	14	3
Sr	64	394	63	496	682	324	54	63	74	41	59	157	71
Y	42	24	65	26	32	36	23	26	76	30	32	16	80
Zr	291	92	343	34	32	131	203	236	483	335	407	173	446
Nb	8	3	8	6	7	5	6	6	10	6	8	3	11
Ba	385	91	35	252	142	123	31	41	63	699	72	217	69
Hf	8	2	9	-	-	-	5	6	10	8	10	4	-
Ta	1	0	0	-	-	-	0	0	1	0	0	0	-
Pb	2	3	2	10	13	3	2	2	5	2	2	2	3
Th	6	4	8	3	4	3	4	4	9	7	7	4	4
U	4	3	4	3	5	3	2	2	4	3	3	2	3

Appendix 3-3a Major and trace elements of the Abutulu Unit

Table 2 Continued													
La	31.0	21.9	17.1	-	-	-	12.7	8.9	23.1	41.6	39.2	16.2	31.8
Ce	54.0	56.4	44.3	-	-	-	34.9	30.6	57.1	81.8	86.1	38.5	123.5
Pr	7.0	8.0	6.5	-	-	-	5.3	5.3	8.2	12.5	12.1	5.0	-
Nd	29.0	34.4	30.3	-	-	-	24.7	26.4	39.0	53.9	53.2	22.4	-
Sm	6.9	7.2	9.3	-	-	-	6.1	7.2	11.1	11.1	11.4	5.5	-
Eu	1.7	1.5	2.2	-	-	-	1.3	1.4	2.4	2.2	2.1	1.5	-
Tb	1.1	0.8	1.7	-	-	-	0.7	0.9	2.1	1.1	1.2	0.7	-
Gd	7.0	6.1	11.0	-	-	-	5.4	6.4	13.4	8.9	9.7	5.2	-
Dy	7.0	4.6	11.3	-	-	-	4.4	5.0	13.1	5.7	5.8	3.2	-
Ho	1.4	0.9	2.3	-	-	-	0.9	1.1	2.6	1.1	1.2	0.6	-
Er	4.4	2.4	6.6	-	-	-	2.7	3.0	7.7	3.6	3.8	1.9	-
Tm	0.6	0.3	0.9	-	-	-	0.4	0.5	1.1	0.6	0.6	0.3	-
Yb	4.5	2.1	6.1	-	-	-	2.9	3.3	7.0	4.1	4.6	2.3	-
Lu	0.7	0.3	0.9	-	-	-	0.5	0.6	1.0	0.7	0.8	0.4	-
La/Nb	3.72	8.09	2.07	-	-	-	2.31	1.47	2.30	6.93	5.04	4.89	-
Ce/Pb	35.28	17.97	20.92	-	-	-	20.99	16.16	12.65	45.74	35.26	16.99	-
Nb/U	2.30	0.91	2.12	-	-	-	3.20	2.71	2.67	2.08	2.62	2.11	-
La/Sm	4.50	3.03	1.84	-	-	-	2.07	1.24	2.09	3.75	3.45	2.96	-
Sm/Nd	0.24	0.21	0.31	-	-	-	0.25	0.27	0.28	0.21	0.21	0.24	-
A.I.	30.9	33.3	29.1	36.9	41.7	39.5	36.6	37.2	24.9	95.1	39.7	34.5	23.8

Appendix 3-3b REEs of the Abutulu Unit

	Rb	Sr	87Rb/86Sr	87Sr/86Sr	2σ	Sri at 778Ma	Sm	Nd	147Sm/144Nd	143Nd/144Nd	2σ	Ndi at 778Ma	Nd at 778±90Ma	T_{DM} Ma
sk-202a	1.76	624	0.0081	0.703628	0.000013	0.703537	4.48	17.3	0.1566	0.512757	0.000009	0.511919	+6.4±0.5	778
sk202b	2.68	711	0.0109	0.703693	0.000016	0.703572	4.05	15.1	0.1625	0.512779	0.000009	0.511908	+6.2±0.4	802
sk-203b	3.02	748	0.0117	0.704188	0.000012	0.704058	4.31	16.1	0.1618	0.512767	0.000009	0.511900	+6.1±0.4	825
sk-204	2.99	901	0.0096	0.704036	0.000015	0.703930	4.69	17.9	0.1586	0.512757	0.000009	0.511907	+6.2±0.5	807
sk-240	10.5	316	0.0959	0.703415	0.000015	0.702349	2.38	8.26	0.1744	0.512813	0.000007	0.511879	+5.7±0.3	905
sk-240a	1.98	286	0.0201	0.703020	0.000012	0.702797	2.93	11.9	0.1487	0.512663	0.000008	0.511867	+5.3±0.6	899
sk-254	2.28	74.0	0.0892	0.704266	0.000010	0.703275	11.1	39.0	0.1303	0.512798	0.000007	0.511876	+5.7±0.3	859
sk255	36.5	51.0	2.0751	0.721407	0.000012	0.698354	4.23	19.6	0.1242	0.512577	0.000006	0.511880	+5.5±0.8	792
sk256	84.2	41.4	5.9156	0.753392	0.000011	0.687676	11.1	53.9	0.1291	0.512584	0.000008	0.511918	+6.2±0.8	789
sk257	0.56	59.2	0.0274	0.704842	0.000010	0.704537	11.4	53.2	0.1478	0.512611	0.000007	0.511919	+6.3±0.8	854
sk258	14.1	157	0.2605	0.706625	0.000010	0.703732	5.47	22.4	0.1566	0.512678	0.000007	0.511886	+5.7±0.6	778
sk-014	4.15	197	0.0609	0.704823	0.000015	0.704146	4.47	17.2	0.1567	0.512776	0.000006	0.511937	+6.8±0.5	732

	Rb	Sr	87Rb/86Sr	87Sr/86Sr	2σ	Sri at 976Ma	Sm	Nd	147Sm/144Nd	143Nd/144Nd	2σ	Ndi at 976Ma	Nd at 976Ma	T_{DM} Ma
SK 25	1.76	624	7.149683	0.783052	0.000010	0.683274	7.394	34.9	0.1275	0.512527	0.000009	0.511911	+6.4±0.5	925
SK 25A	2.68	711	7.072846	0.783399	0.000012	0.684693	5.279	24.54	0.1295	0.512531	0.000009	0.511906	+6.2±0.5	939
SK 27	3.02	748	1.901475	0.719691	0.000015	0.693155	5.211	32.78	0.0957	0.512317	0.000009	0.511911	+6.3±0.8	946
SK93	2.99	901	8.786430	0.787351	0.000010	0.664730	11.26	61.69	0.1099	0.512394	0.000009	0.511773	+6.1±0.6	957
SK231	10.5	316	0.772212	0.711028	0.000015	0.700251	19.28	129.7	0.0895	0.512273	0.000007	0.511767	+6.3±0.8	949
SK234	1.98	286	7.442692	0.760097	0.000024	0.656229	7.13	34.78	0.1234	0.512468	0.000008	0.511770	+5.9±0.5	975
	Rb	Sr	87Rb/86Sr	87Sr/86Sr	2σ	Sri at 600Ma	Sm	Nd	147Sm/144Nd	143Nd/144Nd	2σ	Ndi at 600Ma	Nd at 600Ma	T_{DM} Ma
SK4	2.28	74.0	2.816971	0.727191	0.000018	0.703088	4.015	24.53	0.09852	0.512439	0.000007	0.512025	+3.7±0.1	807
SK5	36.5	51.0	0.966498	0.711586	0.000011	0.703316	5.285	38.7	0.08220	0.512380	0.000006	0.512029	+3.8±0.1	776
SK224	84.2	41.4	1.530476	0.715616	0.000011	0.702520	2.787	17.46	0.09608	0.512427	0.000008	0.512038	+3.6±0.1	806
SK275	0.56	59.2	0.559396	0.707869	0.000012	0.703082	3.122	25.77	0.07292	0.512329	0.000007	0.512026	+3.5±0.1	780

Appendix 5-1 Isotopic data for the low and medium-grade rocks and granitoids of the western Nuba Mountains

Grain.Spot	% $^{206}Pb_c$	ppm U	ppm Th	$^{232}Th/^{238}U$	±%	(1) ppm $^{206}Pb^*$	(1) $^{206}Pb/^{238}U$ Age		(1) $^{207}Pb/^{206}Pb$ Age		% Dis-cor-dant	(1) $^{207}Pb^*/^{206}Pb^*$	±%	(1) $^{207}Pb^*/^{235}U$	±%	(1) $^{206}Pb^*/^{238}U$	±%	err corr	Th/U	Domain
1.1	0.30	2252	41	0.019	2.38	190	603	±7	593	±17	-2	0.0602	0.7	0.816	1.4	0.0982	1.2	0.9	0.02	rim
2.1	0.08	350	202	0.597	0.23	30	614	±10	597	±22	-3	0.0612	1.5	0.844	1.9	0.1001	1.8	0.7	0.58	core
3.1	3.66	146	59	0.420	0.37	12	574	±9	564	±140	-2	0.0574	2.2	0.736	2.4	0.0930	1.8	0.5	0.41	core
3.2	0.84	3110	511	0.170	0.37	256	589	±6	574	±21	-3	0.0591	1.0	0.780	1.3	0.0957	1.1	0.7	0.16	rim
4.1	0.20	1654	80	0.050	0.65	142	614	±8	600	±13	-2	0.0606	0.4	0.836	1.4	0.1001	1.4	0.9	0.05	rim
5.1	1.91	1679	359	0.221	0.84	142	605	±10	606	±52	+0	0.0570	1.9	0.769	2.1	0.0980	1.9	0.6	0.21	rim
6.1	0.11	577	190	0.341	0.23	49	611	±8	593	±18	-3	0.0626	0.9	0.861	1.5	0.0997	1.5	0.8	0.33	rim

Errors are 1-sigma; Pb_c and Pb^* indicate the common and radiogenic portions, respectively.

Error in Standard calibration was 0.28% (not included in above errors but required when comparing data from different mounts).

(1) Common Pb corrected using measured ^{204}Pb.

(2) Common Pb corrected by assuming $^{206}Pb/^{238}U$-$^{207}Pb/^{235}U$ age-concordance

Appendix 5-2a U-Pb isotopic composition of sample ZR1

Grain.Spot	% 206Pbc	ppm U	ppm Th	232Th /238U	±%	(1) ppm 206Pb*	(1) 206Pb /238U Age		(1) 207Pb /206Pb Age		% Dis-cor-dant	(1) 207Pb* /206Pb*	±%	(1) 207Pb* /235U	±%	(1) 206Pb* /238U	±%	err corr	Th/U	Domain
1.1	0.52	185	61	0.338	0.34	19	728	±8	708	±49	-3	0.0630	2.3	1.038	2.6	0.1195	1.1	0.4	0.33	core
2.2	0.02	568	153	0.278	0.22	50	624	±7	626	±14	+0	0.0606	0.6	0.849	1.3	0.1016	1.1	0.9	0.27	core
2.3	0.45	536	45	0.086	0.37	44	592	±6	616	±27	+4	0.0603	1.3	0.801	1.6	0.0963	1.1	0.6	0.08	rim
3.1	1.22	2104	302	0.148	0.31	169	576	±7	648	±29	+12	0.0612	1.3	0.789	1.8	0.0935	1.2	0.7	0.14	rim
4.1	0.08	179	31	0.178	1.67	17	692	±14	684	±25	-1	0.0623	1.2	0.973	2.5	0.1134	2.2	0.9	0.17	core
5.1	0.28	1225	93	0.079	0.25	100	583	±6	619	±14	+6	0.0604	0.7	0.789	1.2	0.0947	1.0	0.8	0.08	rim
5.2	0.00	280	85	0.312	0.28	29	743	±8	721	±16	-3	0.0634	0.8	1.068	1.3	0.1221	1.1	0.8	0.30	core
6.1	0.03	1161	103	0.091	0.24	95	586	±6	604	±9	+3	0.0600	0.4	0.787	1.1	0.0951	1.0	0.9	0.09	rim
7.1	0.58	6464	1502	0.240	0.09	438	490	±5	516	±8	+5	0.0576	0.4	0.627	1.1	0.0789	1.0	0.9	0.23	rim
8.1	0.05	1230	47	0.039	0.35	104	604	±6	597	±10	-1	0.0598	0.5	0.810	1.2	0.0982	1.1	0.9	0.04	rim
8.2	0.04	457	195	0.442	0.63	46	716	±8	733	±14	+2	0.0637	0.7	1.033	1.3	0.1175	1.2	0.9	0.43	core
9.1	1.70	1123	66	0.061	0.30	91	583	±6	590	±47	+1	0.0596	2.1	0.778	2.4	0.0946	1.0	0.4	0.06	rim
10.1	0.14	1507	161	0.110	0.83	129	613	±6	607	±15	-1	0.0601	0.7	0.827	1.2	0.0998	1.0	0.8	0.11	rim
11.1	--	121	23	0.194	0.51	13	737	±10	745	±24	+1	0.0641	1.1	1.070	1.8	0.1211	1.4	0.8	0.19	core
12.1	0.53	865	66	0.079	0.63	72	594	±6	613	±20	+3	0.0603	0.9	0.803	1.4	0.0966	1.0	0.7	0.08	rim
13.1	2.47	87	29	0.347	0.45	8	631	±9	863	±107	+28	0.0678	5.1	0.961	5.4	0.1028	1.6	0.3	0.34	core

Errors are 1-sigma; Pb_c and Pb^* indicate the common and radiogenic portions, respectively.
Error in Standard calibration was 0.36% (not included in above errors but required when comparing data from different mounts).
(1) Common Pb corrected using measured ^{204}Pb.
(2) Common Pb corrected by assuming $^{206}Pb/^{238}U$-$^{207}Pb/^{235}U$ age-concordance

Appendix 5-2b U-Pb isotopic composition of sample ZR2